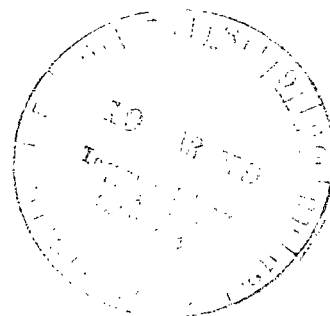NASA Technical Paper 1222

Configuration Management and Automatic Control of an Augmentor Wing Aircraft With Vectored Thrust

Luigi S. Cicolani, B. Sridhar,
and George Meyer

MARCH 1979

NASA

NASA Technical Paper 1222

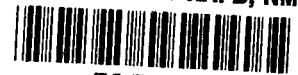# Configuration Management and Automatic Control of an Augmentor Wing Aircraft With Vectored Thrust

Luigi S. Cicolani, B. Sridhar,
and George Meyer
Ames Research Center
Moffett Field, California

TABLE OF CONTENTS

<div align="center">SYMBOLS</div>

A_u applied specific force component along the air velocity vector

A_N applied specific force component normal to the air velocity vector

$\mathscr{A}_{\delta_f}(\bar{x},\bar{p})$ all applied specific forces that can be generated by the regulator at fixed flap, given $(\bar{x},\bar{p})$

$\mathscr{A}_{\delta_f,\nu}(\bar{x},\bar{p})$ all applied specific forces that can be generated by the regulator, at fixed flap and nozzle, given $(\bar{x},\bar{p})$

$\bar{a}$ acceleration vector

$\overline{ac}$ commanded acceleration vector

$\bar{a}_{app}$ applied specific force from engine and aerodynamic forces

C_J cold thrust coefficient

C_L, C_D aircraft lift and drag coefficients

$CM_{\delta_f}(\bar{x},\bar{p})$ regulator control margin with fixed flap

$CM_{\delta_f,\alpha}(\bar{x},\bar{p})$ regulator control margin with fixed flap and angle of attack

$CM_{\delta_f,\delta t}(\bar{x},\bar{p})$ regulator control margin with fixed flap and throttle

$CM_{\delta_f,\nu}(\bar{x},\bar{p})$ regulator control margin with fixed flap and nozzle

$\mathscr{E}$ elliptical region

$\bar{F}_A, \bar{F}_E$ aerodynamic and engine forces

$F^*(A_u,V_e)$ flap schedule

$\mathscr{F}_T$ all flight conditions, $(\bar{x},\bar{p})$, for which trim solutions exist

$\mathscr{F}_{TA}$ all flight conditions, $(\bar{x},\bar{p})$, for which operationally acceptable trim solutions exist

g gravitational acceleration

h altitude

K_R position error feedback gain

LM lift margin

$\dot{m}_E$	engine mass flow rate
N_H	engine power, percent reference rpm
$\mathscr{P}_o$	design regime for p
$\bar{p}$	vector of parameters in the trim equations (W, τ, δ)
$\bar{p}_s$	standard case parameter values
Q	dynamic pressure
R_c	radius of curvature
$\bar{R}$	aircraft position vector from runway axes origin
$\overline{RC}$	commanded aircraft position vector
S_w	wing area
S_ν, S_T	control sensitivity matrices for fixed nozzle and fixed throttle regulators
T_C	equivalent thrust of cold pressurized engine air exhausted through augmentor flap
T_H	engine exhaust thrust
t	time, sec
$\mathscr{U}_o$	all values of $\bar{u}$ for which aircraft force model is defined
$\mathscr{U}_T(\bar{x},\bar{p})$	all solutions, $\bar{u}$, of trim equations for the flight condition $(\bar{x},\bar{p})$
$\mathscr{U}_{TA}(\bar{x},\bar{p})$	all operationally acceptable trim solutions, $\bar{u}$, for the flight condition $(\bar{x},\bar{p})$
$\bar{u}$	vector of control variables in the trim equations (δ_f, ν, α, δ_t)
V	speed with respect to runway axes
V_A	airspeed
V_E	equivalent airspeed, $V_A\sqrt{\dfrac{\rho}{\rho_o}}$
$\bar{V}$	aircraft velocity vector with respect to runway axes
$\overline{VA}$	aircraft velocity vector with respect to air mass
$\overline{VC}$	commanded aircraft velocity vector

W	aircraft weight
$\bar{W}$	steady wind (mean air mass velocity with respect to runway axes)
$\mathscr{X}_o$	design regime of $\bar{x}$
$\mathscr{X}(\bar{p})$	all values of $\bar{x}$ for which a trim solution exists, given $\bar{p}$
$\mathscr{X}_A(\bar{p})$	all values of $\bar{x}$ for which an operationally acceptable trim solution exists, given $\bar{p}$
$\mathscr{X}_B(\bar{p})$	flight envelope abuse buffer regime, $\mathscr{X} - \mathscr{X}_A$
$\bar{x}$	vector list of path variables (V_E, A_u, A_N) used in the trim equations
α	angle of attack
β	sideslip angle
γ	flight-path angle of $\bar{V}$ with respect to horizontal plane
γ_A	flight-path angle of $\overline{VA}$ with respect to horizontal plane
δ	atmospheric pressure ratio
δ_e	elevator angle
δ_{e_T}	trim value of δ_e
δ_f	flap angle
δ_R	rudder angle
δ_t	engine throttle lever angle
δ_w	aileron wheel control angle
Θ	body axes Euler pitch angle
ν	engine exhaust nozzle angle
$\nu^*(\bar{x})$	nozzle schedule
ρ	atmospheric density
τ	atmospheric temperature ratio
Φ	body axis Euler roll angle
ϕ	the null set

ϕ_V direction of applied normal acceleration, A_N, from vertical plane containing $\overline{VA}$

ψ body axis Euler heading angle

ψ_V heading angle of $\overline{V}$

ψ_{VA} heading angle of $\overline{VA}$

$\overline{\omega}$ angular velocity of aircraft body axes

Subscripts and Superscripts:

$(\ )_c$ commanded value of ( )

$(\ )_{NOM}$ value of ( ) on the nominal approach path

$\overline{(\ )}$ vector

$\hat{(\ )}$ estimated or approximated value of ( )

$\overline{\nabla}_x f(x)$ Jacobian of $f(x)$ wrt x

Axes, Vectors and Transformation Notation:

$\overline{i}, \overline{j}, \overline{k}$ orthogonal unit vectors defining right-handed axes frame

$\underline{u}, \overline{m}, \overline{n}$ path axes reference frame

$(\ )_f$ vector given by its components in frame f; f may be s (stability axes), b (body axes), p (path axes), or r (runway axes)

$T_{f_2 f_1}$ transformation of vectors referred to axis frame f_1 into vectors referred to axis frame f_2

$(\ )^T$ vector or matrix transpose

CONFIGURATION MANAGEMENT AND AUTOMATIC CONTROL OF AN AUGMENTOR

WING AIRCRAFT WITH VECTORED THRUST

Luigi S. Cicolani, B. Sridhar,* and George Meyer

Ames Research Center

SUMMARY

An advanced structure for automatic flight-control logic for powered-lift aircraft operating in terminal areas is under investigation at Ames Research Center. This structure is based on acceleration control; acceleration commands are constructed as the sum of acceleration on the reference trajectory and a corrective feedback acceleration to regulate path tracking errors. The central element of the structure, termed a Trimmap, uses a model of the aircraft aerodynamic and engine forces to calculate the control settings required to generate the acceleration commands. The feedback control design for nonlinear plants is simplified by this structure, since the transfer function of the controlled element (the Trimmap-aircraft combination) is approximately unity at all configurations and flight conditions. Further, consideration of plant nonlinearity is isolated in the Trimmap and the nonlinearity is algebraic rather than dynamic.

This report describes the design criteria for the Trimmap and derives a Trimmap for Ames' experimental augmentor wing jet STOL research aircraft. The principal problems are associated with control redundancy (there are two more controls than necessary to generate any given acceleration command) and model nonlinearity. Control redundancy is resolved using a stored configuration schedule which selects two of the controls (flap and engine exhaust nozzle) as a function of the reference flight condition, while the remaining two controls (elevator and throttle) are computed on the basis of the total acceleration command and the aircraft force model. The configuration schedule is designed off-line to optimize configuration-dependent parameters of interest subject to operational constraints on controls usage; the present concept maximizes lift margin and regulator control margin. The algebraic nonlinearity of the force model is treated using piecewise linear descriptions of the model over its finite domain; thus, model accuracy is controlled by the number of pieces and the model is inverted by solving linear equations for each of a finite number of pieces.

The automatic control system, including the Trimmap described in this paper, was subjected to simulation tests using a rigorous STOL approach trajectory. These tests demonstrate the system response to low-frequency inputs, including maneuver commands, Trimmap model errors, and steady winds. The proposed Trimmap maintains an optimal configuration and coordinates all

---

controls during any maneuvers within the terminal area operational domain and in response to steady winds; and it compensates automatically for model errors.

INTRODUCTION

An effort is under way at Ames Research Center to derive methodology for automatic flight-control logic for powered-lift V/STOL aircraft flying in the terminal approach area and to apply the methodology to specific aircraft to demonstrate its feasibility.

Among the powered-lift concepts currently being developed are the augmentor wing, tilt rotor, lift fan, and externally blown flap. When compared to conventional aircraft, these aircraft pose several special flight-control logic problems. First, the use of powered lift at landing entails large changes in the configuration of the aircraft from its conventional cruise configuration to the powered-lift landing configuration. As a result, aerodynamic forces are configuration- and power-dependent and are sufficiently nonlinear that the conventional method of approximating a nonlinear plant by a series of linear perturbation models at different nominal flight conditions and configurations may require prohibitively large numbers of such models in order to provide stable, near-optimum transient response over the full flight envelope. Even at a single flight condition, the variation of forces with controls may be sufficiently nonlinear that nonlinear transient response is obtained from linear control laws. In addition, V/STOL aircraft achieve powered lift by a wide variety of design concepts with radically different control characteristics and aerodynamic force models; consequently, the methodology should accommodate these variations systematically.

A second complicating feature is control redundancy; that is, some STOL aircraft have a novel configuration control such as the engine exhaust nozzles of Ames' augmentor wing jet STOL research aircraft (AWJSRA) or the mast angle of the tilt rotor. Consequently, there are many control settings which trim the aircraft at a given flight condition and, in fact, for the AWJSRA the set of such trim settings has two degrees of freedom. The automatic control system must resolve this redundancy and do so automatically and optimally for all paths within the approach flight regime.

Third, the response of aircraft controls will vary considerably with configuration so that the use of these controls to regulate path errors must also vary with configuration during an approach. For redundantly controlled aircraft the novel control may also be suitable for regulator usage and thereby provide additional control margin.

Finally, it is anticipated that STOL aircraft will operate in terminal areas in conjunction with advanced air traffic control (ATC) and guidance systems which make full use of STOL capability for steep descents and low-speed maneuverability and will command four-dimensional (time of arrival and path) approaches in limited airspace. The output set of these systems is assumed to consist of any trajectory within the flight envelope limits of the

aircraft, and within passenger comfort and operational constraints. The automatic flight-control system should be able to couple the powered-lift STOL aircraft to such a system and the design methodology must accommodate its full output set. In view of the complexities involved in flying these aircraft, either manually or automatically, it can be assumed that an airborne digital computer and associated control actuators will be a key element in V/STOL flight control and the methodology can assume such a digital system.

Automatic Control System Design Structure

A logical structure to accommodate these problems is proposed in reference 1. A block diagram outlining the main elements in that structure for its application to the AWJSRA is shown in figure 1. The system is to be capable of executing four-dimensional trajectories as required by an advanced ATC system controlling terminal area STOL operations, and these may be any trajectories within a domain bounded by aircraft performance limits, passenger comfort constraints, and other operational considerations. These are assumed to be coarsely defined commands; for example, sequences of straight line and circular-arc legs. The command generator element of the logic is an interface whose function is to modify the ATC command as necessary to satisfy operating constraints on maneuvering and on the limits of aircraft maneuver capabilities, and which minimizes the maneuvering activity required to follow the ATC command. Theoretical development of the command generator and simulation test results are presented in reference 2.

The output of the command generator is a time-varying nominal trajectory:

$$\left\{ (RC_r(t),\ VC_r(t), ac_r(t)),\quad t \in [t_o, t_F] \right\}$$

which is assumed given in inertial or runway coordinates.[1] The remaining elements of the control logic — the path regulator, Force Trimmap, and attitude control — track these commands. A special feature of the control structure shown in figure 1 is that the path is tracked on the basis of acceleration commands. The nominal path acceleration, ac_r, and a corrective feedback acceleration, Δa_r, calculated from path errors, are summed to form the total acceleration command, act_r. The regulator control law, $\Delta a_r(RC_r - \hat{R}_r,\ VC_r - \hat{V}_r)$, operates on errors from the reference path; it is linear for small errors with limiting in accordance with the desired acceleration authority for the regulator and acceleration rate capabilities of the aircraft. This control law specifies the desired transient dynamics of the aircraft and control-system combination and these dynamics are achieved in accordance with the accuracy with which the remaining control system tracks the acceleration commands.

---

[1]The reference frame in which a vector is expressed is indicated by subscripts; the subscripts r, b, s, and p refer, respectively, to runway, body, stability, and path axes. When a reference frame is specified, the superscript bar is dropped from the vector notation.

3

The control settings necessary to generate the commanded acceleration, ac_r, are calculated in the Force Trimmap element of figure 1 as solutions of the aircraft force-balance or "trim" equations and additional kinematic relations. The Trimmap outputs are commands directly to control servos $\{\delta_f, \delta_t, \nu, \delta_{e_T}\}$ and to an attitude control subsystem $\{\phi, \theta, \psi, \omega_b\}$. These latter are Euler attitude angles and body axis components of angular velocity. Denoting a model of the aircraft engine and aerodynamic forces as:

$$\bar{a} = \hat{f}(\bar{v}, \bar{u}, \bar{p}) \tag{1}$$

where $\hat{f}$ neglects plant dynamics and is based on available data from theory, wind-tunnel tests or flight tests, then the Trimmap is a partial inverse of this model and has the form:

$$\bar{u}_c = g(\bar{ac}, \bar{v}, \bar{p}) \tag{2}$$

The Trimmap provides dynamic trimming of the aircraft because ac_r is time-varying during an approach, but it can be assumed that the bandwidth of ac_r is low compared to the bandwidth of the force dynamics and that this is imposed in the system by appropriate design of the command generator and regulator elements of the structure.

The Trimmap outputs include the attitude states required by the trajectory and these are executed by the attitude control subsystem of figure 1 using elevator, wheel, and rudder commands. Although this subsystem is not outlined in detail in figure 1, its proposed structure in reference 1 parallels that of the outer loop, with an attitude command generator to modify coarse attitude commands from the Trimmap, and an attitude regulator and moment Trimmap to track these commands with the desired attitude transient response by commanding and controlling angular acceleration.

Finally, a state estimation system completes the control loop by providing estimates $(\hat{R}_r, \hat{V}_r, \hat{a}_r, \hat{W}_r, \hat{\phi}, \hat{\theta}, \hat{\psi}, \hat{\omega}_b)$ of aircraft dynamic response to the servo commands and wind disturbances.

The proposed automatic control structure is suited to powered-lift aircraft since the element controlled by the outer loop is the combined Force Trimmap (eq. (2)) and aircraft acceleration response (eq. (1), approximately) which has a transfer function of approximately unity everywhere in the flight envelope at sufficiently low input frequencies. In that case, the regulator control law gains are fixed and the aircraft response is linear and invariant with flight condition and configuration. The nonlinearity in the control structure is that of the Trimmap (eq. (2)), but this is now an algebraic nonlinearity rather than a dynamic one. Analogous properties occur for the attitude control subsystem of reference 1 since the element controlled by the inner loop is the combined moment Trimmap and aircraft angular acceleration response, and this also has a transfer function of approximately unity.

A Trimmap for the AWJSRA is derived in this report and some simulation results are presented. Although the Trimmap is specialized to each aircraft, especially in the case of V/STOL aircraft, an effort has been made to formulate

4

concepts, problem statements, and solution methods for general applicability to powered-lift, redundantly-controlled aircraft.

A flow chart of the Trimmap computations for the AWJSRA is shown in figure 2. The runway axis-referenced acceleration command, act_r, is combined with gravity to obtain the commanded applied specific force and this is mapped into stability axis components $(A_u, A_N)_c$ along and normal to the flight path, and the roll angle, ϕ_V, which locates the normal force relative to the vertical plane. This mapping requires the velocity vector direction angles (γ_A, ψ_{VA}) and the sideslip command, β_c, if nonzero. The specific force commands (A_{u_c}, A_{N_c}) are inputs to the Basic Trimmap element of the diagram, which solves the stability axis force balance equations of the aircraft. These are the familiar lift and drag trim equations and, together with additional relationships to resolve the control redundancy, provide solutions for the required angle of attack, α_c, and the control commands $(\delta_{f_c}, \nu_c, \delta_{t_c})$. The remaining Trimmap outputs are the trim elevator and attitude commands. The trim elevator is that setting which nulls the pitch angular acceleration and is a function of the output variables of the basic Trimmap. In the attitude control subsystem, the pitch axis is controlled using variations of the elevator about this setting. The required Euler attitude angles $(\Phi_c, \Theta_c, \psi_c)$ are computed from angles associated with the trajectory velocity and acceleration and with the trim solution $(\gamma_A, \psi_{VA}, \phi_{VC}, \beta_c, \alpha_c)$ while the angular velocity command is computed approximately from the rotations of the commanded velocity vector $(\dot{\gamma}, \dot{\psi}_V)$. (More generally, the derivatives of $(\gamma_A, \psi_{VA}, \phi_V, \beta_c, \alpha_c)$ can be used to construct the required angular velocity and angular acceleration vectors.)

In general, the Force Trimmap for any STOL or CTOL aircraft can be represented as in figure 2 by changing the control variable notation as necessary. The mapping to stability axes commands and the computation of attitude commands use general kinematic relations that are aircraft-independent. Aircraft force model details appear only in the basic Trimmap; in the case of CTOL aircraft this model is relatively simple and the corresponding basic Trimmap is readily derived. For powered-lift, redundantly-controlled aircraft, model complexity is the source of the principal problems associated with the Force Trimmap; in the AWJSRA example of this report these stem principally from control redundancy. The proposed structure for dealing with this redundancy is shown in the basic Trimmap of figure 2 and consists of two elements: an automatic configuration schedule (ACS) and a trim solution algorithm. The configuration schedule is a stored schedule for two configuration controls which is calculated off-line to optimize the configuration point-by-point over the operational flight envelope subject to operational constraints on controls usage. In flight, the configuration is commanded open-loop by the ACS as a function of the commanded flight condition and thus provides optimized configuration commands along any terminal area trajectory commanded by the command generator. For the AWJSRA, the two controls that are scheduled are flap and nozzle; the flap is selected to maximize lift margin and the nozzle is selected to maximize the control margin of the remaining two controls, elevator and throttle, for use in path regulation. In flight, these latter two controls are calculated by the trim solution algorithm to generate the total acceleration command, including the corrective

5

acceleration commands from the path error regulator, at the current configuration and flight condition. In order to maximize the available control margin, the trim solution algorithm also uses the nozzle for regulation if one of the principal regulator controls saturates.

Report Outline

The basic Trimmap design problem is formulated in the next two sections. In the second section, "Trajectory Commands," the input acceleration commands and trajectory variables are derived for the various maneuvers and steady flight conditions typical of flight operations; the domain for these input variables is estimated from the kinematic constraints imposed by passenger operations and by the limits of the AWJSRA performance. The AWJSRA force model and trim equations are given, including the domains of control variables and parameters for which the model is defined or which bound the region of design interest, in the third section. In the latter section, the nature of solutions of the trim equations at a given flight condition is also examined, including their redundancy and the effect of operational constraints on controls usage in limiting the range of redundant solutions which can be employed by the Trimmap. These constraints further define the operational flight envelope of the aircraft as those flight conditions for which solutions of the trim equations exist satisfying the operational constraints. From these considerations, the Trimmap design problem is formulated and a structure is outlined for the Trimmap which includes a configuration schedule to resolve the control redundancy and a trim solution algorithm for regulation.

The trim solution algorithm is considered next. At a given flight condition the acceleration capability of the aircraft for flight-path error regulation, or control margin, is found to be a function of the configuration and the controls used by the algorithm. A structure is outlined which maximizes the control margin with respect to the controls used by the algorithm.

The configuration schedule, the main topic of this report, is developed in the next three sections. The schedule determines the operational flight envelope of the automatic system as well as the values of all configuration-dependent parameters of interest, such as control margin, attitude, fuel rate, etc., over that envelope. The development begins with a detailed examination of the operational constraints on controls usage for the AWJSRA and a selection of the parameters to be optimized by the schedule. Then, the flap schedule is calculated to provide maximum lift margin and the nozzle schedule is calculated to maximize control margin. This is done with an approximate numerical procedure which consists of enumerating solutions at a sufficient number of points covering the domains of interest of all the independent variables defining configuration and flight condition. The numerical results for the optimum configuration at each flight condition are fitted with approximating functions for use as the configuration schedule in simulation testing of the proposed control system. The analysis considers the flight envelope limits for the design and the behavior of the configuration schedule over that envelope and its effect on the remaining controls and other configuration-dependent parameters of interest.

6

Finally, the Trimmap is completed with the addition of elevator trim and attitude and angular rate command logic to the basic Trimmap and, together with the remaining control system of figure 1, is subjected to simulation testing on a STOL approach path. Behavior in response to various maneuver commands, Trimmap model errors, and wind disturbances is examined.

TRAJECTORY COMMANDS

The nature of the acceleration commands to the Force Trimmap is examined in this section. Path axes are introduced as a convenient reference frame in which to define the acceleration commands associated with aircraft maneuvers and trajectories, and in which to state the operational constraints on trajectory kinematics associated with passenger operations. On the other hand, the basic Trimmap works with the stability axis components of the applied specific force. These are functions of the trajectory commands; their relation to the path axis components of acceleration, their behavior during typical aircraft maneuvers, and their admissible ranges of values for passenger operations, which forms the Trimmap design domain, are examined.

The aircraft velocity vector, expressed in spherical coordinates, is

$$\bar{V} = V(\cos \gamma \cos \psi_V \bar{i} + \cos \gamma \sin \psi_y \bar{j} - \sin \gamma \bar{k}) \tag{3}$$

where $(\bar{i}, \bar{j}, \bar{k})$ are unit vectors defining runway axes and (V, ψ_V, γ) are the aircraft speed, heading angle, and flight-path angle (fig. 3(a)); they can be calculated from the runway axes velocity coordinates using:

$$\left. \begin{array}{l} V = \sqrt{\dot{x}^2 + \dot{y}^2 + \dot{z}^2} \\[2mm] \tan \psi_V = \dfrac{\dot{y}}{\dot{x}} \qquad \psi_V \in [-\pi, \pi) \\[2mm] \sin \gamma = -\dfrac{\dot{z}}{V} \qquad \gamma \in [-\pi/2, \pi/2] \end{array} \right\} \tag{4}$$

The acceleration vector for any trajectory can be derived from equation (3) as

$$\bar{a} = \dot{V}\underline{u} + V\dot{\psi}_V \cos \gamma \bar{m} - V\dot{\gamma}\bar{n} \tag{5}$$

where $\underline{u}, \bar{m}, \bar{n}$ are unit vectors defining the path axes (fig. 3(b)) which are oriented, respectively, tangent to the flight path and normal to the flight path in the horizontal and vertical planes.[2] They are related to runway axes by

---

[2]The underbar, $\underline{u}$, is used to distinguish the unit path tangent vector from the control vector, $\bar{u}$, used elsewhere.

$$\underline{u} = \cos \gamma \cos \psi_V \bar{i} + \cos \gamma \sin \psi_V \bar{j} - \sin \gamma \bar{k}$$

$$\bar{m} = -\sin \psi_V \bar{i} + \cos \psi_V \bar{j} \tag{6}$$

$$\bar{n} = \sin \gamma \cos \psi_V \bar{i} + \sin \gamma \sin \psi_V \bar{j} + \cos \gamma \bar{k}$$

The path axes components of $\bar{a}$ in equation (5) separate the maneuver acceleration command into terms corresponding to speed changes ($\dot{V}$), turning flight ($V\dot{\psi}_V \cos \gamma$) or, equivalently, ($V^2/R_c$), and flare or pushover maneuvers to change flight-path angle ($V\dot{\gamma}$). Maneuvers from one steady flight condition to another can be formulated as a superposition of these maneuvers and, for CTOL aircraft, maneuver accelerations along the three axes are controlled independently by engine throttle, roll attitude, and pitch attitude. The path axes are unsuited to hovering ($\bar{V} = 0$) and vertical flight ($\dot{y} = \dot{x} = 0$), for which they are undefined.

The aircraft trajectory is governed by

$$m\bar{a} = \bar{W} + \bar{F}_A + \bar{F}_E$$

where the terms on the right-hand side are weight and aerodynamic and engine forces and m is the aircraft mass. The acceleration command of interest in the Trimmap design is the applied specific force to be supplied by the engine and aerodynamic forces that the Trimmap has at its control. Given in g-units, the applied specific force command is

$$\bar{f} = \frac{(\bar{a} - \bar{g})}{g} = \frac{(\bar{F}_A + \bar{F}_E)}{w} \tag{7a}$$

where $\bar{g}$, referred to path axes, is $g(\sin \gamma, 0, \cos \gamma)^T$. The stability axis components of $\bar{f}$ are the most useful form for the Trimmap calculations and are calculated as the cylindrical coordinates of $\bar{f}$ (see footnote):[3]

$$A_u = \underline{u} \cdot \bar{f} = \sin \gamma + \frac{\dot{V}}{g}$$

$$A_N = \left| [I - \underline{u}\underline{u}^T]\bar{f} \right| = \sqrt{(\cos \gamma + V\dot{\gamma}/g)^2 + V^2/gR_c} \tag{7b}$$

$$\phi_V = \tan^{-1}\left(\frac{\bar{m} \cdot \bar{f}}{\bar{n} \cdot \bar{f}}\right) = \tan^{-1}\left(\frac{V^2/gR_c}{\cos \gamma + V\dot{\gamma}/g}\right)$$

[3]The derivation of equations (7) assumes zero nominal sideslip angle, β_c, so that the stability x-axis coincides with the velocity direction, $\underline{u}$. While this is usually the desired value of β_c, sideslip can, in general, be commanded independently of the trajectory. General formulas, which include the effect of nonzero β_c and are used in the Force Trimmap, are derived in appendix D.

8

where A_u is the longitudinal applied specific force, A_N is the applied specific force normal to the flight path, and ϕ_V is the angle of the normal specific force vector from the vertical plane. This angle is measured about the velocity vector and differs in definition from the usual Euler roll attitude angle measured about the body x-axis only by second-order effects.

Equation (7) maps the trajectory command into corresponding applied specific force commands for the Trimmap and is used in figure 4 to map a graph of (A_u, A_N) for the principal flight conditions of interest; for static equilibrium flight ($\bar{a} = 0$), equations (7) generate a unit circle as γ is varied. For steady turns ($|R_c| < \infty$), the unit circle is moved up and for steady speed changes ($\dot{V} \neq 0$) these circles move left or right by the amount $\dot{V}/g$. These constitute the flight conditions which can be held for a more or less extended period. Acceleration commands for a typical approach trajectory will consist of a sequence of such steady operating points together with the maneuvers required to pass from one steady operating point to another, such as the flare and pushover maneuvers shown in figure 5, and the example command generator output for part of an approach path shown in figure 6.

The nominal path maneuvering commands to the Trimmap are limited by the aircraft capability, passenger comfort constraints, and operating constraints for the specific aircraft (ref. 3). For the AWJSRA these limits are taken as:

$$
\left.
\begin{aligned}
&h \in [0, 3500 \text{ m}] \\
&V_A \in [45, 160 \text{ knots}] \\
&|\gamma_A| < 15° \\
&|\dot{V}| \leq 0.15 \text{ g} \\
&|V\dot{\gamma}| \leq 0.125 \text{ g} \\
&|\phi| \leq 20°
\end{aligned}
\right\} \tag{8}
$$

In the present context, these limits are assumed to be satisfied by the trajectory commands of both the ATC and the command generator. The limits on $|V\dot{\gamma}|$, $|\phi|$ are typical of passenger operations, and the remaining are estimated outer bounds of the AWJSRA flight capability and correspond to wing stall ($V_{A_{min}}$) and the extremes of total applied longitudinal specific force ($\dot{\gamma}_{min}$, γ_{max}, $\dot{V}_{min}$, $\dot{V}_{max}$). From these and equations (7) the extreme nominal specific force commands that need be considered in the present Trimmap design are therefore enclosed in a regime:

$$
\left.
\begin{aligned}
&A_u \in [-0.35, 0.35] \\
&A_N \in [0.75, 1.5]
\end{aligned}
\right\}
$$

as shown in figure 4. The most used portion of this regime for passenger STOL and CTOL operations is within ±0.2 g of level static equilibrium flight,

but other types of flight operations (helicopters, military aircraft, rockets) extend well beyond this region.

AUGMENTOR WING TRIM EQUATIONS AND TRIMMAP FORMULATION

Trim Equations

The Trimmap uses the controllable engine and aerodynamic forces to generate the commanded applied specific force. For STOL and CTOL aircraft these forces are given in stability axes and are assumed aligned in the aircraft plane of symmetry; for the AWJSRA these are expressed as

$$
\begin{pmatrix} A_u \\ A_N \end{pmatrix}_c = \frac{T_H}{W} \begin{pmatrix} \cos(\alpha + \nu) \\ \sin(\alpha + \nu) \end{pmatrix} - \frac{\dot{m}_e V_A}{W} \begin{pmatrix} 1 \\ 0 \end{pmatrix} + \frac{QS_w}{W} \begin{pmatrix} -C_D \\ C_L \end{pmatrix} \tag{9}
$$

The engine thrust is vectored through controllable exhaust nozzles (fig. 7) whose angle from the longitudinal body axis is ν. In addition, compressed cold air from the engine is exhausted through a specially designed flap (fig. 7) to augment the aerodynamic forces. The potential thrust T_C of this compressed air, obtainable by isentropic expansion to the atmosphere, is used to define the cold thrust coefficient

$$
C_J \equiv \frac{T_C}{QS_w}
$$

and the dependence of aerodynamic forces on engine power is given in terms of this coefficient; that is,

$$
\left. \begin{aligned} C_D &= C_D(\alpha, \delta_f, C_J) \\ C_L &= C_L(\alpha, \delta_f, C_J) \end{aligned} \right\} \tag{10}
$$

The engine parameters T_H, T_C, $\dot{m}_E$ are functions of the throttle setting, airspeed, and ratios of stagnation air temperature (τ) and pressure (δ) to reference sea level values:

$$
\left. \begin{aligned} T_H &= T_H(\delta_t, V_A, \tau, \delta) \\ T_C &= T_C(\delta_t, V_A, \tau, \delta) \\ \dot{m}_E &= \dot{m}_E(\delta_t, \tau, \delta) \end{aligned} \right\} \tag{11}
$$

The engine and aerodynamic model parameters listed in equations (10) and (11) are nonlinear scalar functions available as tabulated data. The modeling data used for this study are given in appendix A, and are taken from a detailed Ames simulation of the AWJSRA based on wind-tunnel and flight-test data (refs. 4,5).

The most accurate available model data are desired as the starting point for the study. Model data are usually available from simulations; their accuracy will depend on the source (theory, wind-tunnel tests, engine test stand data, flight tests) and usually improves with time as more data becomes available. Errors in the static force model affect system performance as a result of inaccurate calculation of safety margins, optimal configurations, and system flight envelope; in flight, steady-state acceleration response errors are compensated by automatic adjustment of controls from their predicted values and, if sufficiently large, induce steady position errors. On the other hand, increased complexity and computational requirements are associated with increased model accuracy and some simplification of the simulation model is desired both for off-line studies and for the on-board Trimmap. For the present study, the static force simulation model is represented to 0.01 g by the model of appendix A. This value is small relative to the assumed compensation authority of the control system so that that authority will be used in flight on the residual uncertainties of the simulation model itself.

Trim Equation Variables

Equation (9) must be solved to obtain the output of the basic Trimmap. For this purpose it is useful to sort the variables of equation (9) into

$$
\left.
\begin{array}{ll}
\text{Control variables:} & \bar{u} = (\delta_f, \nu, \alpha, \delta_t) \\[2mm]
\text{Path variables:} & \bar{x} = (V_E, A_u, A_N) \\[2mm]
\text{Parameters:} & \bar{p} = (W, \tau, \delta)
\end{array}
\right\} \tag{12}
$$

where V_E denotes the equivalent airspeed $V_A \sqrt{\rho(h)/\rho(o)}$. The aircraft model in equation (9) is defined only over a bounded domain of values of $\bar{u}$ associated with hardware limits on the controls and the availability of model data. In the present case, the aircraft model is defined for

$$
\mathcal{U}_o = \left\{ \bar{u}: \quad
\begin{array}{l}
\delta_f \in [5.6°, 72°], \\[2mm]
\nu \in [6°, 104°], \\[2mm]
\alpha \in [-10.5°, 27.5°], \\[2mm]
\delta_t \in [0°, \min\{38°, 36.3 + 143.5(\sqrt{\tau} - 1)\}]
\end{array}
\right\} \tag{13}
$$

The variable α is controlled with the elevator, whose travel is limited to

$$
\delta_{e_T} \in [-25°, 15°]
$$

The required elevator setting to trim the aircraft at any value of α can be calculated from the pitching-moment model of the aircraft. Results have been obtained for this trim setting, $\delta_{e_T}(\alpha, \delta_f, C_J)$, and are included in appendix A.

11

The path variables $\bar{x}$ are calculated from the commanded path. Their ranges of interest in the Trimmap are limited by aircraft capabilities, passenger comfort, and operational constraints as noted in the previous section. An outer bound on the regime of interest for the AWJSRA is estimated as

$$\mathscr{X}_o = \left\{x;\quad V_E \in [45,160 \text{ knots}], A_u \in [-0.35, 0.35], A_N \in [0.75, 1.5]\right\} \tag{14}$$

Not all points in $\mathscr{X}_o$ are necessarily within the aircraft capabilities defined by equations (9)-(13), and a more exact determination of these capabilities is part of the Trimmap derivation.

The weight and atmospheric parameters, $\bar{p}$, which appear in eq. (9) will also take on values over some desired domain, $\mathscr{P}_o$, within which satisfactory Trimmap operation should be provided. For the AWJSRA this domain can be taken as

$$\mathscr{P}_o = \left\{\bar{p};\quad W \in [0.95, 1.2]W_S, \tau \in [0.9, 1.1], \delta \in [0.7, 1.0]\right\} \tag{15}$$

where W_S is the standard weight value

$$W_S = 177.9 \text{ kN } (40{,}000 \text{ lbf})$$

The ranges of the atmosphere parameters in $\mathscr{P}_o$ is smaller than for passenger operations generally and reflects the aircraft's operation principally for research in a single terminal area.

In summary, aircraft trim equations, such as equation (9), can be given in the general form

$$\bar{a}_T(\bar{x}, \bar{p}, \bar{u}) = 0, \qquad \bar{u} \in \mathscr{U}_o$$

where $\bar{x}$, $\bar{p}$, $\bar{u}$ refer, respectively, to path variables, parameters, and control variables. The operational domain over which its solutions are of interest in the Trimmap is bounded and given in the form

$$\bar{x} \in \mathscr{X}_o, \qquad \bar{p} \in \mathscr{P}_o$$

Because the trim equations are often nonlinear and lack closed-form solutions, numerical procedures are necessary in the Trimmap analysis and the magnitude of the task is sized by the dimension and extent of these domains.

Control Redundancy

The trim equations are to be solved for control settings $\bar{u}$ given the flight conditions $(\bar{x}, \bar{p})$. There are, however, redundant solutions whenever the number of controls exceeds the number of equations. For the AWJSRA this excess is two,

$$\dim[\bar{u}] = \dim[\bar{a}_T] + 2$$

and there can be arbitrarily many solutions of equation (9) within the limits, $\mathscr{U}_o$. The set of all such trim solutions at a given flight condition can be formally denoted as

$$\mathscr{U}_T(\bar{x},\bar{p}) = \left\{ \bar{u} \in \mathscr{U}_o; \quad \bar{a}_T(\bar{x},\bar{p},\bar{u}) = 0 \right\} \qquad (16)$$

and the aircraft flight envelope is then all those flight conditions within the design domain, $\mathscr{X}_o$, $\mathscr{P}_o$, for which there is at least one trim solution:

$$\mathscr{F}_T \equiv \left\{ (\bar{x},\bar{p}): \quad \bar{x} \in \mathscr{X}_o, \bar{p} \in \mathscr{P}_o \text{ and } \mathscr{U}_T(\bar{x},\bar{p}) \neq 0 \right\} \qquad (17)$$

Although there are no closed form solutions of equation (9) for $\mathscr{U}_T(\bar{x},\bar{p})$, numerical solutions can be generated in sufficient quantities to produce a plot of $\mathscr{U}_T(\bar{x},\bar{p})$ for any single flight condition. Figure 8 shows such plots for two flight conditions (level flight at 120 knots and descending flight at -7.5° glidepath angle and 65 knots). Every point in these figures yields a solution by interpolating the map lines for the flap and nozzle values at that point.

Solution of the nonlinear trim equation will be required repeatedly in this analysis and in the actual flight Trimmap, so that efficient solution algorithms are significant to the derivation. Algorithms for solving the trim equation are described in appendix B.

Operational Constraints on Controls

Not all the trim solutions in $\mathscr{U}_T(\bar{x},\bar{p})$ are acceptable for actual steady flight operations as Trimmap output commands; only those which satisfy a number of operational and safety constraints on the use of controls (limits on throttle, lift margin, angle of attack, etc.) are acceptable. This reduced set of acceptable trim solutions is denoted by

$$\mathscr{U}_{TA}(\bar{x},\bar{p}) \equiv \left\{ \bar{u}: \quad \bar{u} \in \mathscr{U}_T(\bar{x},\bar{p}) \text{ and } \{f_i(\bar{u},\bar{x},\bar{p}) \geqslant 0, \quad i = 1, \ldots, N\} \right\} \qquad (18)$$

where $\{f_i\}$ are all the operational constraints that the Trimmap output must satisfy in flight for the particular aircraft. These are listed in detail for the AWJSRA in the next section. The effect of imposing these constraints on the trim solution sets $\mathscr{U}_T$ previously given for two flight conditions is shown in figure 9. As seen, $\mathscr{U}_{TA}$ is considerably reduced from $\mathscr{U}_T$ in both cases.

Operational criteria for powered-lift aircraft are less well defined than for CTOL aircraft and are the subject of recent and ongoing studies at Ames (refs. 6-8). The criteria used in the present study are taken from current AWJSRA research flight operations and, in their details, are unique to the AWJSRA. However, constraints of the type given and their effect on the design method would occur for aircraft generally. A minimum requirement for the constraint list used in the computations is that it comprises sufficient conditions for operational acceptability of trim solutions.

The operational flight envelope for the aircraft within the design domain is that set of flight conditions for which at least one trim solution acceptable for steady flight is available; that is,

$$\mathscr{F}_{TA} \equiv \left\{ (\bar{x},\bar{p}): \quad \bar{x} \in \mathscr{X}_o, \bar{p} \in \mathscr{P}_o, \text{ and } \mathscr{U}_{TA}(\bar{x},\bar{p}) \neq 0 \right\} \qquad (19)$$

Thus, the constraints define the limits of operationally acceptable flight as well as restrict the acceptable trim solutions at any point within $\mathscr{F}_{TA}$.

Trimmap Formulation

A functional description of the Trimmap element of figure 1 can be given in greater detail. The Trimmap function is to solve the aircraft trim equations for a unique control command, $\bar{u}_c$, given the path commands $\bar{x}_c$ and current parameter values $\bar{p}$. Over the operationally acceptable flight envelope $\mathscr{F}_{TA}$ it resolves the control redundancy by selecting an optimum trim solution subject to constraints on controls usage. If the Trimmap obtained in a design is denoted as the map

$$\bar{u}*(\bar{x},\bar{p}): \quad \mathscr{F} \to \mathscr{U} \qquad (20)$$

then that design will achieve some corresponding operationally acceptable flight envelope

$$\hat{\mathscr{F}}_{TA} \equiv \left\{ (\bar{x},\bar{p}): \quad \bar{x} \in \mathscr{X}_o, \bar{p} \in \mathscr{P}_o, \bar{u}*(\bar{x},\bar{p}) \in \mathscr{U}_{TA}(\bar{x},\bar{p}) \right\} \qquad (21)$$

and complete flight envelope

$$\hat{\mathscr{F}}_T \equiv \left\{ (\bar{x},\bar{p}): \quad \bar{x} \in \mathscr{X}_o, \bar{p} \in \mathscr{P}_o, \bar{u}*(\bar{x},\bar{p}) \in \mathscr{U}_T(x,p) \right\} \qquad (22)$$

At best, these are equal, respectively, to $\mathscr{F}_{TA}$ and $\mathscr{F}_T$ (eqs. (17) and (19)) but are usually smaller than those two sets as a result of approximations and simplifications made in the design process. An objective of the Trimmap design is to maximize $\hat{\mathscr{F}}_{TA}$ and $\hat{\mathscr{F}}_T$ since these are outer limits on the flight capabilities of the autopilot-aircraft combination.

The basic structure of the proposed Trimmap logic is shown in figure 10. Two principal elements are used: a configuration schedule and a trim solution algorithm. This structure assumes that an optimum trim solution satisfying the operational constraints for steady flight, $\bar{u}*(\bar{x},\bar{p})$, has been calculated off-line and solutions from $\bar{u}*$ for two of the controls, (u_1, u_2), are stored on-board as the configuration schedule. In flight, the configuration schedule commands these two controls on the basis of the nominal trajectory commanded by the command generator; that is, these two controls are driven open-loop by the nominal trajectory command. The remaining two controls, (u_3, u_4), are calculated by solving the two trim equations using the current parameter values $\bar{p}$ and $\bar{x}_c$, where $\bar{x}_c$ differs from $\bar{x}_o$ by the amount of the corrective acceleration command from the trajectory regulator. These two controls are in the feedback line and are termed regulator controls here. Their command values

14

will differ from their nominal values in $\bar{u}^*(\bar{x}_o,\bar{p})$ to the extent that path errors are nonzero.

Further details of the above structure applied to the AWJSRA are shown in figure 10(b). Flap and nozzle have been selected as configuration controls. Their stored schedules, $F^*(\bar{x})$ and $\nu^*(\bar{x})$ do not include the parameters $\bar{p}$ as independent variables but, instead, the configuration schedule is optimized for a standard set of values, $\bar{p}_s$, given by

$$W_s = 177.9 \text{ kN}$$

$$\tau_s = 1$$

$$\delta_s = 1$$

This simplification is reasonable in view of the narrow regime of parameter values $\mathscr{P}_o$ over which the AWJSRA is operated. In flight, the trim solution algorithm adjusts the regulator controls for nonstandard parameter values, but some reduction in the design envelope $\hat{\mathscr{F}}_A$ is traded for the simplification. Of the four controls, only the flap actuator response is too slow for use in path regulation but any pair of controls from $\{\nu,\ \alpha,\ \delta_t\}$ or even all three controls can be used as regulator controls. The pair $(\alpha,\ \delta_t)$ is used in CTOL aircraft and was also found suitable for AWJSRA operations as the basic regulator mode throughout its flight envelope. However, the use of all three controls provides greater regulator control power than is available for any single pair, and the trim solution algorithm is modified to utilize the nozzle control when the basic regulator mode saturates, as discussed in the next section.

The basic Trimmap outlined in figure 10(b) is that element of the Force Trimmap of figure 2 that deals with the solution of the two trim equations, equation (9). This element encompasses the principal design problems regarding nonlinearity and trim solution redundancy. Additional functions are required in the Force Trimmap to map input acceleration commands into stability axis components (eqs. (6) and (7)), to provide the elevator trim setting that balances out pitching moments at the commanded configuration (appendix A), and to provide appropriate attitude commands that orient the applied forces correctly in inertial space (appendix D).

STRUCTURE OF THE TRIM SOLUTION ALGORITHM

Three of the AWJSRA's controls are suitable for path error regulation. In general, the control margin available for the regulation function differs with the control pair used and the three controls $(\delta_t,\ \nu,\ \delta_e)$ collectively provide more control margin than is available from any single pair. Thus, to obtain maximum control margin the trim solution algorithm must use all three controls. This section includes a discussion of the regulator control margin and outlines a regulator control logic for the AWJSRA that uses all three controls.

The acceleration capability or control regime of the regulator controls at a given configuration $\{\delta_f, \nu\}$ and parameter values $\bar{p}$ can be calculated as those accelerations that can be generated in equation (9) by moving the regulator controls over their permitted ranges of use for regulation; that is, if $\{\alpha, \delta_t\}$ are the regulator controls (fixed nozzle mode) then the control regime is the envelope of accelerations filled out by

$$\mathscr{A}_{\delta_f,\nu}(V_E,p) = \left\{(A_u,A_N); \quad \delta_t \in [\delta_{t_{min}},\delta_{t_{max}}], \alpha \in [\alpha_{min},\alpha_{max}], \bar{a}_T(\bar{x},\bar{p},\bar{u}) = 0\right\}$$

(23)

It is understood in equation (23) that $\{\delta_f, \nu, V_E, \bar{p}\}$ are given and that $\{\alpha, \delta_t\}$ are varied through their permitted ranges for regulation, $[\delta_{t_{min}}, \delta_{t_{max}}]$, $[\alpha_{min}, \alpha_{max}]$. The numerical values of these limits on control usage are listed in the next section along with other constraints. The control regime is illustrated in figure 11 for glide slope conditions.

Control regimes for other regulator control pairs or for all three controls can be defined analogously

$$\mathscr{A}_{\delta_f,\delta_t}(V_E,p) \equiv \left\{(A_u,A_N); \quad \nu \in [\nu_{min},\nu_{max}], \alpha \in [\alpha_{min},\alpha_{max}], \bar{a}_T(\bar{x},\bar{p},\bar{u}) = 0\right\}$$

$$\mathscr{A}_{\delta_f,\alpha}(V_E,p) \equiv \left\{(A_u,A_N); \quad \nu \in [\nu_{min},\nu_{max}], \delta_t \in [\delta_{t_{min}},\delta_{t_{max}}], \bar{a}_T(\bar{x},\bar{p},\bar{u}) = 0\right\}$$

$$\mathscr{A}_{\delta_f}(V_E,p) \equiv \left\{(A_u,A_N); \quad \nu \in [\nu_{min},\nu_{max}], \delta_t \in [\delta_{t_{min}},\delta_{t_{max}}],\right.$$
$$\left. \alpha \in [\alpha_{min},\alpha_{max}], \bar{a}_T(\bar{x},\bar{p},\bar{u}) = 0\right\}$$

(24)

These different control regimes are compared in figure 12 for glide slope conditions; it is apparent that the control regime for all three controls includes and is significantly larger than the regimes of any of the two-control regulators.

A method of measuring the control margin associated with such irregular figures is necessary for the configuration optimization analysis of this report which attempts to maximize the control margin at all operating points. The control margin at a nominal operating point (A_{u_o}, A_{N_o}) is defined as the radius of the largest ellipse of the form

$$R^2 = \sigma^2(A_u - A_{u_o})^2 + (A_N - A_{N_o})^2$$

(25)

which can be inscribed in the acceleration envelope. This is illustrated by the ellipse in figure 11 which is centered at the glide slope operating point. The definition of control margin contains a selectable parameter σ which is the axis ratio of the ellipse. It represents a weighting of normal acceleration relative to longitudinal acceleration in measuring control margin and

16

was selected for this study as the ratio of minimum acceptable acceleration margins for the normal and longitudinal axes

$$\sigma = 5$$

This value reflects the approximate ratio of disturbance accelerations and corresponding corrective acceleration activity of the path regulator for the two axes which results from the high lift-drag ratios, on the order of 5 to 10, for aircraft. To formalize the definition of control margin, note that the region occupied by an ellipse of the form of equation (25) is

$$\mathscr{E}\left(R, A_{u_O}, A_{N_O}\right) = \left\{(A_u, A_N): \quad 5^2\left(A_u - A_{u_O}\right)^2 + \left(A_N - A_{N_O}\right)^2 \leqslant R^2\right\} \tag{26}$$

and the control margin at a given flight condition and configuration is then

$$CM_{\delta_f, \nu}(\bar{x}_O, \bar{p}) \equiv \max\left\{R: \quad \mathscr{E}\left(R, A_{u_O}, A_{N_O}\right) \subset \mathscr{A}_{\delta_f, \nu}(V_{E_O}, \bar{p})\right\} \tag{27}$$

A method for generating the figures $\mathscr{A}_{\delta_f}, \mathscr{A}_{\delta_f, \nu}$, etc., and calculating control margins is described in appendix C.

Control margins for the other regulator modes and for the three-controller mode are defined analogously

$$\left.\begin{array}{l} CM_{\delta_f, \delta_t}(\bar{x}_O, \bar{p}) = \max\left\{R: \quad \mathscr{E}\left(R, A_{u_O}, A_{N_O}\right) \subset \mathscr{A}_{\delta_f, \delta_t}\left(V_{E_O}, \bar{p}\right)\right\} \\[12pt] CM_{\delta_f, \alpha}(\bar{x}_O, \bar{p}) = \max\left\{R: \quad \mathscr{E}\left(R, A_{u_O}, A_{N_O}\right) \subset \mathscr{A}_{\delta_f, \alpha}\left(V_{E_O}, \bar{p}\right)\right\} \\[12pt] CM_{\delta_f}(\bar{x}_O, \bar{p}) = \max\left\{R: \quad \mathscr{E}\left(R, A_{u_O}, A_{N_O}\right) \subset \mathscr{A}_{\delta_f}\left(V_{E_O}, \bar{p}\right)\right\} \end{array}\right\} \tag{28}$$

Values of these control margins, measured in g's, are noted in figure 12 for the various modes and it is apparent that the three-controller regulator has the largest margin.

A conclusion drawn here is that the regulator logic must use all three controls in order to realize the maximum available control margin. One method of implementing this for the AWJSRA is to use the fixed nozzle regulator near the nominal operating point but to switch to an alternative mode which varies the nozzle whenever one of the controls $\{\alpha, \delta_t\}$ is saturated at an extreme permitted value. A corresponding mode-switching diagram for the glide slope case is shown in figure 13; the control regime $\mathscr{A}_{\delta_f}$ is subdivided into regions in which one or another of the three controls is held fixed. A flow diagram for the corresponding trim solution algorithm is shown in figure 14.

The fixed-nozzle mode is selected in the present study as the control mode used near the nominal operating point, or *central regulator mode*. The

configuration optimization will be aimed in part at maximizing the control margin of the central mode in order to minimize control activity and the likelihood of saturating the controls of the central mode. The fixed nozzle mode uses the same pair of control variables as is used for regulation in CTOL aircraft and is obviously appropriate for the AWJSRA in its conventional cruise configuration. The present Trimmap extends this mode throughout the AWJSRA flight envelope and attempts to preserve good control power and acceptable sensitivity into the low-speed STOL regime and powered-lift configuration. It does this by selecting the configuration to maximize the control margin of the central mode and by resorting to the use of the third control when the central mode saturates. More generally, alternative choices of central mode can be considered in regions of the flight envelope where improved control margin is both needed and available from an alternative mode. It should also be noted that, while the multiple mode structure of figure 14 realizes the maximum available control margin, further improvements in control sensitivity should be available with an algorithm which uses all three controls simultaneously for regulation, but such an algorithm is outside the scope of the present work.

CONFIGURATION OPTIMIZATION

The configuration schedule is to be derived off-line and stored on-board and the derivation seeks to optimize the configuration subject to the operational constraints on controls usage for the aircraft. This section describes the AWJSRA constraints and the optimization procedure used.

Operational Constraints for the AWJSRA

The operational constraints which bound the acceptable control settings for steady flight and for regulator usage are discussed below and listed in figure 15(a). These are limits on the extremes of each control or on functions of the controls. Many details of the constraints are unique to the AWJSRA and its operations as a research aircraft, but the list is expected to be representative of most powered-lift aircraft in terms of length, complexity, and type of functions to be bounded. Criteria for civil operation of powered-lift STOL aircraft are under development (refs. 6-8).

The flap range is bounded by hardware limits and by a structural placard on the maximum value which is a function of equivalent airspeed (fig. 15(b)):

18

$$\delta_{f_{max}}(V_E) = \min\left\{65, \max\{3(106.7 - V_E), 0.66(165.5 - V_E), 5.6\}\right\} \qquad (29)^4$$

Throttle servo stops have been installed on the aircraft to limit the extremes used during automatic flight control; the minimum stop is operated by the flap setting and is satisfied in the present design by the continuous piecewise linear function (fig. 15(c)):

$$\delta_{t_{min}}(\delta_f) = \min\left\{17.6, \max\{0.553(\delta_f - 13.2), 9.3\}\right\} \qquad (30)$$

This minimum is well above the engine idle setting and is selected to limit the emergency power recovery time from minimum throttle. Shorter recovery time is required for flaps-down powered-lift configurations than otherwise. The maximum throttle setting for nominal or steady flight conditions is equivalent to the maximum continuous power setting established for the engine:

$$\delta_{t_{max,NOM}} = 25.6° \qquad (31)$$

This is the upper limit imposed on throttle settings in the configuration schedule derivation. Temporarily higher settings are permitted for the regulation function and for takeoff; this upper limit is implemented by one of the servo stops. In addition, the maximum throttle is further reduced on cold days due to a structural limit on the thrust force which the engine nozzles can support when nozzles are down. Combining these limits gives (fig. 15(d)):

$$\delta_{t_{max,REG}}(\tau, \delta) = \min\left\{29.4, 136.6\sqrt{\tau}\ (0.705 + 0.295/\delta) - 107.174\right\} \qquad (32)$$

Nozzles are limited simply by their hardware extremes as noted in figure 15(a).

The lift margin at a given flight condition $(\bar{x}, \bar{p})$ and control setting $\bar{u}$ is the amount of lift force acceleration that can be generated by increasing α to its stall or maximum permitted value; that is,

$$LM(\bar{x}, \bar{p}, \bar{u}) \equiv \frac{QS_w}{W}\left[C_{L_{max}}(\delta_f, C_J) - C_L(\alpha, \delta_f, C_J)\right] \qquad (33)$$

The lift margin reflects both α-margin from stall and speed-margin from its minimum value for equilibrium flight at the given flap, power and nozzle settings; therefore, it measures the tolerance of the aircraft at $(\bar{x}, \bar{p}, \bar{u})$ to vertical gusts, windshears and speed control errors as well as the ability

---

[4]The use of minimum and maximum functions, as in equation (29), provides a conveniently compact notation for representing piecewise linear functions in one or more variables. Functions of one variable, such as equation (29) are, however, more easily visualized in the standard notation; for example,

$$\delta_{f_{max}}(V_E) = \begin{cases} 65 & V_E \leqslant 85 \\ 3(106.7 - V_E) & V_E \in [85, 90] \\ 0.66(165.5 - V_E) & V_E \in [90, 157] \\ 5.6 & V_E \geqslant 157 \end{cases}$$

to flare the aircraft from $(\bar{x}, \bar{p}, \bar{u})$ using attitude changes only. A minimum value of lift margin is required at all nominal flight conditions and, for the AWJSRA, suitable margins established from flight experience are 0.69 g in the flaps-up configuration and 0.4 g in flaps-down ($\delta_f \geqslant 30°$) powered-lift configurations. These requirements are satisfied by the constraint:

$$LM(\bar{x},\bar{p},\bar{u}) \geqslant \max\left\{0.4,\min\{0.69,0.0119(63.66 - \delta_f)\}\right\} \tag{34}$$

The value of 0.69 g matches the usual speed margin of 30% required for CTOL aircraft. In a powered-lift configuration, however, lift can be generated from engine power increases as well as from angle of attack increases and a lower fixed-power lift margin can be comfortably permitted provided a fixed-power flare is possible (ref. 7).

The lift-margin constraint limits the acceptable control settings at a given flight condition. It can also be viewed as placing an upper bound on the nominal value of α as a function of $\{\delta_t, \delta_f, \bar{x}, \bar{p}\}$ or as establishing the the minimum operating speed boundary of the flight envelope. This boundary is shown in figure 15(e) for values of $\{\delta_t, \delta_f, \bar{x}, \bar{p}\}$ representative of the approach flight regime.

The constraints on pitch attitude listed in figure 15(a) are approximate limits favored by pilots. They are imposed in computing the configuration schedule by corresponding approximate constraints on $\alpha(\bar{x}, \bar{p})$; assuming

$$1. \quad \alpha = \Theta - \gamma$$

$$2. \quad \gamma = \sin^{-1}(A_u)$$

Then the limits on α for nominal flight conditions are

$$\alpha_{NOM} \in [-10° - \sin^{-1}(A_u),15° - \sin^{-1} A_u] \tag{35a}$$

Secondary effects of roll angle are neglected in (1) above and γ has been calculated from A_u assuming $\dot{V}$ is null. More generally, if $\dot{V}$ is nonzero then, in the extreme cases, equation (35a) implies

$$1. \quad \text{If} \quad \alpha = \alpha_{NOM,min} \quad \text{then} \quad \Theta \geqslant \Theta_{min} \quad \text{for} \quad \dot{V} \leqslant 0$$

$$2. \quad \text{If} \quad \alpha = \alpha_{NOM,max} \quad \text{then} \quad \Theta \leqslant \Theta_{max} \quad \text{for} \quad \dot{V} \geqslant 0$$

and this ensures the pitch attitude constraints in most operational situations with nonzero $\dot{V}$. In addition, the constraint on touchdown attitude is imposed by requiring

$$\alpha_{NOM} \geqslant 2° - \sin^{-1}(A_u) \tag{35b}$$

at those values of $\{A_u, V_E\}$ for which touchdown can occur.

In flight, the regulator varies angle of attack around its nominal value; an upper bound to prevent stall by the regulator is established as

20

$$\alpha_{max,REG}(V_E) = \min\{0.1667(V_E + 10), 15\} \tag{36}$$

This limit is used in calculating the control margin of a given configuration and provides a margin from the stall angle of attack that gives at least 0.15 g of lift margin unused by the autopilot in the case of approaches at maximum flap setting. These boundaries are shown in figure 15(e).

In flight, path errors are corrected by varying the regulator controls around their nominal values given from the configuration schedule. Consequently, the choice of configuration controls must allow sufficient margins from the boundaries of aircraft acceleration capability for use by the regulator controls. Lower limits on these margins were taken as

$$\left.\begin{array}{ll} \text{Longitudinal acceleration margin} & \pm 0.05 \text{ g} \\[1em] \text{Normal acceleration margin} & \pm 0.25 \text{ g} \end{array}\right\} \tag{37}$$

From equation (7) and the lift force expression it can be calculated that these values allow for corrective flight-path variations of $\pm 3°$ or speed corrections at ± 0.05 g and can accommodate horizontal gusts of 13%-15% of the airspeed without exceeding the margins. In terms of the control margin measure defined in equations (25) and (28), the above acceleration margin limits are given by the constraint

$$CM_{\delta_f}(\bar{x}_o, \bar{p}) \geqslant 0.25 \text{ g}$$

This is the minimum acceptable margin when all three regulator controls are considered. The control margin of the central regulator mode, which uses only two controls, can be less than this value. In the glide slope case previously shown in figure 12 the desired control margin is available using all three controls but not for any choice of two-controller modes.

The elevator is used to execute angle of attack commands from the Trimmap and to regulate pitch attitude errors. A trim elevator setting associated with the nominal flight condition, and calculated as that elevator setting that trims out all pitching moments due to engine and aerodynamic forces, is derived in appendix A. In the present configuration schedule computations a margin of 8° from the limits of elevator travel was imposed on the associated trim elevator setting

$$\delta_{e_T}(\bar{x}, \bar{u}) \in [-17°, 7°]$$

in order to provide some margin for the regulation functions.

The configuration schedule is derived by identifying the operationally acceptable range of choice of configurations for steady flight (eq. (18)) and then determining a unique choice that optimizes some parameter of interest. The range of acceptable configurations is defined by constraints on controls usage, such as those listed in figure 15(a) for the AWJSRA. These constraints considerably reduce the range of choice compared to the full set of trim solutions and also impose gross variations of configuration over the flight

envelope. Both of these effects can be seen in the two examples previously illustrated in figure 9.

Configuration Selection

Schedules for the flap and nozzle settings are to be determined over the flight envelope. Schedules that optimize control characteristics are computed next in two successive steps using the criteria:

1. Select the maximum acceptable flap angle

2. Select nozzle angle to maximize the regulator control margin

The maximum flap is selected within the acceptable range of choice and can be calculated independent of any particular choice of nozzle schedule. This flap selection criterion maximizes the lift margin, which is a strong function of flap. It emphasizes safety and control in the low speed approach regime and is also favorable for fuel requirements in this regime. This occurs because flap and throttle provide lift margin interchangeably there so that a higher flap setting permits a lower range of throttle settings for trim (e.g., see fig. 9(b)).

After the flap schedule is determined, the nozzle is selected to maximize the control margin of the central regulator. This margin depends strongly on the nozzle setting at any given flight condition and flap setting. This selection criterion minimizes control sensitivity and saturation of the central mode, but does not affect the control margin available for all three controls, CM_{δ_f}.

An additional step is useful to adjust the schedules derived from the above procedure. After the variations of all parameters over the flight envelope

$$F^*(x), \ \nu^*(x), \ \delta_t^*(x), \ \alpha^*(x), \ . \ . \ .$$

are obtained, the scheduled controls can be adjusted for any engineering requirements for smooth or monotonic variations, or for special restrictions on controls in restricted regions or for certain maneuvers.

The configuration selection procedure is carried out empirically in the next two sections; the magnitude of the computational task is reduced in the stated procedure by optimizing the flap and nozzle schedules in sequence rather than simultaneously; this is based on the special properties that the parameters to be optimized are each strongly dependent on only one of the configuration controls, and that the flap schedule can be optimized independent of the nozzle setting. These specializations reduce the domain of search in the optimization; but their effect on the margins obtained is expected to be small.

The configuration selection rules used emphasize control characteristics on the assumption that lift margin and control power are marginal in much of

the low-speed STOL approach regime. A major objective of the configuration scheduling is then to maintain acceptable control characteristics and to realize as much of the potential operating envelope of the aircraft as is possible in this marginal regime. A second generation design can be expected to integrate fuel and noise considerations into the optimization by trading excess lift or control margin obtained in the present design in some regions of the flight envelope for reduced fuel rate and noise.

FLAP SCHEDULE

The flap schedule to be used in the ACS is described in this section. The computations are done in two steps; first, the range of admissible flap settings is determined at each of a number of operating points covering the trajectory envelope of interest, $\mathscr{X}_O$, and then a unique setting is defined at each point and a function fitted to these values for use in the ACS design. The flap schedule given here is approximately the maximum admissible flap at each point in $\mathscr{X}_O$. The influence of flap servo rate limits on the design of the flap schedule is also analyzed.

Admissible Flap Settings

At a given flight condition, $(\bar{x}, \bar{p})$, the admissable flap settings are those values for which at least one acceptable trim solution exists. An algorithm that was used to calculate these flap settings at a sufficient number of points is outlined in appendix C. The procedure is entirely empirical; a grid of values of flap settings is tested at a given flight condition and then this is repeated for a grid of values of $(\bar{x}, \bar{p})$ covering the flight conditions of interest.

Results are shown in figures 16(a)-(g) as a series of plots of the admissible flap range for several positive values of A_u (climbing or accelerating flight) and negative values of A_u (descending or decelerating flight). The standard parameter values and a value of 1 g for A_N were used in these calculations. The upper bound on the admissible flap range is limited by the flap placard and, at high values of A_u, by the control margin. The lower bound is dictated at low speeds by the lift margin constraint.

Flap Selection

The rationale for flap scheduling is given below and is basically a generalization of conventional flap usage. First, the flap schedule will be given as a function of only two of the variables of $(\bar{x}, \bar{p})$:

$$F^* = F^*(V_E, A_u) \tag{38}$$

This choice provides for the major trends in conventional flap usage; that is, flaps are lowered with decreasing speed in order to maintain lift margin with the higher maximum lift coefficients of the flaps-down configuration. Second,

flaps are raised with increasing flight-path angle (or A_u) and with increasing speed in order to avoid the induced drag penalty of the flaps-down configuration which must be overcome by engine thrust.

Third, the flap will be scheduled to give the maximum admissible flap setting, or equivalently, to maximize the lift margin. This choice matches current practice with the AWJSRA in the approach regime and minimizes angle of attack with respect to flap setting. It is unfavorable for fuel requirements at higher speeds but favorable at lower speeds so that a minimum fuel design would differ from the present design in some regions of the flight envelope. Lift margin is an appropriate control characteristic to optimize in the flap selection since it is a strong function of flap. Optimization of the control margin, $CM_{\delta f}$, was also considered since it is a function of the flap angle and is independent of the nozzle selection, but it was found that $CM_{\delta f}$ was insensitive to flap setting.

The effect of flap choice on the remaining controls of the trim solution is illustrated for two flight conditions in figure 9. The flap selection removes one degree of redundancy and narrows the remaining choice to a single constant flap line in figure 9. In the glide slope case the maximum flap provides the widest choice of acceptable trim solutions, the minimum throttle and fuel rate, and the minimum α and maximum lift margin compared to other flap values. In the higher speed case the lowest throttle setting occurs at minimum flap. In both cases the usual interchange between flap and angle of attack as lift generators is evidenced by the nearly parallel flap contours and, more generally, is present independent of configuration and flight condition. At low speeds engine power is also used to generate lift and a similar flap-throttle interchange occurs while at high speeds the conventional relation between flap and throttle setting due to the induced drag variation with flap is obtained.

Flap Schedule

The flap schedule will be given in the form of a piecewise linear function suitable for use in the Trimmap. This function was derived to fit the maximum admissible flap within the domain of $\bar{x}$ for which a nonzero range of admissible flap settings is available; outside this domain the fitted function extends linearly. The errors in fitting the maximum admissible flap are designed to maintain the scheduled flap inside its admissible range over as much of the flight regime as possible. The schedule is

$$F^*(A_u, V_E) = \min\{F_{UB}(A_u), \max\{F_1(A_u, V_E), 5.6\}\}$$

where

$$F_{UB}(A_u) = \min\{65, \max\{538.5(0.1207 - A_u), 30\}\}$$

$$F_1(A_u, V_E) = \begin{cases} 140 - V_E & V_E \leqslant 90 \text{ knots} \\ F_{90}(A_u) + 0.6627(90 - V_E) & V_E > 90 \text{ knots} \end{cases}$$

$$F_{90}(A_u) = \min\{50, \max\{333.3(0.215 - A_u), 30\}\}$$

(39)

In form, F* is a generalization of the flap placard function (eq. (29)), which is a linear function of V_E limited by the flap extremes; in F*, the parameters of that form have been made functions of A_u.

The variation of F* with V_E is given in figure 16(h) for several breakpoint values of A_u; the parameters defining this variation are linear functions of A_u between these values. Plots of F* are also superposed on the admissible flap ranges in figure 16(a)-(g) and it is seen that there is almost no loss of acceptable flight envelope by the fitted function, F*. The parameters of F* are based principally on the standard case data (fig. 16) and therefore fit that case best. However, they have also been adjusted to maximize the acceptable flight envelope for values of A_N other than 1.0 and in order to adjust the implied pitch attitudes in some regions of the envelope.

The complete flap schedule is shown by a contour plot in figure 17. The expected trends are visible; that is, F* decreases monotonically with increasing V_E or A_u. The variation with V_E is independent of A_u for negative values of A_u. Thus, pull-up to level flight from any steady descent is executed without flap configuration changes at any speed. For positive values of A_u flap reduces with A_u to a speed-dependent minimum value. The flap schedule F* is defined at all flight conditions both inside and outside the acceptable flight envelope, as seen in figure 17, even though it is fitted only to data inside that envelope. Inadvertent excursions of the aircraft outside the acceptable flight envelope enter a marginal region in which trim solutions exist but are unacceptable for steady flight. Owing to its linearity, the schedule, (eq. (39)), provides a marginal region of adequate size to accommodate such excursions.

Flap Command Rates

In the design process discussed in the previous section, and in the design of F* so far described, the scheduling problem is treated as one that can be solved independently at each point in the flight envelope assuming that each point is a steady or quasi-steady flight condition. The transient variations of $\bar{u}_c$ necessary to go from one steady flight condition to another were not considered nor were control rate constraints imposed on the schedule. However, the control servo actuators are usually rate or bandwidth limited and transient control lags will occur during maneuvers if this limit is saturated. In general, if $\bar{x}_c(t)$ is the commanded history of flight conditions for any maneuver or trajectory within the domain of interest, and the Trimmap is represented as $u*(\bar{x})$, then the corresponding commanded control rates are given by

$$\dot{u}_c = \left[\bar{\nabla}_{\bar{x}} u*(\bar{x}_c) \right] \dot{\bar{x}}_c$$

These rates depend on both the maneuver and the Trimmap's configuration schedule.

The AWJSRA flap is the slowest of the controls and has the rate limit

$$\left| \dot{\delta}_f \right|_{max} = 3.5°/sec \qquad (40)$$

25

The flap command rates in maneuvering flight implied by the flap schedule are

$$\frac{d\delta_{f_c}}{dt} = \frac{\partial F^*}{\partial V_E} \dot{V} + \frac{\partial F^*}{\partial A_u} \dot{A}_u \tag{41}$$

The partials of F^* are piecewise constant and are shown in figure 18. The maximum maneuver command rates from the command generator are obtained from equations (7) and (8) as

$$|\dot{V}| \leqslant 0.1 \text{ g}$$

$$|\dot{A}_u| \cong |\dot{\gamma}| \leqslant \frac{0.125 \text{ g}}{V}$$

For speed-change maneuvers the flap rate limit is saturated if

$$\left| \frac{\partial \delta_{f_c}}{\partial V_E} \right| = \frac{|\dot{\delta}_f|_{max}}{|\dot{V}|_{max}} = 1.8 \text{ deg/knot}$$

Since $|\partial F^*/\partial V_E|$ is less than this value at all flight conditions (fig. 18(a)), the use of F^* will not saturate the flap rate limit as a result of speed changes. The rate of change of A_u is due primarily to commanded flight-path angle rates. Since γ is confined to small angles, maximum values of $\dot{A}_u$ can occur only briefly and some flap rate saturation can be tolerated during flight-path angle changes. The value of the partial for which rate saturation occurs is

$$\left| \frac{\partial \delta_{f_c}}{\partial A_u} \right| = \frac{|\dot{\delta}_f|_{max}}{|\dot{A}_u|_{max}} = V_E \text{ deg/g}$$

The partial of F^* exceeds this limit by factors of 3 to 10 in those regions where the partial is nonzero (fig. 18(b)). Flap lags as high as 15° have occurred in simulated maneuvers. However, the Trimmap is designed to avoid maneuver execution errors during configuration lags by using the actual flap value in the trim solution algorithm rather than the commanded flap (see fig. 10(b)). This provides automatic adjustment of the regulator controls to compensate for flap lag so that the maneuver acceleration commands are accurately followed.

To summarize, configuration control rate limits are of consequence only during maneuvering,

$$\dot{x}_c \neq 0$$

since this is the only occasion for significant nominal control activity, $\dot{u}_c \neq 0$. The effect of rate-limit saturation is control lag and a possible loss of acceptability of the resulting nonscheduled configuration. This should be prevented for long duration maneuvers by limiting the appropriate schedule gradient in accordance with maneuver limits of the command generator and the control rate limit. For short duration maneuvers configuration lag can be temporarily tolerated but must be correctly compensated by the regulator controls in order to obtain adequate tracking of the maneuver commands.

26

NOZZLE SCHEDULE

The nozzle schedule to be used in the Trimmap is derived in this section. The nozzle is scheduled to maximize the control margin of the fixed-nozzle regulator, $CM_{\delta_f \nu}$, everywhere in the acceptable flight envelope. A computer-generated solution for the optimum nozzle, $\nu^*(x)$, is given first and then a fitted function to be implemented in the airborne computer, $\hat{\nu}^*(x)$, is given along with contour plots of the corresponding values of the other controls and parameters of interest which depend on the configuration schedule. The optimization calculations are carried out at the standard parameter values.

Optimum Nozzle Angle, ν^*

The computational procedure used to generate the nozzle setting for maximum control margin is outlined in appendix C. The effect of nozzle setting on control margin is illustrated in figure 19 for the glide slope case; the control regimes for several values of nozzle angle along with the glide slope operating point are shown. The control margin at a given nozzle angle is related to the minimum distance from the operating point to the boundary of the corresponding control regime; as seen in figure 19, this distance is strongly dependent on nozzle angle, and is even undefined at the highest and lowest nozzle angles for which the control regimes do not enclose the operating point.

The effect of nozzle angle on control margin is seen more generally in figure 20 for various values of A_u at low speed and at cruise speed (65 and 160 knots). The curves are dashed outside the range of acceptable trim solutions which is limited by bounds on lift margin, throttle, or attitude. In the low speed case (fig. 20(a)), definite control power maxima occur at each A_u, and the optimum nozzle angle increases with decreasing A_u. The conventional minimum-nozzle configuration is not within the acceptable range at any value of A_u at this speed so that the aircraft requires vectored thrust to fly acceptably at this speed. In some cases the maximum occurs outside the acceptable range due to insufficient lift margin and a constrained optimum nozzle value with lower control margin must be selected. The corresponding throttle is seen to be the minimum for the acceptable range of solutions and the optimum solution at this speed has the minimum lift margin.

At cruise speed (fig. 20(b)) there is considerably greater control margin than at 65 knots, but the curves again have definite maxima. These occur on the nozzles-up boundary at level and climbing flight and at higher nozzle angle for all descending or decelerating flight. The unconstrained optimum nozzle is now within the acceptable range and can be selected. However, the corresponding throttle setting is higher than at lower acceptable choices of the nozzle angle and, at this speed, some control margin could be traded for lower fuel rates by selecting lower nozzle angles. The required throttle increases with nozzle angle at all flight conditions shown in figure 20 and this relationship between throttle and nozzle occurs generally at other flight conditions.

The use of thrust vectoring is not actually required at cruise speed by the operational constraints except for very steep descent or to generate maximum deceleration.

A contour plot of the optimized nozzle angle ν^* is shown in figure 21(a). This is plotted for normal specific force at 1 g, which corresponds closely to static equilibrium flight conditions. The contours are roughly parallel and vary principally with longitudinal specific force. The nozzles-up conventional configuration is used for level and climbing or accelerating flight at speeds above 90 knots. Below 90 knots and in descending or decelerating flight the nozzles are lowered for maximum control power and reach near-maximum values at the extreme decelerating boundary. The boundary of this plot encloses the acceptable flight envelope within which ν^* is defined. In some regions of this envelope, ν^* is given by the unconstrained maximum control margin but otherwise is at a boundary of the range of acceptable nozzle angles so that some constraint parameter is at an extreme permitted value. A subdivision of this acceptable flight envelope into such regions is shown in figure 21(b). The critical low-speed region is characterized by minimum lift margin, while the minimum flight path angle region is characterized by minimum pitch attitudes. At the edges of the acceptable flight envelope a second constraint parameter, usually the throttle, reaches an extreme and the acceptable range of nozzle angles narrows to a single value.

Fuel minimization is not considered in the present maximum control margin design of the nozzle schedule, but the fuel requirements of the schedule can be evaluated. Fuel requirements vary with nozzle setting since the required throttle setting and, therefore, fuel rate and noise, vary directly with nozzle angle (fig. 20). The acceptable nozzle settings for maximum control margin and for minimum throttle setting coincide in the two regions of constrained optimization corresponding to minimum nozzle and minimum lift margin, but not in the region of unconstrained optimization. Consequently, some fuel reduction is possible in this region by trading excess control margin for reduced throttle settings. Data for such a schedule were computed and the computations showed fuel reductions over a regime of higher speeds and descending flight ($V_E > 110$ knots, $A_u < 0$) with maximum reductions in throttle setting at steep descents ($\gamma \sim -5°$ to $-7°$). However, only the margins of this region are used by typical approaches so the nozzle schedule for the present tests was not modified to incorporate these improvements.

Nozzle Schedule

The optimized nozzle schedule is to be implemented in an airborne digital computer. Several methods are available, the choice being influenced by constraints on storage and computation time in the airborne computer and by the ease of adjusting the implemented schedule in different regions of the flight envelope to iteratively improve the fit, or as may be required following simulation or flight tests. The available methods for modeling such empirically determined functions include (1) programming the generating algorithm on-board and generating ν^* on-line, (2) storing the tabulated data

$$\left\{ v^*_{IJK} \right\} = \left\{ V^*\left(A_{u_i}, V_{E_j}, A_{N_k}\right); \ i = 1, \ldots, N_I, \ j = 1, \ldots, N_J, \ k = 1, \ldots, N_K \right\}$$

that would be generated off-line and use table interpolation on-board, and (3) fitting an approximating function, $\hat{v}^*(x)$, to the given tabulated data, $\{V^*_{IJK}\}$. Method (3) will be used here; method (1) cannot be used for lack of both storage and computation time in the airborne computer and method (2) requires large storage, in the amount $N_I \cdot N_J \cdot N_K$, but is easily adjusted. Method (3) requires the storage of relatively few parameters but the fitted function $\hat{v}^*(x)$ is difficult to generate or adjust.

The fitting function was selected and the parameters of the fit evaluated "by hand" using the procedure outlined next. The procedure is organized to fit the variation of v^* with its independent variables, $\{A_u, A_N, V_E\}$, one variable at a time and in the order of their importance in influencing the observed behavior of v^*; that is:

1. Select a functional form, $\hat{v}^*(\bar{c}, A_u)$, to fit the observed variation of v^* with A_u. Here, $\bar{c}$ refers to the parameters of the function. For example, a bounded straight line fit is

$$v^* = \min\left[\nu_{max}, \max[a + bA_u, v_{min}]\right]$$

2. Select V_{EJ}, A_{NK} from $\{V_{Ej}\}$, $\{A_{Nk}\}$ and calculate the parameters, $\bar{c}_{JK}$, which best fit the data $\{v^*_{IJK}, i = 1, \ldots, N_I\}$. Repeat this step for all velocities $\{V_{Ej}\}$ to obtain the set of parameters $\{\bar{c}_{jk}, j = 1, \ldots, N_J\}$.

3. Select a functional form, $\hat{\bar{c}}(\bar{d}_K, V_E)$, to fit the observed variation of $\bar{c}$ with V_E. Here, $\bar{d}_k$ refers to the parameters of the function.

4. Calculate the parameter values, $\bar{d}_k$, which best fit the data $\{\bar{c}_{jk}, j = 1, \ldots, N_J\}$. Repeat these computations, beginning with step 2, for all values of normal specific force, $\{A_{Nk}\}$ to obtain the set of parameters $\{\bar{d}_k, k = 1, \ldots, N_K\}$.

5. Select and fit an approximating function, $\hat{\bar{d}}(A_N)$, to these data.

This procedure results in a function of the form

$$\hat{v}^*(\bar{x}) = \hat{v}^*(A_u, \bar{c})$$

where

$$\bar{c} = \hat{\bar{c}}(\bar{d}, V_E)$$

$$\bar{d} = \hat{\bar{d}}(A_N)$$

The nonunique choices of fitting function and parameter values at each step of the above procedure allow useful latitude to impose engineering judgment. However, it has proved cumbersome, and a more algorithmic approach would be necessary if more than three independent variables were desired in the schedule. The functional forms selected at each step should be continuous,

and linear forms are preferred to, say, polynomials because they extend linearly beyond the domain for which the data are fitted. In addition, the selected form should be sufficiently elaborate to meet the accuracy objectives of the fitting process; that is, $\hat{\nu}*$ should remain within the range of acceptable nozzle angles over as much of the acceptable flight envelope of $\nu*$ as is possible; no interior region of this envelope should become unacceptable as a result of inaccuracies in the approximating function; and the fitting accuracy should be greatest near the boundaries of the acceptable flight envelope where the range of acceptable nozzle angles is smallest and control power is marginal.

In the present problem the behavior of $\nu*$ differs distinctly among the regions shown in figure 21(b) but is consistent within any region, so that a different function is expected to be required in order to model $\nu*$ accurately on each region. A suitable form was derived as

$$\hat{\nu}*(x) = \min\{104,\max\{\ell_0(x),\ell_1(x),q(x),6°\}\} \qquad (42)$$

where $q(x)$ models $\nu*$ in the region of unconstrained maximum control power and is quadratic in A_u, and ℓ_0, ℓ_1 are both linear in A_u and model $\nu*$ in the region of minimum lift margin. Two functions are required in this region in order to model the effects of piecewise linear variations in the underlying flap schedule. Otherwise, $\hat{\nu}*$ is bounded by the minimum and maximum nozzle angles. The fitting function is further defined in figure 22(a) together with a subdivision of the domain into regions on which $\hat{\nu}*$ is given by one or another of the functions in equation (42) and which can be compared with the subdivision shown in figure 21(b).

A contour plot of $\hat{\nu}*$ is shown in figure 22(b) and can be compared with the original function in figure 21(a).

The approximating function, $\hat{\nu}*(x)$, is defined everywhere in $\mathscr{X}$ both inside and outside the acceptable flight envelope $\mathscr{X}_{AF}$ of figure 21, even though no data outside that envelope are available since the optimum configuration is undefined for this region in the problem formulation given in the earlier section on configuration optimization. It should be noted that trim solutions exist in a limited region, $\mathscr{X}_F-\mathscr{X}_{AF}$, outside the acceptable flight envelope, even though all such solutions are operationally unacceptable for steady flight. For this discussion it is useful to define these flight envelopes as volumes in the space of path variables

$$\left.\begin{array}{l}\mathscr{X}_{AF}(\bar{p}) \equiv \{\bar{x};\quad \mathscr{U}_{TA}(\bar{p},\bar{x}) \neq \phi,\ \bar{x} \in \mathscr{X}_o\}\\[2mm]\mathscr{X}_F(\bar{p}) \equiv \{\bar{x};\quad \mathscr{U}_T(\bar{p},\bar{x}) \neq \phi,\ \bar{x} \in \mathscr{X}_o\}\end{array}\right\} \qquad (43)$$

The constraint abuse buffer region in which trim solutions exist but are unacceptable is then

$$\mathscr{X}_{BF}(\bar{p}) \equiv \mathscr{X}_F(\bar{p}) - \mathscr{X}_{AF}(\bar{p}) \qquad (44)$$

The boundaries of $\hat{\mathscr{X}}_{AF}$ and $\hat{\mathscr{X}}_F$ corresponding to $\hat{\nu}*$ and F* are shown in figure 22(c). It is seen that a buffer region is provided by this schedule. This buffer zone is subdivided in figure 22(c) according to the constraint parameters which are abused. Along the inner boundary minimum speed is limited by lift margin, throttle, and control margin; maximum A_u by pitch attitude, throttle, and control margin; and minimum A_u by control margin and pitch attitude. The outer boundary is reached generally at the engine limits.

In flight, the aircraft may be carried into this buffer region unexpectedly by wind disturbances (gusts, wind shears, and step vertical, or horizontal winds) which induce abuses of the minimum acceptable speed boundary, or more generally, flight envelope abuses. A sudden loss of trim solutions at this boundary would create a difficult monitoring problem for the pilot and some explicit criterion for defining the configuration schedule in the buffer region is desired. The optimization procedure given in the section on configuration optimization can be extended to the region where no acceptable trim solution occurs by relaxing the constraints listed in figure 15, in some specified order and amount, until a "least unacceptable" solution occurs satisfying the relaxed constraints. The inclusion of such criteria for the buffer region in the configuration optimization procedure incorporates the design goal that

$$\hat{\mathscr{X}}_F(p) \cong \mathscr{X}_F(p)$$

explicitly in the problem. In the present work, $\hat{\nu}*$ was not explicitly designed for this region, but an acceptable design occurs due to the ability of the piecewise linear fitting function used here to extend in a physically reasonable way beyond the domain of the data to be fitted.

The boundary of $\mathscr{X}_F$ has been included in figure 22(c) as a dashed line which can be compared with the boundary of $\hat{\mathscr{X}}_F$ achieved by the schedule. The two sets differ only along the minimum speed boundary where the schedule loses 4 knots or less in the descent regime and more in the climb region.

The locus of operating points in the $A_u - V_E$ plane for a representative AWJSRA STOL approach flight from cruise to glide slope and touchdown is included in figure 22(c). Very nearly the entire sequence of descending or decelerating segments is within the acceptable envelope $\hat{\mathscr{X}}_{AF}(p_s)$ of the designed configuration schedule, but approaches the minimum speed and A_u boundaries very closely with a negligible abuse of the minimum speed boundary during flare. A significant aspect of STOL approach operations, such as this one, is the full exploitation of the low speed and maximum deceleration regions of the flight envelope to achieve the steep approach and short landing field objectives.

Solutions for the nominal values of the remaining control variables and other configuration-dependent parameters of interest in the control problem can now be calculated over the complete flight envelope corresponding to the configuration schedule, $\hat{v}*$, $F*$. Contour plots of the nominal values of throttle, angle of attack, elevator, lift margin, and control power are given for the A_u - V_E plane at $A_N = 1$ (fig. 23) and for the A_u - A_N plane at 80 knots airspeed (fig. 24). In flight, values of these controls will be adjusted from their nominal values due to random corrective acceleration commands, nonstandard parameter values, and inaccuracies in the aircraft modeling data used to generate these plots.

Contour plots in the A_u - V_E plane give the variation of control settings for all static equilibrium and steady decelerating or accelerating operating points. The throttle setting (fig. 23(a)) shows the conventional trends in the region of level and ascending/accelerating flight where the conventional nozzles-up configuration occurs (cf. fig. 22(b)); that is, throttle increases principally with A_u and somewhat with V_E. In the region of descending/decelerating flight where nozzle variations occur the throttle is more nearly independent of both A_u and V_E out to the edge of the envelope. At speeds below 70 knots, where engine power is used to maintain lift margin, the throttle is seen to rise rapidly with decreasing speed and is nearly independent of A_u. Thus, three regions with different throttle behavior occur, corresponding to conventional and nonconventional configurations and to minimum lift margin.

As in CTOL aircraft, angle of attack principally controls lift coefficient and normal acceleration at all flight conditions and can therefore be expected to vary directly with A_N, inversely with V_E, and to be independent of A_u. These trends can be modified by the variation of flap since flap also controls lift coefficient, and by the variation of throttle when flaps are down since engine power then controls lift coefficient to a significant degree. Thus, details of the angle of attack variation seen in figure 23(b) are due in part to the selected flap schedule (fig. 17) and to the nozzle schedule at low speeds through its effect on the throttle setting. In a manual approach with CTOL aircraft the flap history is typically a step function versus speed with a corresponding sawtooth angle of attack function. For an automatic approach, a smooth flap schedule can be expected to give a nearly constant angle of attack. A similar trend occurs with powered-lift aircraft and is extended to speeds below that for which maximum flap is reached by raising throttle smoothly with speed reductions. Figure 23(b) shows that angle of attack varies very little with airspeed or A_u over nearly the entire flight regime; a "bowl" at 90 knots and a "peak" at 80 knots are related to corresponding variations in the scheduled flap with V_E and A_u, respectively, in these two regions.

A consequence of flap usage in CTOL aircraft is that the trim value of the regulator control variable α is maintained roughly centered in its allowed range; this relationship between scheduling of the configuration

control variables and regulator controls also appears in the present maximum control margin design. The nozzle schedule, in that region where the nozzle is not at an extreme, maintains the throttle roughly centered in its range, and the flap acts similarly on α.

The trim elevator setting (fig. 23(c)) does not saturate its acceptable range anywhere or impose a boundary on the flight envelope. There is little variation in trim elevator over the flight envelope.

Lift margin (fig. 23(d)) increases with speed and is very nearly independent of either A_u or flight-path angle. Along the approach path superposed on figure 23(d), this control parameter drops from 2 g at cruise to the minimum permitted value for powered lift, 0.4 g, which is reached on the glide slope. For the AWJSRA, the lift margin constraint limits the minimum approach speed. At higher speeds, excess lift margin can potentially be traded for reduced fuel rates by reducing the scheduled flap value. This is based on the increase in aerodynamic drag with increased flap setting at higher speeds. Fuel reductions are therefore possible in a region with lift margin above some comfortable value, say 1 g, ($V_E > 100$ knots) and scheduled flap settings above the minimum ($V_E < 157$ knots).

Control margin for the constant-nozzle regulator is shown in figure 23(c). Control margin reaches zero at the minimum and maximum throttle values allowed for regulation and is undefined outside that boundary. Good control margin (above 0.25 g) is maintained throughout most of the flight envelope. It drops below this in the low-speed descending flight regime and in narrow bands around the edges of the flight envelope. During the approach path superposed in figure 23(e), its value drops from above 0.5 g to 0.12 g at the glide slope operating point. Flight is extended into this marginal region with acceptable control margin (0.25 g) by using three controls for regulation; otherwise, acceptable approach operation with the fixed-nozzle regulator would be limited to shallow descents and higher approach speeds enclosed by a 0.25-g contour in figure 23(e). Nozzle scheduling to maximize control margin is of course more critical in the marginal regime.

The fixed nozzle mode has low control margin and high control sensitivity in the low-speed descending flight regime. This occurs because perturbation forces generated by variations in α and δ_t are both close to the normal axis when nozzles and flaps are down so that there is poor control margin in longitudinal acceleration. The fixed throttle mode has more nearly orthogonal perturbation forces associated with variations of α and ν at high nominal nozzle settings and is, therefore, of interest as an alternative central regulator mode in this flight regime. To evaluate the potential improvement in central regulator mode control margin, data for a throttle schedule which maximized the fixed throttle control margin (CM_{δ_f, δ_t}) was generated by the same method previously outlined for the optimum nozzle computation. The results showed that the fixed throttle mode had greater control margin over the critical STOL regime (roughly, $V_E < 100$ knots, $A_u < 0$); the improvement was only modest at the glide slope (0.03 g) due to limitations on nozzle travel, but exceeded 0.1 g in much of the regime.

Contour plots on the $A_u - A_N$ plane are given in figure 24 for an airspeed of 80 knots. These plots illustrate the variation of nozzle schedule and trim controls with A_N and on various constant speed maneuvers in which A_N differs from 1 g, such as steady turns and flight-path angle changes. The flap schedule (eq. (39)) is not included in these plots since it is independent of A_N.

Figure 24(a) shows some overview characteristics of the configuration schedule at this speed. The boundary of trim solutions is irregular and defined variously by engine thrust and aerodynamic lift limits. The boundary of acceptable flight conditions is defined in different segments by constraints on minimum lift margin and minimum or maximum throttle or pitch attitude. The intervening buffer zone is hatched to indicate the abused constraint parameters. Operating points for some flight conditions of interest are superposed on this figure; the loci of static equilibrium and steady turns for different flight-path angles is shown together with a scale of equivalent flight-path angles below the abscissa of the figure. A range of angles from $-10°$ to $8°$ is within the acceptable flight envelope at this speed. Flight-path angle is changed by transient pullup or pushover maneuvers requiring excursions in normal acceleration of 0.1 g to 0.2 g around static equilibrium; maneuvers of this type for the AWJSRA approach are shown in the figure and are within the acceptable flight envelope.

The nozzle schedule (fig. 24(b)) varies principally with A_u and the nozzle is therefore used to change flight-path angle. Lesser variation with A_N occurs so that there is some adjustment of nozzle angle to achieve steady turns. There is very little use of the conventional nozzles-up configuration at this low speed.

The corresponding throttle setting (fig. 24(c)) shows little variation except near the margins of the flight envelope; hence the throttle control is nearly fixed during the maneuvers discussed above and its conventional function in controlling A_u is taken over by the nozzles.

The corresponding trim angle of attack (fig. 24(d)) increases with A_N and, therefore, angle of attack is used to control A_N during maneuvers requiring transient or steady changes in A_N such as the pullup and pitchover maneuvers superposed on figure 24(d). This use of angle of attack is the conventional one. The trim elevator setting (fig. 24(e)) decreases with A_N except at positive values of A_u and remains well within the permitted range of elevator settings.

To summarize figure 24, over the maneuver range of interest, the nozzles are used to control A_u and angle of attack to control A_N, while the throttles are nearly constant. This can be compared with conventional configurations in which nozzles are up and throttle controls A_u. More generally, the control usage seen here occurs at all lower speeds and at higher speeds in the region of the $A_u - A_N$ plane in which nonconventional nozzle positions are scheduled. The region of conventional configuration and throttle usage is nearly null at 80 knots but expands at higher speeds.

SIMULATION TESTS

Simulation tests have been carried out in a simplified simulation of the system shown in figure 1 (cf. ref. 9). The simulation accurately represents the translational degrees of freedom of the aircraft and is suited to testing the operation of the trajectory control subsystem in response to low frequency inputs such as trajectory commands, Trimmap model errors, and steady winds. In this simulation, the combined attitude control subsystem and aircraft attitude dynamics are replaced with approximate second-order dynamics for attitude response to attitude commands. The estimation subsystem is omitted and perfect state estimation is assumed except for a filter to simulate the estimation of steady winds. The command generator and path regulator elements of the control system are included in the simulation; details of their design are outside the scope of this paper but descriptions are given in references 1 and 2.

A flow chart of the complete Force Trimmap of the simulated automatic control system is shown in figure 25 with relevant equations from the text and appendix D noted in each element. The inputs are the reference trajectory commands (ac_r, VC_r) from the command generator, the corrective feedback acceleration Δa_r from the path regulator, the wind estimate $\hat{w}_r$, and the sideslip command β_c. Additional inputs used are the current flap setting (δ_f) and parameter values (W, τ, δ, ρ). The vector inputs are assumed referenced to runway axes; the acceleration commands are converted to stability axis components of the applied specific force ($A_{u_{NOM}}$, $A_{N_{NOM}}$, A_{u_c}, A_{N_c}) using equations (4), (7), (D4), (D18), and (D19), and these are used by the configuration schedule and trim solution algorithm of the basic Trimmap to determine $\{\delta_{f_c}, \delta_{t_c}, \nu_c, \alpha_c\}$. Finally, the elevator trim setting δ_{e_T} is computed from the trim solution (appendix A), and the Euler attitude and angular rate commands to the attitude control subsystem $\{\phi_c, \theta_c, \psi_c, \omega c_b\}$ are computed from various inputs (act_p, γ_{ac}, $\psi_{V_{ac}}$, Φ_{V_c}, β_c, α_c) using equations derived in appendix D. These inputs are derived in turn from the Trimmap input variables as noted in figure 25.

The approach test path used for the simulation results of this section is shown in figure 26 along with the input parameters to the control system's command generator which define the trajectory. This trajectory is a simulation test path and not one proposed for actual flight. It consists of a sequence of legs that correspond to a succession of steady or slowly changing operating points. The command generator is required to fill in reasonable maneuvers to pass from one steady operating point to the next at the leg junctions. Some relatively complex maneuvers involving all three path axes simultaneously are included in the test path. Since nonzero model errors are present in the Trimmap due to aerodynamic or engine model error, programming errors, or errors in estimates of airspeed or parameter values, a test is included during leg 3 to demonstrate their effects on system performance by off-setting the simulated aircraft lift and drag forces by 0.06 g. Finally, steady winds are normally present in terminal area operations and wind tests during a level turn (legs 4 and 5), a low speed helix (leg 7), and on the glide slope (leg 8)

are included to demonstrate the ability of the system to track the four-dimensional inertial reference path in the presence of winds and wind shears.

Simulation results are shown in figures 27(a)-(c), in which the principal variables are grouped into acceleration and speed commands (Trimmap inputs), control commands (Trimmap outputs), and trajectory errors (tracking performance).

Response to Maneuver Commands

The initial period up to 55 sec of flight illustrates the maneuvering capabilities of the system. Transient acceleration commands to acquire leg 2 (a 2-axis maneuver to enter a descending turn from leg 1) and leg 3 (a 3-axis maneuver to enter a level decelerating straight segment from leg 2) are supplied by the command generator; the longitudinal acceleration command drops without overshoot at the pitchover and then rises without overshoot at the pullup to level flight but with some small reversal as the deceleration of leg 3 is initiated. The normal acceleration command drops transiently for the pitchover and then rises without overshoot to its steady-state value for the turn; the converse transient occurs at the exit from leg 2.

The applied specific force time histories in figure 27(a) include traces for the total command, which includes the feedback term, and the actual aircraft applied specific force. Since no external disturbances are present during this period, transient differences from the nominal specific force commands measure the ability of the system to follow maneuver commands. It is desired that these response errors be minimized in order that the regulator work chiefly on the effects of external disturbances to the system. The response errors depend on both the commanded maneuver defined by the command generator and on the acceleration tracking accuracy of the Trimmap-aircraft combination. In general, nonzero maneuver command rates (principally jerk) require nonzero control rates and these result in trajectory errors and feedback activity due to control lags; that is, control rates and tracking errors increase with the commanded maneuver activity. Thus, design goals for the command generator include minimizing the maneuvering required to transition between any steady flight conditions specified by the coarse input trajectory commands to the system, and to limit maneuvering commands in accordance with the acceleration tracking capability of the Trimmap-aircraft combination.

The activity of the scheduled controls for the first 55 sec shows only minor nozzle use which is closely related to the change in normal-specific force for the turn, while the regulator controls show throttle variations which follow the change in longitudinal specific force with flight-path angle. Only minor angle of attack variations are used so that pitch attitude simply follows flight-path angle. The roll command is seen to vary smoothly without overshoot at turn entry and exit; this behavior reflects the success of the command generator design for the lateral axis.

These maneuvers occur in the CTOL flight regime and begin and end with the AWJSRA in its conventional configuration; the control activity seen here

36

differs from conventional control in that nozzle activity replaces angle of attack for the turn execution. If operationally desirable, CTOL-like maneuver control activity can be imposed on the Trimmap by requiring the use of minimum nozzle setting as much as possible in the configuration schedule.

The control activity used by the Trimmap to execute the commanded transition maneuvers in figure 27(b) shows desired characteristics; that is, no unnecessary overshoot or reversal. More generally, control activity, as measured by control rates required for maneuvering flight, is given by

$$\dot{\bar{u}}_c = \frac{\partial \bar{u}*}{\partial V_E} \dot{V}_E + \frac{\partial \bar{u}*}{\partial A_u} \dot{A}_u + \frac{\partial \bar{u}*}{\partial A_N} \dot{A}_N = [\nabla_x \bar{u}*(\bar{x},\bar{p})]\dot{\bar{x}}_c \qquad (45)$$

where

$$\bar{u} = (\delta_f, \nu, \alpha, \delta_t)^T$$

This expression contains the gradients of the configuration schedule and associated trim solutions of the Trimmap, $\bar{u}*$, and the maneuver command rates of the command generator, $\dot{\bar{x}}$. Thus, control activity and its minimization for the automatic control system depends on both of these elements.

The control activity seen in figure 27(b) involves simultaneous use of roll, angle of attack (or elevator), throttle, and nozzle controls during maneuvers requiring accelerations along the three path axes simultaneously; that is, the Trimmap automatically coordinates all of the AWJSRA's controls with the commanded maneuver for any maneuver in the output set of the command generator. In contrast, manual flight operations are designed to minimize pilot workload, and a significant problem for STOL aircraft is to limit workload requirements within the capabilities inherent in manual flight control; this generally implies control usage limited to two controls at a time with sequential step changes of the redundant configuration controls, and maneuvering carried out sequentially along one axis at a time (refs. 6, 7, and 8). For the present automatic system, these operational restrictions were not imposed because the workload capacity of the digital flight-control system, as measured by the number of input and output channels, data memory capacity, and real-time processing speed, exceed those inherent in direct manual flight control, but the objective remains to minimize control activity. Restrictions on the operational use of this general capability of the automatic control system for ease of monitoring requirements and pilot takeover were not considered in this study. Restrictions on maneuver complexity are readily imposed as restrictions on the coarse input trajectory commands.

Effects of Steady Model Errors

The actual acceleration can differ from the commanded acceleration both transiently and in steady state due to errors in the model of aircraft forces used by the Trimmap to compute control settings. These errors can arise from several sources (aerodynamic and engine force model errors, state and parameter estimation errors, programming errors, neglected dynamic effects) and are

normally present during flight. To illustrate the effects of steady model errors, the normal and longitudinal applied specific forces of the aircraft were offset by 0.06 g during the time interval [55, 80]. These errors are compensated by feedback as follows: in steady state, position standoff errors occur (fig. 27(c)) of sufficient size to generate a steady feedback acceleration command, Δa, which exactly compensates the model error. This effect is seen in figure 27(a), where the total specific force commands (A_{u_c}, A_{N_c}), rise to steady values different from the nominal specific force commands, but the actual specific force (A_u, A_N) is held at the desired nominal value. The required steady corrective acceleration command is generated by steady offsets of the regulator controls, (α, δ_t) from their expected value as given by the configuration schedule and available model data. This is seen in figure 27(b) where throttle is driven nearly to its acceptable limit to compensate for the longitudinal error which, in size, is a large percentage of the engine's acceleration capacity. The angle of attack compensates for the normal acceleration error but in this case only a very small offset occurs because the model error is a small percentage of the wing's lift force capacity.

In general, if ε_a is the Trimmap model error expressed as an acceleration error vector,

$$\varepsilon_a \equiv (\tilde{A}_u, \tilde{A}_N)^T$$

then a steady position standoff error proportional to the acceleration error develops asymptotically

$$\Delta R \xrightarrow{\ t\ } [K_R^{-1}] \varepsilon_a \tag{46}$$

where $[K_R]$ is the position error feedback gain in the path error regulator. This induces a steady corrective acceleration that exactly compensates the model error

$$\Delta a \xrightarrow{\ t\ } -\varepsilon_a \tag{47}$$

but requires a steady offset of the regulator controls from their values predicted by the design data

$$\Delta \bar{u}_c \xrightarrow{\ t\ } -[\nabla_a \bar{u}_R^*(x,p)] \varepsilon_a \tag{48}$$

Here $[\nabla_a \bar{u}_R^*]$ is the Jacobian of the regulator controls with respect to acceleration. The derivation of these results is omitted and rests partly on details of the path error regulator element in figure 1. The basic dependence of path tracking performance on the modeling accuracy of the trim solution algorithm and the related trade-off between performance and model accuracy are evident in equation (46). Steady feedback signals measure the modeling error (eq. (47)), and an analysis of this signal from flight records would indicate the size and nature of such errors. In addition, these errors would saturate the authority limits of the feedback if sufficiently large. The system compensates for model errors by adjusting the regulator controls (eq. (48)) and may thereby result in reduced control and lift margins.

The path tracking errors and steady feedback offsets noted in equations (46) and (47) can be removed or reduced by adding integral feedback of the acceleration error to the Trimmap of figure 25; this can be implemented as an additional corrective acceleration, δa, in the total acceleration command

$$act_p = ac_p + \Delta a_p + \delta a_p \tag{49a}$$

where, for each path axis, the correction has the form

$$\delta a = max\left\{-\delta a_L, min\left\{K \int_o^t (ac - \hat{a})dt, \delta a_L\right\}\right\} \tag{49b}$$

Here, δa_L is the authority limit of the integral feedback, $\hat{a}$ is the estimated acceleration, and K the feedback gain. This model error compensation device adjusts controls in accordance with equation (48), but accommodates model errors $|\varepsilon_a|$ up to the amount δa_L without steady-state position error or feedback offset. Equations (46) and (47) then define the effects of steady Trimmap inaccuracies in excess of δa_L. A compensator of the type (eqs. 49)) is not included in the present simulation study but will be included in a further study of the system.

Accuracy requirements for the Trimmap model are of interest because of the relation between model accuracy and Trimmap computational requirements. The Trimmap model is derived from an estimate of the aircraft and contains errors due to approximations in representing the estimated aircraft and the uncertainties of the estimated model. With the use of integral feedback, (eqs. 49)), approximation errors up to a fraction of δa_L can be permitted while the remaining compensator authority is applied to the basic uncertainties in estimating the actual aircraft.

<center>Response to Winds</center>

A steady x-axis wind of 15 knots is imposed during a 180° turn in the time interval [100, 155] and, with respect to the aircraft, acts variously as a tailwind, crosswind, and headwind during the turn. The control system is expected to track a circular path, as seen from the ground, and maintain the desired ground speed.

The appearance of steady wind in the Trimmap calculations is seen in figure 25; the velocity vector with respect to the air mass is used to define the path axes in which the components of the nominal and total acceleration commands are given, and to define the equivalent airspeed used in the configuration schedule and trim solution algorithm. In the simulation results in figure 27(a), $A_{u_{NOM}}$ rises and falls during the turn due to a geometric effect; the required air velocity vector V_{A_c} is not perpendicular to the radius vector of the inertial circle to be tracked and some acceleration along $\bar{V}_{A_c}$ is required to supply the centripetal turn acceleration. These effects of winds on the inputs to the basic Trimmap can be derived; the velocities of interest are related by

$$\bar{V}_A = \bar{V}_I - \hat{\bar{W}} \tag{50}$$

The effect of the estimated wind on the spherical coordinates of V_A is then

$$\left.\begin{aligned}
\Delta V_A &= -\underline{u} \cdot \hat{\bar{W}} \\[2mm]
\Delta \psi_V &= -\underline{u} \otimes \frac{\hat{\bar{W}}}{V_I} \cdot \bar{k} \\[2mm]
\Delta \gamma &= \gamma_I \underline{u} \cdot \frac{\hat{\bar{W}}}{V_I}
\end{aligned}\right\} \tag{51}$$

Here, relatively small winds are assumed

$$\frac{|\hat{\bar{W}}|}{V_I} << 1$$

and the effect of steady vertical wind, $\hat{W}_z$, on flight-path angle is neglected since $\hat{W}_z$ is normally negligible. During the turn, $\bar{V}_A$ is time-varying as $\bar{V}_I$ changes direction. Otherwise, $\bar{V}_A$ is constant when $\bar{V}_I$ and $\bar{W}$ are constant vectors. The corresponding variations in Trimmap inputs are derived from equations (6) and (51) as

$$\left.\begin{aligned}
\Delta \bar{x} &\equiv (\Delta V_E, \Delta A_u, \Delta A_N)^T \\[2mm]
\Delta V_E &\cong \Delta V_A \sqrt{\rho/\rho_o} \\[2mm]
\Delta A_u &= \bar{a} \cdot \Delta \underline{u} \cong \bar{a} \cdot \bar{m}\Delta\psi_V + \Delta\gamma \\[2mm]
\Delta A_N &= \cos \phi_V \bar{a} \cdot \Delta\bar{n} + \sin \phi_V \bar{a} \cdot \Delta\bar{m} \cong 0
\end{aligned}\right\} \tag{52}$$

As seen in equations (52) the centripetal turn acceleration $\bar{a} \cdot \bar{m}$, which is of the order of 0.4 g typically, will affect the commanded acceleration along the aircraft stability axis $\bar{u}_A$ proportionally to $\Delta\psi_V(t)$. The effect on normal acceleration command is generally negligible compared to 1 g, by several orders of magnitude.

Because the inputs to the configuration schedule x_{NOM} are adjusted for winds, the configuration controls will generally be adjusted automatically to maintain the designed maximum control margin configuration in the presence of steady winds. This is illustrated in figure 27(b), where the flap command varies in relation to the equivalent airspeed command V_{E_c}, although there is no adjustment of nozzle from its minimum value at this example flight condition. The regulator controls also vary in response to the effects of winds on $\bar{x}_c$, as seen in the throttle variation which follows the time history of A_{u_c}. In the present example, note that there is little effect on angle of attack since the effect of speed variations on lift is taken up principally by the scheduled flap adjustments. The general effects of steady winds on

40

adjustments of the controls from their anticipated no-wind values can be derived from the configuration schedule and associated trim solutions (figs. 17, 22(b), and 23) and can be represented as

$$\Delta \bar{u} = [\nabla_x \bar{u}*(\bar{x},\bar{p})]\Delta \bar{x} \tag{53}$$

where $\Delta \bar{x}$ is given by equations (52) and $[\nabla_x \bar{u}*]$ is the Jacobian of the basic Trimmap function or algorithm. At flight conditions other than the test case of figure 27, the nozzle may be adjusted in place of throttle (when $\nu*$ is not at a nozzle limit) and, similarly, α may be adjusted in place of flap (when $F*$ is at a flap limit); in all cases, however, the Trimmap maintains the optimum configuration automatically.

The trajectory tracking performance illustrated in figure 27(c) shows good tracking of the commanded velocity vector of the trajectory (V_{I_c}, ψ_{V_c}, γ_c) during the wind test with only minor transient errors due to transient maneuvering at turn entry and exit and due to wind estimation lags at wind onset and offset.

Pitchover and Configuration Transition

During the period, $t \in [160, 194]$, the aircraft exits a decelerating turn (leg 5) onto a steep descent (leg 6). The longitudinal acceleration command (fig. 27(a)) reaches its descent value without overshoot while the normal acceleration transient for the pitchover uses the maximum excursion, 0.125 g, permitted for flight-path angle changes in the command generator.

Large changes in the configuration controls occur during the pitchover (fig. 27(b)); flap rises to 55° and nozzle to over 80°. The scheduled flap variation for this maneuver is due to the speed reduction and is independent of the flight-path angle change (fig. 17) while the nozzle change is due principally to the flight-path angle change (fig. 22(b)). The regulator controls, α, δ_t, are used transiently for the pitchover and are adjusted somewhat for the descent but remain roughly in the center of their ranges. Good maneuvering commands and execution is evidenced in the roll angle and in the velocity coordinates and path errors of figure 27(c)).

The aircraft begins the STOL phase of its approach at the pitchover, characterized by low speeds and steep descents near the minimum A_u boundary of the acceptable flight envelope and by the powered-lift, nozzle-down configuration. Control characteristics such as control margin (fig. 23(e)) and sensitivity also change rapidly for the worse with the configuration and speed changes and will remain marginal until landing.

This interval of the test path can be compared with the corresponding transition maneuver for manual approach described in reference 6, in which flap is first reduced stepwise with speed in level flight and then a step change in nozzle to its approach setting occurs simultaneously with pitchover to the descent path. In the present automatic approach, a short transition period again occurs, separating longer conventional and STOL phases of the

approach, and the flap and nozzle variations show the same relationship to
speed and equivalent flight-path angle. However, the automatic transition
shown here does not attempt to minimize pilot workload, so the sequential and
descrete steps of the manual transition are now carried out simultaneously
and continuously. The automatic system attempts to minimize control activity;
that is, overshoot of steady-state value or unnecessary reversal is avoided in
the path and control variables (A_u, A_N, V, γ, ψ, $\bar{R}$, θ, ϕ, δ_f, ν, α, δ_t).

<center>Descending Helical Turn with Winds</center>

Leg 7 ($t \in [194, 294]$) is a low-speed, steeply descending and decelerating
turn in the presence of a steady 10-knot y-axis wind whose onset occurs at
the quarter turn ($t = 205$). The maneuver execution is similar to earlier
results except for wind effects. The 10-knot wind is a crosswind relative
to the runway center plane and to approach paths confined to the centerplane,
and is not difficult to control as a crosswind relative to the aircraft.
However, during the 360° helical turn it acts variously as headwind, crosswind,
and tailwind and produces an excursion of the equivalent airspeed V_E down
to 58 knots in that quadrant of the helix in which it is a tailwind
(fig. 27(a)). This excursion abuses the minimum speed boundary by 6 knots and
results in abuse of the lift margin and maximum throttle constraints. In
addition, the longitudinal acceleration A_{uNOM} is affected by the wind
through both the turn acceleration and flight-path angle terms in equa-
tions (51) and (52) with excursions of A_u down to −0.18 g. This excursion
abuses the minimum A_u boundary of the acceptable flight envelope during
about half the turn and results in very low control margin. These envelope
abuses are also shown in figure 28. The minimum approach speed, $V_{E_{min}}(\bar{p})$,
is a familiar flight safety parameter for CTOL aircraft; in addition, STOL
aircraft can approach at steep glide angles near the minimum longitudinal
applied specific force boundary so that $A_{u_{min}}(\bar{p})$ is also a significant safety
parameter.

The control activity (fig. 27(b)) shows that the effects of wind on lift
are balanced at first by flap adjustments until it saturates at its maximum;
then by α increases, and finally, at the lowest speeds, large throttle
increases are used to supply powered lift and a modest abuse of the maximum
allowed steady throttle (25.6°) occurs. The nozzle variation is related to
the effect of wind on A_{uNOM}, and rises to values above 90° where there is
little speed control margin remaining in the regulator. The ability of the
Trimmap and autopilot to survive envelope abuse events and to continue solving
the trim equations outside the boundary of the acceptable flight envelope has
been demonstrated here. This capability is an important flight-safety aspect
of the design and, although the configuration schedule design procedure
formulated in the section on configuration optimization does not supply design
criteria for the envelope abuse regime, such criteria can be incorporated in
a general design methodology for redundantly controlled aircraft.

In the present simulation tests, the system is carried outside its
acceptable envelope while attempting to track the commanded four-dimensional
inertial path in the presence of winds. In an operational environment, a

four-dimensional guidance system would be additional element of the automatic control system not present in the system of figure 1 which would synthesize trajectory commands using wind information so that the aircraft is not forced to abuse its acceptable operational envelope in order to track the inertial trajectory (e.g., refs. 11 and 12). A helical path in the wind environment of the present simulation test can be flown at a shallower descent angle and higher speed without abusing the flight envelope, although the susceptibility of four-dimensional helical turns to wind effects on control activity and control characteristics makes it a doubtful operational maneuver.

Glide Slope with Wind Shear

The glide slope, ($t \in [294, 381]$), is a steep descent at minimum speed, which is disturbed in this test by both a crosswind (10 knots) and a headwind (15 knots). The headwind is initiated at $t = 315$ and then both winds decline linearly to zero at $t = 360$, prior to flare. This shear is modest relative to values encountered in practice but suffices to illustrate the effects of steady shear.

The crosswind requires only a change of aircraft heading ψ from the desired inertial direction ψ_{V_I}, and this correction is supplied automatically by the Trimmap, as seen by the small difference between ψ_V and ψ in figure 27(c).

The headwind produces variations of the nominal commands; both V_{E_C} and $A_{u_{NOM}}$ increase temporarily in accordance with equation (52) and the wind time history and also transient feedback components occur in A_{u_c} and A_{N_c} at the onset of the headwind (fig. 27(a)). The feedback components arise both from lags in the control response to the wind variation, and from errors in estimating the wind. Wind estimation errors enter the Trimmap calculations of lift and drag forces as airspeed errors and, hence, produce the same effect as other modeling errors (eqs. (46)-(49)); that is, if δV is the steady airspeed estimation error then the corresponding steady acceleration error is

$$\varepsilon_a = 2 \frac{\delta V}{V_A} \frac{QS_w}{m} \begin{pmatrix} C_D \\ C_L \end{pmatrix} \tag{54}$$

In the glide slope test, steady wind estimation errors result from wind shear, and the consequent steady position offsets below the reference glidepath, δR_u, δR_n, are seen in figure 27(c). Larger steady shear values would produce proportionately larger estimation errors, δV, and corresponding position offsets.

The control activity on the glide slope (fig. 27(b)) shows some nozzle adjustment in response to the wind effect on A_u. In manual operations (ref. 6) the nozzle is adjusted on the glide slope for winds; here, the automatic configuration schedule carries out a similar adjustment and can vary the adjustments with wind changes due to shear. The configuration schedule also attempts to reduce flap as airspeed increases, but is prevented

from doing so by a flap retraction stop installed in the aircraft (and simulated here) that prevents flap retraction by the automatic control system below a detent, once that detent is passed during an approach. The detents occur at flap settings 30°, 50°, and 65°. The retraction-stop event has the same effect on the trim solution calculation as a flap rate saturation event; that is, δ_{f_c} and δ_f are unequal and can remain unequal persistently in the case of steady winds. The calculation of the regulator controls, (α, δ_t), should therefore be based on the actual flap in order to generate the commanded acceleration accurately, as is done in the present Trimmap design.

Both regulator controls show variations on the glide slope (fig. 27(b)) due to winds; a complex throttle transient occurs at wind onset which in part executes the feedback transient in A_{N_c} at wind onset and, in part, the nominal A_u variation (see fig. 27(a)). In the STOL configuration, engine power is used to generate both normal and longitudinal acceleration and, hence, even if each input signal is a well-behaved transient, their combined effect on the throttle command can be twice as complex and require a higher frequency, as seen here. The angle of attack variation follows the airspeed change and also is used by the regulator function of the Trimmap to supply the corrective feedback portion of A_{u_c}; the combined effect is a rapid drop in α and pitch attitude by 5° at wind onset.

Several overview figures of the Trimmap inputs and outputs on the test path are shown in figures 28(a) and (b). The trajectory variables $\{V_E(t), A_u(t), t \in [0, 384]\}$ are seen in figure 28(a), and a dashed trace of the trajectory in the absence of winds is included for comparison. It is apparent that the winds during the level turn, helical descent, and glide slope legs can have a pronounced effect on these Trimmap and configuration schedule inputs while tracking a four-dimensional approach path. The low-speed steep helical descent is especially susceptible to envelope abuse due to winds both in minimum speed and minimum equivalent flight-path angle.

The locus of configuration commands (fig. 28(b)) during the approach is relatively simple and migrates from the lower left corner of the figure (CTOL configuration) to the upper right (STOL configuration). Of the remaining corners, the upper left does not occur in the configuration schedule and the lower right corresponds to nominal flight conditions which are little used in passenger operations. However, these regions would come into greater use if the nozzle were used for regulation.

It should be noted that, although some feedback activity and exercise of the regulation function occurs in the simulation results presented in this paper, these tests primarily demonstrate the functioning of the automatic configuration schedule and autopilot system in response to low-frequency inputs that excite only a minimum of feedback activity. Realistic examination of the regulator behavior and response to higher frequency maneuvers and feedback commands and to higher frequency disturbances and modeling errors requires a more accurate six degrees-of-freedom simulation of the aircraft attitude and engine dynamics than was used here; such an examination will be the subject of future simulation tests.

44

CONCLUSIONS

The design criteria for a Trimmap for the application of an advanced automatic control system structure (ref. 1 and fig. 1) to the augmentor wing jet STOL research aircraft (AWJSRA) has been described. This structure accommodates the coupling of redundantly controlled aircraft to an ATC system having a general set of approach trajectories at its command. The Trimmap is the central element of an acceleration controller structure capable of executing trajectory commands. Acceleration commands are constructed as the sum of the acceleration on the commanded trajectory and a feedback term to correct path errors; the Trimmap then calculates the control settings required to generate these accelerations at the current state and parameter values, using a model of the aircraft forces. The principal problems to be resolved in the Trimmap for this and other STOL aircraft are control redundancy and the nonlinearity of the trim equations.

A structure for resolving redundancy was proposed (fig. 10). It contains two principal elements: first, a configuration schedule drives the redundant controls (flap and nozzle) as a function of the nominal trajectory command and is configured off-line. The second element is a trim solution algorithm that carries out the regulation function by solving the two trim equations for the remaining controls (angle of attack and throttle) on the basis of the total acceleration command. It was found that the control margin available for regulation is maximized by using as many of the controls for this purpose as have sufficient bandwidth. The trim solution algorithm was therefore structured to default to nozzle use when either of the conventional controls saturate (fig. 14).

The configuration can be selected optimally at any flight condition within a range limited by the operational constraints. For the AWJSRA, the flap and nozzle were selected to maximize lift margin and regulator control margin. This was done because these margins are strongly dependent on the configuration controls and in order that the automatic system retain the aircraft's full capabilities for low-speed, steeply descending flight. It can be concluded that configuration management is a key design issue for redundantly controlled aircraft and governs the operational envelope of the automatic control system as well as the behavior of configuration-dependent parameters over that envelope.

Aircraft nonlinearity is treated in a simple way by the computational methods described here for solution of the trim equations (appendix B) and for optimization of the configuration schedule (appendix C). Tabulated data is used so that the relevant nonlinearities are approximated as continuous piecewise linear functions with accuracy governed by the number of pieces used. In addition, the design domains for all independent variables in the problem are bounded and known in each design problem. Thus, solutions of the nonlinear trim equations can be computed routinely and reliably by representing the model as piecewise linear, using a finite number of pieces, and then searching the pieces exhaustively for solutions. This approach, however, requires specially devised algorithms for each application and more general algorithms based on Newtonian iteration are attractive alternatives but of unknown convergence.

45

Similarly, the configuration optimization procedure is simply one of enumerating trim solutions and constraint parameters on a set of points which span the design domains of all variables defining configuration and flight condition, and selecting the optimum configuration at each flight condition from the solutions obtained.

The automatic control system, including the Trimmap described in this report, was subjected to simulation tests using a four-dimensional (4-D) STOL approach path (fig. 26).

These investigations demonstrate the system response to low-frequency inputs, including maneuver commands, Trimmap model errors, and steady winds, but system behavior in response to higher frequency disturbances, such as gusts and transient model errors, are not covered in these tests. Simulation results are shown in figure 27 from which a number of conclusions were drawn.

1. The proposed Trimmap structure provides automatic coordination of all aircraft controls during transition maneuvering and does so for any maneuver in a general output set permitted to the command generator and the underlying ATC system. Control rates and system performance during transitions depend on both the Trimmap configuration schedule and the command generator. The automatic system has a higher workload capacity than is acceptable in manually controlled flight, and the present concepts exploit this higher capacity to achieve the generalized maneuver capability.

2. Steady Trimmap errors in modeling the aircraft forces are continuously present in flight and can arise from aircraft model data inaccuracies, state or parameter estimation errors, and software inaccuracies. The system feedback adjusts the regulator controls from their nominal values in order to compensate for such errors, and results in a steady position error in proportion to the accuracy of the model used by the trim solution algorithm (eqs. (46)-(49)). It was concluded that integral feedback of the acceleration error (eq. 49)) should be added to the Trimmap in order to relieve the regulator of using its authority for steady model error compensation and to reduce the sensitivity of system tracking performance to model accuracy.

3. Steady winds are normally present throughout the approach and can significantly affect the Trimmap inputs compared to their values in the absence of winds (eqs. (51) and (52) and fig. 28(a)). The Trimmap adjusts all controls for the wind effects to maintain the maximum control margin configuration automatically while tracking the four-dimensional inertial path. Steady wind estimation errors arise during wind shear conditions and produce the model error effects described above.

4. The STOL approach path operates near the boundaries of the acceptable flight regime both in minimum speed and in minimum longitudinal applied specific force in order to achieve the short field length capability. The minimum flight-path angle boundary corresponding to $A_{u_{min}}(\bar{p})$ is, therefore,

a significant safety parameter for STOL aircraft in addition to the minimum speed, $V_{E_{min}}(\bar{p})$. Abuses of both boundaries can arise due to winds, and the capability of the Trimmap to operate during such abuses was demonstrated.

Ames Research Center
  National Aeronautics and Space Administration
    Moffett Field, Calif. 94035, April 12, 1978

47

APPENDIX A

AWJSRA ENGINE AND AERODYNAMIC FORCE MODELS AND ELEVATOR TRIM FUNCTION

The engine and aerodynamic force models used in the calculations of this paper are described in detail. Both graphs and tabulated data are given for the various functions required for the models (T_H, T_C, $\dot{m}_E$, C_D, C_L). In addition, elevator trim values and engine fuel flow data used in the Force Trimmap are included.

Function evaluation is carried out by interpolation of the tabulated data using simple, invertible interpolation formulas given in appendix B. To minimize storage and computation time requirements, table sizes have been approximately minimized within the accuracy requirement that the original data, based on theory, wind-tunnel tests, and flight tests, be reproduced by the force model to an accuracy of 0.01 g. Other classes of data-fitting functions (spline functions and orthogonal polynomials) were investigated for computational efficiency; however, they were difficult to invert and required as many parameters as the tabulated data method in order to obtain the required accuracy. In addition, tabulated models permit straightforward control over the maximum error in the model while analytical function models, whose parameters are computed via least squares techniques, are designed to minimize average errors. The table interpolation method is applied consistently throughout this paper and was found to be simple and routinely applicable in all phases of the work.

Engine Model

The AWJSRA is powered by two twin-spool jet engines (Rolls Royce Spey MK 801-SF engines). Some air is ducted off the first compressor and exhausted through the augmentor flaps to obtain lift augmentation; the air is also ducted to the ailerons for boundary-layer control. The remaining air passes through the engine normally but is exhausted through movable nozzles to provide a jet thrust vector which can be varied in direction over 90°. The engine nozzles and forces are illustrated in figure 29.

The direct engine forces are the thrust from the hot exhaust and the ram drag due to momentum rate of the inlet air. These forces, referred to stability axes, are

$$\bar{F}_E = T_H \begin{pmatrix} \cos(\nu + \alpha) \\ \sin(\nu + \alpha) \end{pmatrix} + \dot{m}_E V_A \begin{pmatrix} -1 \\ 0 \end{pmatrix} \tag{A1}$$

In addition, the effect of the ducted air used for lift augmentation is included in the aerodynamic description through the dependence of lift and drag coefficients on the "cold thrust coefficient"

48

$$C_J \equiv \frac{T_c}{QS_W} \tag{A2}$$

where T_c is the equivalent thrust obtained from isentropic expansion of the compressed ducted air to ambient atmospheric conditions.

Three parameters (T_H, T_c, $\dot{m}_E$) in equations (A1) and (A2) remain to be defined. These are functions of airspeed, atmospheric pressure and temperature, and engine rpm. Plots and tables are given in figure 30 and in table 1 for the "corrected" engine parameters

$$\frac{T_H(N_H/\sqrt{\tau},V)}{\delta} \quad , \quad \frac{T_c(N_H/\sqrt{\tau},V)}{\delta} \quad , \quad \frac{\sqrt{\tau}\ \dot{m}_E(N_H/\sqrt{\tau})}{\delta}$$

where

τ,δ = temperature and pressure ratios, $\dfrac{T_1}{T_{SSL}}$, $\dfrac{P_1}{P_{SSL}}$

P_{SSL},T_{SSL} = standard mid-latitude sea level atmospheric pressure, temperature (10.13 N/cm^2, 288.15° K)

P_1,T_1 = engine inlet stagnation conditions

These data derived from engine test stand data from the manufacturer and from company reports from the aircraft modification contractor, include the effects of power bleed and ducting losses. The ratios τ, δ are convenient similarity parameters introduced so that engine thrust and mass flow at all atmospheric conditions can be calculated from those at the reference conditions, $\tau = \delta = 1$. The independent variable, N_H, is the cockpit tachometer dial reading ("power setting") which, for this installation, is rpm/121.3. Engine operational limits on power setting are

$$\left.\begin{array}{lll}
\text{Idle power} & N_I = & 59.3 \\[2mm]
\text{Maximum continuous power} & N_{MC} = & 95.8 \\[2mm]
\text{Normal T.O. power} & N_{TO} = & 98.5 \\[2mm]
\text{Emergency power} & N_E = & 101.4
\end{array}\right\} \tag{A3}$$

Such limits occur for most jet engine installations; they are selected to yield specified time intervals between required major engine overhauls and are marked by detents on the throttle controls.

The throttle lever angle, which is used to control engine output, is directly related to power setting for the AWJSRA (fig. 30). Engine fuel flow is also given in figure 30 and table 1.

The domain over which these data define the engine model

$$0 \leqslant V \leqslant 250 \text{ knots}$$

$$0 \leqslant N_H/\sqrt{\tau} \leqslant 103.5$$

suffices to cover the range of airspeeds of interest for the AWJSRA and operation at or below maximum continuous power for temperatures above $-12°$ C.

The maximum steady thrust available in flight occurs at maximum continuous power, N_{mc}; it decreases with altitude and temperature and increases with airspeed, as shown in figure 31. The maximum cold thrust coefficient also occurs at N_{mc}. It varies principally with airspeed (fig. 31(c)) and is independent of pressure altitude. As seen, C_J is restricted to low values at cruise speeds (160 knots) and there is little effect of engine power on aerodynamic coefficients at higher speeds. Much higher values of C_J are available at landing speeds (65 knots) and at low speeds generally as desired for the lift augmentation system design.

Aerodynamic Forces

The aerodynamic forces in stability axes are written

$$\bar{F}_A = QS_W \begin{pmatrix} C_D \\ C_L \end{pmatrix} \tag{A4}$$

where C_L, C_D are the usual lift and drag coefficients and S_W is the wing area, 80.4 m^2.

The aerodynamic description of the AWJSRA used here is derived from reference 4, where wing-body lift and drag coefficients are tabulated as functions of three variables, $\{\alpha, \delta_f, C_J\}$, over the domain

$$\left. \begin{array}{l} \alpha \in [-10.5°, 27.5°] \\[1mm] \delta_f \in [5.6°, 72°] \\[1mm] C_J \in [0,2] \end{array} \right\} \tag{A5}$$

The data of reference 4 were based largely on wind-tunnel data, but more accurate data have since been obtained from flight tests (ref. 6) and are included in the model of this paper. In addition, the coefficients have been corrected for the symmetric deployment of aileron with flap that is built into the flap mechanism, and for the tail lift which is required to trim the aircraft. Ground effects, which occur at altitudes below 16 m are not included in the model.

50

The tail lift correction is computed from

$$\Delta C_{L_T} \simeq - \frac{1}{a_T} \left[c C_{M_{WB}} + a_L C_{L_{WB}} - a_D C_{D_{WB}} \right]$$

(A6)

Here, $C_{M_{WB}}$ is the wing-body pitching moment, c is the mean aerodynamic cord, and a_T, a_L, and a_D are the moment arms for tail lift and wing-body lift and drag forces (ref. 4). The tail lift correction contains only functions of $\{\alpha, \delta_f, C_J\}$ and can be included in the lift coefficient without increasing the number of independent variables. Variations in c.g. location with aircraft weight and the pitching moment due to engine thrust have only negligible effect on the tail lift and are neglected.

The resulting aerodynamic model is tabulated in table 2 and pictured in figure 32 as lift-drag polars for four flap settings, with lines of constant α and C_J mapped on each plot. During approach and landing the flap setting progresses slowly from 5.6° at cruise to 65° at landing. At cruise, engine power is seen to have little effect on lift and reduces the aerodynamic drag by exhausting pressurized air rearward through the flap. In any case, there is little available range of C_J at cruise speeds and correspondingly little effect of engine power so that the resulting model at cruise closely resembles that of a conventional aircraft and has a maximum C_L of about 2. At low speeds and maximum flap the available range of C_J is much greater and its effects on lift coefficient is pronounced with maximum C_L in the range of 4 to 5.

The purpose of a conventional flap is to increase the maximum C_L available from the wing in order to permit lower landing speeds. The special flap of the augmentor wing has the same purpose but obtains a higher $C_{L_{max}}$ than a conventional flap in order to obtain sufficiently low landing speeds for short field length landings. Thus, the polar plots in figure 32 although roughly similar to those for conventional aircraft, require an additional parameter, C_J, to account for engine power effects; they also exhibit large nonlinear variations with flap setting. As a result, the data required to define the aerodynamic force model is greatly increased compared to the single lift-drag polar required for CTOL aircraft.

Elevator Trimmap

In the analysis of the trim equation in this paper the control variables are taken as

$$\bar{u} = (\delta_f, \delta_t, \alpha, \nu)$$

of which $(\delta_f, \delta_t, \nu)$ are directly controlled by the autopilot through servos, and α is controlled by commands to the elevator servo. Therefore the relationship $\delta e(\bar{u})$ is necessary for the implementation of the autopilot and constraints on elevator usage will correspondingly limit the usable range of $\bar{u}$.

The elevator affects the aircraft forces and moments through the tail lift, which is modeled by the linear relation

$$L_T = L_{T_o} + L_{\delta e}\delta e \tag{A7}$$

with elevator travel limited to

$$\delta e \in [-25°, 15°] \tag{A8}$$

and

$$L_{\delta e} = QS_w C_{L_{\delta e}}$$

Elevator stall can be neglected since it has not been observed for angles of attack below wing stall. In addition, reduction of dynamic pressure at the tail due to the wing wake presence is also negligible because of the T-tail design of the aircraft. L_{T_o} is the tail lift at zero elevator angle and can be written as

$$L_{T_o} = QS_T C_{L_{T_\alpha}} \Delta\alpha_T$$

where

$$\Delta\alpha_T = \alpha - \varepsilon + L_T - \alpha_{o_T}$$

ε = tail downwash angle

i_T = tail incidence

α_{o_T} = angle of attack for which tail lift is zero

$$C_{L_{T_\alpha}} = \frac{\partial C_{L_T}}{\partial \alpha}$$

The downwash angle is generated from a complex model (ref. 4) whose independent variables are $\{\delta_f, \alpha_T, C_J\}$. Here, α_T is the wing angle of attack delayed by the time it takes for air to reach the tail from the wing:

$$\alpha_T = \alpha(t - \Delta t)$$

$$\Delta t = \frac{a_T}{V_A}$$

where a_T is the distance between wing and tail center of pressure. For steady flight α_T and α are equal. Values of the remaining parameters of the tail lift model, $C_{L_{\delta e}}$, . . ., α_{oT}, are given in reference 4.

52

The elevator is used to control the pitching moment balance, given by

$$I_y \dot{q} + (I_x - I_z)pr + I_{xz}(p^2 - r^2) = QS_W \left[cC_{M_{WB}} + a_L C_{L_{WB}} - a_D C_{D_{WB}} \right.$$

$$\left. -a_I C_{DR} + a_E C_T \right] + a_T \left(L_{T_o} + L_{\delta e} \delta e \right) \tag{A9}$$

Here, C_{DR}, C_T are dimensionless engine forces

$$C_{DR} \equiv \frac{m_E V_a}{QS_W} \ , \qquad C_T = \frac{T_H}{QS_W}$$

and a_I, a_E, a_T are the moment arms of the engine and tail lift forces. These moment arms are computed from a nominal center of gravity location. Changes in this location with aircraft weight are small and can be neglected in computing the tail lift and elevator setting for trim. Equation (A9) can be solved for δe and the resulting terms arranged in three parts to separate the effects of dynamic reactions, engine forces, and aerodynamic forces and moments.

$$\left. \begin{aligned}
\delta e &= \delta e_D + \delta e_E + \delta e_A \\[2mm]
\delta e_D &= \frac{(\dot{q} I_y + pr(I_x - I_z) + (p^2 - r^2) I_{xz})}{C_{L_{\delta e}} QS_T a_T} \\[2mm]
\delta e_E &= \frac{(a_I C_{DR} - a_E C_T) S_w}{C_{L_{\delta e}} a_T} \\[2mm]
\delta e_A &= -\left(cC_{M_{WB}} + a_L C_{L_{WB}} - a_D C_{D_{WB}} \right) \frac{S_w}{C_{L_{\delta e}} S_T a_T} - \frac{C_{L_{T_\alpha}}}{C_{L_{\delta e}}} \Delta \alpha_T
\end{aligned} \right\} \tag{A10}$$

In the present analysis the elevator setting for steady or very nearly steady flight conditions along the nominal path is of interest so that the dynamic term can be neglected and then the elevator setting for trim is

$$\delta e_T = \delta e_A(\alpha, \delta_f, C_J) + \delta e_E \tag{A11}$$

The principal term in equation (A11) is δe_A, which is a function of only $\{\alpha, \delta_f, C_J\}$ and can be calculated and tabulated over the same grid for which the lift and drag coefficients are given. The results are shown in figure 33 and table 3. Ground effects (which are of a significant size) are omitted from δe_A.

The physical limits of elevator travel (eq. (A8)) limit the range of $\overline{\mu}$ for which trim is possible. Under dynamic conditions, the elevator is also used transiently to control attitude and therefore the allowed trim settings must be further restricted within equation (A8) to provide a margin for the

53

attitude control function. For the AWJSRA design this margin was taken simply as 8° and it was found that the constraints on elevator usage had almost no influence in establishing the boundaries of the flight envelope or the range of acceptable configurations at any flight condition within the envelope.

APPENDIX B

SOLUTION OF THE TRIM EQUATIONS

Solution of the aircraft trim equations for two control variables is required extensively in computing the configuration schedule and is proposed as part of the Trimmap element of the flight-control logic (figs. 1, 2, and 10). These equations are nonlinear and are solved numerically in the case of the AWJSRA; this is expected to be the case for powered-lift aircraft generally so that efficient general approaches to the solution of such equations are of interest in the control system design.

An exhaustive grid search procedure was used in this work and is described in this appendix. This method is conceptually simple; data defining the aerodynamic and engine forces are assumed given as tables of values on a grid of points covering the domain of interest. Table interpolation is used to provide a piecewise linear model on each piece of the grid and these linear equations are solved piece by piece until the piece containing the solution is found or the grid is exhausted. The existence of a solution is determined in a finite number of steps, and its uniqueness is determined from properties of the model data.

Alternative methods based on Newtonian iteration were also investigated. The classical Newton method is simple and well known but subject to an array of difficulties in practice affecting both reliability and computational requirements. These difficulties motivate the modifications found in a variety of quasi-Newton methods (ref. 13), such as the Newton-Powell algorithm (ref. 14). An advantage of iterative searches is their general applicability; the same iterative procedure applies to the solution for any pair of variables in the AWJSRA trim equation and to solving the trim equation for any powered-lift aircraft, including cases where more than two equations in two unknowns must be solved, such as the tilt rotor aircraft which requires the solution of eight equations in eight unknowns. The Powell algorithm requires little more than a user-supplied function evaluation subroutine. In addition, the adaptive search of an iterative scheme may converge in fewer steps on a distant solution than the rigid grid search pattern of the exhaustive grid search method, especially if the aircraft model is not strongly nonlinear.

For flight control use, important properties of the trim solution algorithms are computation time and reliability. The Powell algorithm was tested with the AWJSRA model after modification to enforce constraints on the search domain. It proved efficient with convergence to a solution in a few steps for all cases tested. However, methods of proving the convergence of such algorithms for all operational conditions, given the aircraft model, do not appear to be available. Consequently, the exhaustive grid search procedure was adopted for the present control system design. Computation time requirements are proportional to the product of the time required for each step in a search and the number of steps to converge on a solution. An upperbound on computation time is given by the case of searching for a solution when none

exists. This case will occur in practice in the absence of existence conditions that can be tested before entering the algorithm. When solutions do exist, the convergence rate or average number of steps to converge is a property of interest.

For reliability, convergence of the algorithm to a solution, if it exists, and correct selection of a single solution if several exist, are necessary properties. In addition, such software properties as insensitivity to round-off error, and risk of programming error, which increases with the complexity of the algorithm's structure, are relevant.

For convenience, the trim equations for the AWJSRA are repeated here

$$
\begin{pmatrix} A_{u_C} \\ A_{N_C} \end{pmatrix} = \left[T_H \begin{pmatrix} \cos(\alpha + \nu) \\ \sin(\alpha + \nu) \end{pmatrix} - \dot{m}_E V_A \begin{pmatrix} 1 \\ 0 \end{pmatrix} + QS_w \begin{pmatrix} -C_D \\ C_L \end{pmatrix} \right] \frac{1}{W}
\tag{B1}
$$

where $T_H(N_H/\sqrt{\tau}, \delta, V_A)$, $\dot{m}_E(N_H/\sqrt{\tau}, \delta)$, $C_D(\alpha, \delta_f, C_J)$, $C_L(\alpha, \delta_f, C_J)$ are scalar functions of the control variables or of auxiliary functions of the controls and are given as tabulated data in appendix A. A following section of this appendix (Exhaustive Grid Search Solution Method) describes exhaustive grid search algorithms for solving equation (B1) for values of the control pairs, $\{\alpha, \nu\}$ and $\{\alpha, \delta_f\}$, which yield the commanded applied specific forces, (A_{u_C}, A_{N_C}), given the values of all remaining parameters in equation (B1). Searches over one and two-dimensional grids are used in the solutions. These two algorithms are sufficient for the work described in this paper but, in general, solutions of equation (B1) for any pair of variables among $\{\bar{x}, \bar{p}, \bar{u}\}$ are of interest in the analysis of various performance problems.

Table interpolation is required extensively for function evaluation in these algorithms. Interpolation formulas which are continuous over the table domain are given next.

Table Interpolation

The evaluation of functions, such as C_L, C_D, etc., by interpolation of stored tabulated values is used repeatedly in the trim solution algorithms. Interpolation formulas for functions of three variables are given below; those for functions of one or two variables follow as special cases.

Assume that a table of values of the function, $f(x, y, z)$, has been stored for all points in a grid covering the domain of interest; that is, the set of values

$$
\left\{ f(x_i, y_j, z_k); \quad i = 1, 2, \ldots, N_x, \quad j = 1, \ldots, N_y, \quad k = 1, \ldots, N_z \right\}
\tag{B2}
$$

This table contains $N_x \cdot N_y \cdot N_z$ values and the grid subdivides the domain

$$\mathscr{D} = \left\{ (x,y,z): \quad x \in \left[x_1, x_{N_x}\right], \quad y \in \left[y_1, y_{N_y}\right], \quad z \in \left[z_1, z_{N_z}\right] \right\} \qquad \text{(B3)}$$

into $(N_x - 1) \cdot (N_y - 1) \cdot (N_z - 1)$ box-shaped pieces.

The original function is approximated as piecewise linear by interpolating this table. For a given point, (x, y, z), in $\mathscr{D}$ the table is interpollated in two steps as follows. First, locate the grid piece containing the point (x, y, z); that is, find

$$(i,j,k) \quad \text{such that} \quad x \in [x_i, x_{i+1}), \quad y \in [y_j, y_{j+1}), \quad z \in [z_k, z_{k+1}) \qquad \text{(B4)}$$

This is easily done by several methods; the one used here is defined later in equation (B14) and is efficient in real time simulation and control. Having found (i, j, k) it is convenient to define the following vector which locates the point (x, y, z) relative to (x_i, y_j, z_k) and normalizes the coordinates

$$\bar{\rho} \equiv \left(\frac{x - x_i}{x_{i+1} - x_i} , \quad \frac{y - y_j}{y_{j+1} - y_j} , \quad \frac{z - z_k}{z_{k+1} - z_k} \right)^T \equiv \left(\rho_x, \rho_y, \rho_z \right)^T \qquad \text{(B5)}$$

The coordinates of $\bar{\rho}$ are each numbers in $[0, 1]$. For brevity, the notation $\{f_{000}, f_{100}, \ldots, f_{111}\}$ is adopted to refer to the tabulated values of f at the eight corners of the grid piece: (x_i, y_j, z_k), (x_{i+1}, y_j, z_k), ..., $(x_{i+1}, y_{j+1}, z_{k+1})$.

Second, the linear approximation of f is given from the usual truncated Taylor series expansion of f about (x_i, y_j, z_k):

$$\hat{f}(\bar{\rho}) = f_{000} + \bar{\rho} \cdot (\bar{\nabla}f)_o, \quad \rho_x, \rho_y, \rho_z \in [0,1] \qquad \text{(B6a)}$$

The approximation, $\hat{f}$, is required to be continuous and to match the tabulated values. However, the original function, f, is in general nonlinear, and its values at the eight corners of the grid piece will not fall in a single hyperplane, such as equation (B6a). Consequently, to obtain the desired properties for $\hat{f}$ it is necessary to define hyperplanes by calculating the gradient vector, $\bar{\nabla}f$, from a different set of four grid points depending on the location of $\bar{\rho}$ within the grid pieces. This is illustrated in sketch (a) for the simpler case of a function of two variables. The rectangular domain is divided into two triangular pieces and the gradient calculated from a different set of three grid points in each triangle as noted in the sketch. The resulting function is linear in each triangle and continuous at their common edge. In three dimensions the linear approximation becomes more complex and requires subdivision of the box-shaped domain into six tetrahedral pieces; approximate formulas for the gradient vector are:

$$[\bar{\nabla}f]_o^T = \begin{cases} [(f_{100} - f_{000}),(f_{111} - f_{101}),(f_{101} - f_{100})] & \rho_x \geqslant \rho_z \geqslant \rho_y \\[8pt] [(f_{100} - f_{000}),(f_{110} - f_{100}),(f_{111} - f_{110})] & \rho_x \geqslant \rho_y \geqslant \rho_z \\[8pt] [(f_{101} - f_{001}),(f_{111} - f_{101}),(f_{001} - f_{000})] & \rho_z \geqslant \rho_x \geqslant \rho_y \\[8pt] [(f_{111} - f_{011}),(f_{011} - f_{001}),(f_{001} - f_{000})] & \rho_z \geqslant \rho_y \geqslant \rho_x \\[8pt] [(f_{111} - f_{011}),(f_{010} - f_{000}),(f_{011} - f_{010})] & \rho_y \geqslant \rho_z \geqslant \rho_x \\[8pt] [(f_{110} - f_{010}),(f_{010} - f_{000}),(f_{111} - f_{110})] & \rho_y \geqslant \rho_x \geqslant \rho_z \end{cases} \quad \text{(B6b)}$$
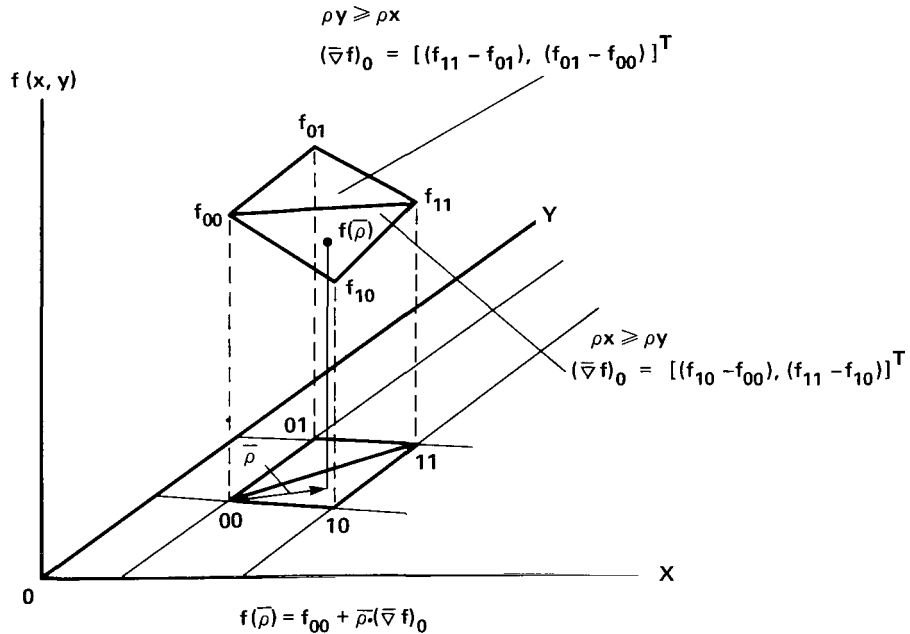
Sketch (a).- Linear interpolation.

Interpolation formulas other than equations (B6) are also available and have different properties; for example, subdivision of the grid piece as in equation (B6b) is avoided by adding terms in cross-products of $\{\rho_x, \rho_y, \rho_z\}$ from the Taylor series, which yields

$$\hat{f}(\bar{\rho}) = f_{000} + \bar{\rho} \cdot (f_{100} - f_{000}, f_{010} - f_{000}, f_{001} - f_{000})$$

$$+ \rho_x \rho_y (f_{110} - f_{010} - f_{100} + f_{000})$$

$$+ \rho_x \rho_z (f_{101} - f_{001} - f_{100} + f_{000})$$

$$+ \rho_y \rho_z (f_{011} - f_{001} - f_{010} + f_{000})$$

$$+ \rho_x \rho_y \rho_z (f_{111} - f_{011} - f_{101} + f_{001} - f_{110} + f_{010} + f_{100} - f_{000})$$

$$\text{(B7)}$$

This formulation extends to more than three variables by retaining all terms to first order in $\{\rho_x, \rho_y, \rho_z, \ldots\}$ from the general Taylor series expansion (cf. ref. 15).

The linear approximation in equations (B6) works well for functions of two variables, including the inversion of such functions, but equation (B6b) is difficult to generalize to four or more variables. The quasi-linear approximation of equation (B7) has worked easily for functions of two or three variables, including their inversion. For some applications, it is useful for $\hat{f}$ to have continuous first derivatives over the table domain $\mathscr{D}$, but that property was not required in the present work; equation (B7) has discontinuous derivatives on the surfaces of the grid pieces while equations (B6) has discontinuous derivatives along all interior boundary surfaces implied by equation (B6b) as well as on the grid piece surfaces.

Exhaustive Grid Search Solution Method

Solution for nozzle and angle of attack— The problem is to solve the trim equations (B1) for $\{\alpha, \nu\}$ given the values of all remaining variables in the equations. It is convenient to define the quantities

$$\left. \begin{aligned} E_u &\equiv \frac{A_{u_c} + (QS_wC_D + \dot{m}_E V_A)}{W} \\[2ex] E_N &\equiv \frac{A_{N_c} - QS_wC_L}{W} \\[2ex] \bar{E} &\equiv (E_u, E_N)^T \end{aligned} \right\} \tag{B8}$$

In equations (B8), C_D and C_L are functions of α and are assumed tabulated on a grid of values

$$\{\alpha_i, \quad i = 1, \ldots, N_\alpha\}$$

where α_{N_α} corresponds to stall or maximum C_L. The trim equations can be rearranged to isolate the nozzle angle in a single equation by substituting equations (B8) in the trim equation, which becomes

$$\bar{E} = T_H (\cos(\alpha + \nu), \sin(\alpha + \nu))^T$$

and then it follows that

$$|\bar{E}(\alpha)| = \frac{T_H}{W} \tag{B9}$$

$$\nu = \alpha + \tan^{-1}\left(\frac{E_N}{E_u}\right) \tag{B10}$$

Since $\bar{E}$ depends on α only and can be tabulated for the grid points, $\{\alpha_i\}$, equation (B9) can be solved numerically for α after which ν is calculated from the closed form expression in equation (B10).

The problem of solving equation (B9) is visualized in sketch (b), which shows the operating point (A_{u_c}, A_{N_c}) for which trim values of $\{\alpha, \nu\}$ are desired, and the line traced out by the aerodynamic forces

$$\bar{F}_A = \frac{QS_w}{W}\begin{pmatrix} -C_D \\ C_L \end{pmatrix} - \dot{m}_E \frac{V_A}{W}\begin{pmatrix} 1 \\ 0 \end{pmatrix}$$
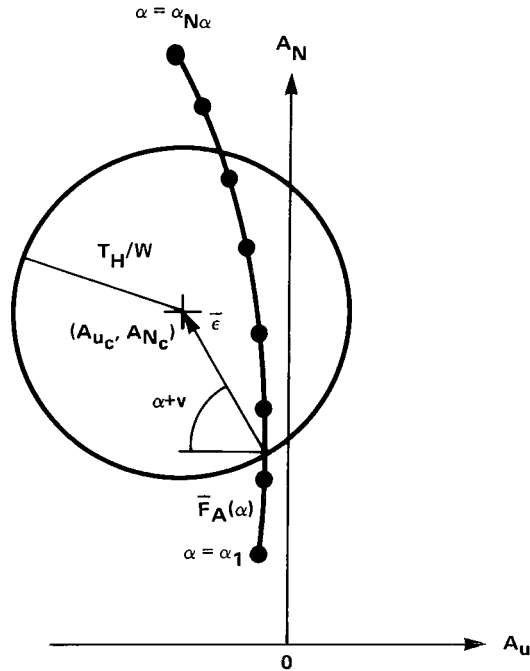
Sketch (b).- Solution of equation (B8).

60

as α is varied over the domain $[\alpha_1, \alpha_{N_\alpha}]$. This line is closely related to the $C_L - C_D$ polars (appendix A); it has a near-vertical slope and A_N is strictly increasing in α below the stall angle. The solution of equation (B9) is equivalent to finding α^* such that the distance from the line to the operating point, $|\bar{E}(\alpha^*)|$, matches the ratio, T_H/W; this is visualized in the sketch as the intersection of the line with a circle of radius T_H/W. In general, there may be no solution (the line is entirely outside or inside the circle), one solution (one endpoint of the line falls inside the circle), or two solutions as in the case sketched above. When two solutions occur, the lower value of α is selected in order that the resulting nozzle angle fall within the hardware limits on the nozzle, $[6°, 104°]$. The higher value of α corresponds to a negative value of E_N and this implies a negative nozzle angle and downward directed thrust vector from equation (B10) in almost all cases.

The numerical solution of equation (B9) is considered in two parts: first, a method is defined for testing whether a given interval of the α-grid, say $[\alpha_i, \alpha_{i+1})$, contains the solution; and, second, a procedure for searching the intervals of the grid is given.

The interval $[\alpha_i, \alpha_{i+1})$ can be tested as follows. Define the notation

$$
\left.
\begin{aligned}
\bar{E}_i &\equiv \bar{E}(\alpha_i) \\[1em]
\Delta E_i &\equiv \bar{E}_{i+1} - \bar{E}_i \\[1em]
\rho_\alpha &\equiv \frac{\alpha - \alpha_i}{\alpha_{i+1} - \alpha_i}
\end{aligned}
\right\} \tag{B11}
$$

Then $\bar{E}(\alpha)$ is given on $[\alpha_i, \alpha_{i+1}]$ by:

$$
\bar{E}(\alpha) = \bar{E}_i + \Delta E_i \rho_\alpha \tag{B12}
$$

This is substituted in equation (B9) and the resulting quadratic in ρ_α solved:

$$
\rho_\alpha^* = - \frac{\bar{E}_i \cdot \overline{\Delta E_i}}{\Delta \bar{E}_i^2} - \sqrt{\left(\frac{\bar{E}_i \cdot \Delta E_i}{\Delta \bar{E}_i^2}\right)^2 + \left(\frac{T}{W} - \bar{E}_i^2\right)\Big/\Delta E_i^2} \tag{B13}
$$

While the quadratic has two solutions for ρ_α^*, only the smaller solution, given in equation (B13), need be tested because the larger one corresponds to nozzle settings outside the nozzle hardware limits. If the condition

$$
\rho_\alpha^* \in [0,1)
$$

is satisfied by equation (B13) then the solution occurs in the tested interval, $[\alpha_i, \alpha_{i+1})$ and is

$$\alpha^* = \alpha_i + \rho_\alpha^* (\alpha_{i+1} - \alpha_i)$$

Otherwise, the solution either does not exist or occurs in some other interval of the α-grid.

Each interval of the α-grid is tested as described above until either a solution is found or the grid is exhausted with no solution in $N_\alpha - 1$ steps. While the grid can be searched in any order a minimum computation time search ordering is desired for real time control or simulation applications. If a solution exists, computation time is proportional to the number of intervals tested before finding the solution and can be minimized, on the average, by testing intervals in the order of the likelihood that they contain the solution. For flight control, solutions are required every control cycle and the expected value of the solution corresponds to the nominal path and is either constant or slowly varying with time. Consequently, the most probable interval is the same interval in which it was found for the previous control cycle and probability decreases with distance from this interval. The corresponding search ordering begins in the same interval, I, in which the solution was previously found and expands to neighboring intervals out to the ends of the grid; that is, in the order $\{I \pm k\}$ generated as k varies in the expression

$$i = \begin{cases} I - k & k = 1, \ldots, I - 1 \\ I + k & k = 1, \ldots, N_\alpha - I - 1 \end{cases} \tag{B14}$$

The maximum computation time required with this search procedure occurs when all intervals must be searched and is proportional to $N_\alpha - 1$. This worst-case time is minimized by minimizing the number of grid points in the α-grid used in the aerodynamic model within the limits imposed by the desired model accuracy.

Solution for throttle and angle of attack— The problem is to solve the trim equations for $\{\alpha, \delta_t\}$ given the values of all remaining variables in these equations. The applied acceleration due to engine and aerodynamic forces is expressed as a function of (α, N_c) by

$$\bar{a}(\alpha, N_c) = \left[T_H \begin{pmatrix} \cos(\alpha + \nu) \\ \sin(\alpha + \nu) \end{pmatrix} - \dot{m}_E V_A \begin{pmatrix} 1 \\ 0 \end{pmatrix} + QS_w \begin{pmatrix} -C_D \\ C_L \end{pmatrix} \right] \frac{1}{W} \tag{B15}$$

Here, N_c denotes the corrected engine power, $N_H / \sqrt{\tau}$. It is convenient to solve for N_c in place of throttle since the engine output is tabulated in appendix A for this parameter on the grid

$$\left\{ N_{c_j}; \quad j = 1, 2, \ldots, N_{N_c} \right\}$$

The throttle setting corresponding to any value of N_c is then given from figure 30. The problem is now to determine (α^*, N_c^*) such that the commanded acceleration (A_{u_c}, A_{N_c}) or, for brevity, $\bar{a}_c$, is obtained; that is, solve

$$\bar{a}(\alpha, N_c) = \bar{a}_c \qquad (B16)$$

The applied acceleration, $\bar{a}(\alpha, N_c)$, can be tabulated for values of (α, N_c) in the grids used for the aircraft and engine models. This yields the table

$$\left\{ \bar{a}_{ij} \equiv \bar{a}\left(\alpha_i, N_{c_j}\right) \qquad i = 1, \ldots, N_\alpha, \quad j = 1, \ldots, N_{N_c} \right\} \qquad (B17)$$

On a grid-piece of the domain, say $[\alpha_i, \alpha_{i+1}] \otimes [N_{c_j}, N_{c_{j+1}}]$, $\bar{a}$ is given from the linear interpolation formula (B5) as

$$\bar{a}(\alpha, N_c) = \bar{a}_{ij} + [\bar{\nabla}\bar{a}]_{ij} \begin{pmatrix} \rho_\alpha \\ \rho_{N_c} \end{pmatrix} ; \quad \rho_\alpha, \rho_{N_c} \in [0,1] \qquad (B18)$$

where

$$\rho_\alpha \equiv \frac{\alpha - \alpha_i}{\alpha_{i+1} - \alpha_i}$$

$$\rho_{N_c} \equiv \frac{N_c - N_{c_j}}{N_{c_{j+1}} - N_{c_j}}$$

Using equations (B6), the Jacobian is given by the 2 × 2 matrices

$$[\bar{\nabla}\bar{a}]_{ij} \equiv \begin{cases} \left[\bar{a}_{i+1,j} - \bar{a}_i, \ \bar{a}_{i+1,j+1} - \bar{a}_{i+1,j}\right] & \rho_{N_c} \leqslant \rho_\alpha \\ \left[a_{i+1,j+1} - \bar{a}_{i,j+1}, \bar{a}_{i,j+1} - \bar{a}_{ij}\right] & \rho_\alpha \leqslant \rho_{N_c} \end{cases} \qquad (B19)$$

The problem of solving equation (B16) is visualized in sketch (c). Equations (B17) and (B18) map values of (α, N_c) into values of (A_u, A_N) and this map is shown in the sketch for the grid lines of the tabulated model. The mapping differs depending on configuration; in the conventional configuration and for CTOL aircraft generally the effects of the engine power and angle of attack are nearly orthogonal and $A_N(\alpha, N_c)$ is nearly independent of engine power. Consequently, there is little coupling between the two equations and the normal acceleration equation can be solved approximately for α^*. However, in the powered-lift configuration, $A_N(\alpha, N_c)$ depends strongly on engine power, both from thrust vectoring and lift augmentation, and α^* can no longer be solved separately from N_c^*. Nevertheless, the solution of equation (B16), if it exists, is unique at all flight conditions and configurations in the design domain based on the model properties:

1. $A_N(\alpha, N_c)$ is monotonic and strictly increasing in α and N_c

2. $A_u(\alpha, N_c)$ is monotonic and strictly increasing in N_c along any line for which $A_N(\alpha, N_c)$ is constant
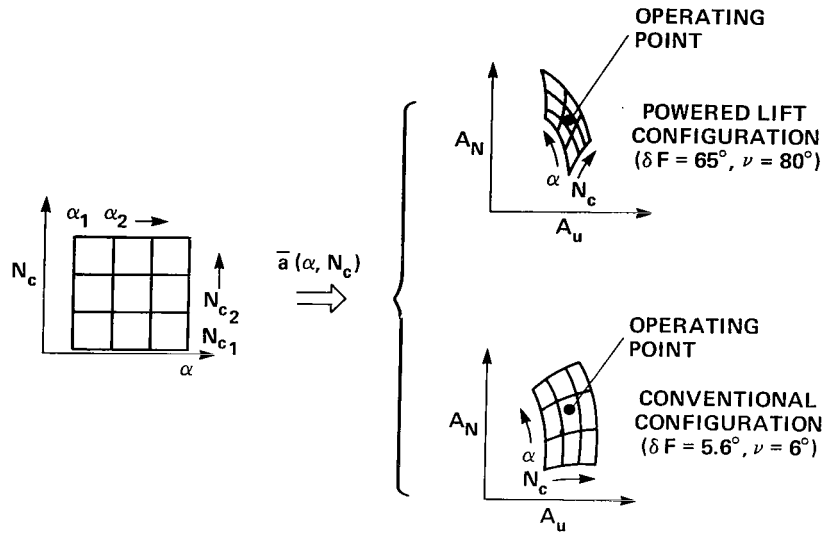
Sketch (c).- Acceleration map for (α, δ_t).

The numerical solution of equation (B16) is considered in two parts; first, a method of testing whether a given grid piece contains the solution is given and then a procedure for searching the pieces of the two-dimensional grid is given.

A grid piece, say $[\alpha_i, \alpha_{i+1}] \otimes [N_{cj}, N_{cj+1}]$, can be tested to determine if it contains the solution by solving equation (B18)

$$\begin{pmatrix} \rho_\alpha^* \\ \rho_{N_c}^* \end{pmatrix} = \left[\nabla a_{ij}\right]^{-1}\left(\bar{a}_c - \bar{a}_{ij}\right) \tag{B20}$$

This solution is calculated once for each Jacobian given in equation (B19). The result in equation (B20) gives the solution of equation (B16) if it satisfies the necessary and sufficient conditions

$$0 \leqslant \rho_{N_c}^* \leqslant \rho_\alpha^* \leqslant 1$$

or

$$0 \leqslant \rho_\alpha^* \leqslant \rho_{N_c}^* \leqslant 1$$

depending on which of the two gradients in equation (B19) was used. If these are satisfied, then the solution is

$$\alpha^* = \alpha_i + \rho_\alpha^*(\alpha_{i+1} - \alpha_i)$$

$$N_c^* = N_{cj} + \rho_{N_c}^*\left(N_{cj+1} - N_{cj}\right)$$

64

Each piece of the grid is tested until either a solution is found or the grid is exhausted with no solution in $(N_\alpha - 1) \cdot (N_{N_C} - 1)$ steps. A search ordering which is efficient in real-time use is defined next by extension of equation (B14) to two dimensions. This ordering tests grid pieces approximately in the order of their probability of containing the solution; that is, it begins at the grid piece (I, J) in which the solution was found for the preceding control cycle, and expands out to the ends of the two-dimensional grid, testing groups of grid pieces which frame the starting piece (I, J) at each step. The grid pieces in each frame are assumed to be equally likely to contain the solution. The indices for the grid pieces in the kth such frame (see sketch (d)) are enumerated in equation (B12) for each of the four sides of the frame; grid pieces and sides which are outside the model domain are deleted from the enumeration by the extremes placed on i, j, and k.
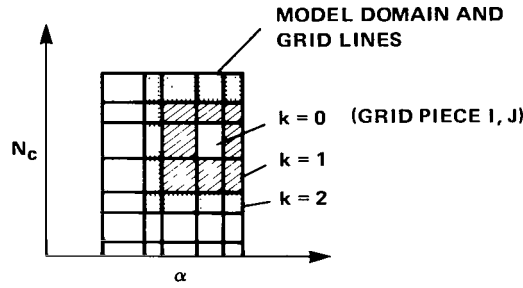
Sketch (d).- Two-dimensional grid search pattern.

$$
\{(i,j)\}^{(k)} = \begin{cases} (I - k, j) & k < I \\ (I + k, j) & k < N_\alpha - I \\ (i, J + k - 1) & k < N_\alpha - J \\ (i, J - k) & k < J \end{cases}
\quad
\begin{aligned}
& j = j_{min}, j_{min} + 1, \ldots, j_{max} \\
& \quad j_{min} = \max\{1, J - k\}; \\
& \quad j_{max} = \min\{N_{N_C} - 1, J + k\} \\
& i = i_{min}, i_{min} + 1, \ldots, i_{max} \\
& \quad i_{min} = \max\{1, I - k + 1\} \\
& \quad i_{max} = \min\{N_\alpha - 1, I + k - 1\}
\end{aligned}
$$

$$\text{(B21)}$$

The search proceeds, taking $k = 0, 1, 2, \ldots$, until a solution is found or the grid is exhausted after $(N_\alpha - 1) \cdot (N_{N_C} - 1)$ grid pieces have been tested. This search ordering is applicable to the solution of any function of two variables.

CONTROL MARGIN AND CONFIGURATION SCHEDULE COMPUTATIONS

Computation of Control Margin

Control margin is a measure of the acceleration capability available to regulate path errors by varying the feedback controls around their trim values associated with the nominal flight condition. Control margin depends strongly on configuration and appears in the configuration schedule design both as a constraint on acceptable configurations and as a parameter to be optimized. Several different control margins

$$CM_{\delta_f}(x,p), \quad CM_{\delta_f,\nu}(x,p), \quad CM_{\delta_f,\delta_t}(x,p), \quad CM_{\delta_f,\alpha}(x,p)$$

were defined in the text associated, respectively, with the use of three controls for regulation and with various pairs of controls. The subscripts in the notation indicate the controls held fixed in each case. Control margin was defined as follows. The acceleration capability of the regulator, given δ_f, V_E, p, is

$$\mathscr{A}_{\delta_f}(V_E,p) = \left\{ (A_u(V_E,p,u), A_N(V_E,p,u)): \quad \alpha \in \mathscr{A}_{REG}, \delta_t \in \mathscr{T}_{REG}, \nu \in \mathscr{N}_{REG} \right\} \qquad (C1)$$

where accelerations are generated using the aircraft model (eq.(9)). Next, define the region enclosed by ellipses with 5-to-1 axes ratios and centered at $\overline{ac}$

$$\mathscr{E}\left(R, A_{u_C}, A_{N_C}\right) \equiv \left\{ (A_u, A_N): \quad 25\left(A_u - A_{u_C}\right)^2 + \left(A_N - A_{N_C}\right)^2 \leqslant R^2 \right\} \qquad (C2)$$

The control margin is then the largest such ellipse that can be inscribed in the envelope of $\mathscr{A}_{\delta_f}(V_E,p)$, as shown in figure 34.

$$CM_{\delta_f}(x,p) \equiv \max\left\{ R: \quad \mathscr{E}\left(R, A_{u_C}, A_{N_C}\right) \subset \mathscr{A}_{\delta_f}(V_E,p) \right\} \qquad (C3)$$

Control margin is computed in three steps and these are outlined below.

1. Generate the envelope of $\mathscr{A}_{\delta_f}(V_E, p)$ (or of $\mathscr{A}_{\delta_f,\nu}$, $\mathscr{A}_{\delta_f,\delta_t}$, $\mathscr{A}_{\delta_f,\alpha}$)

2. Determine if (A_{uc}, A_{Nc}) is inside $\mathscr{A}_{\delta_f}(V_E, p)$ (or inside $\mathscr{A}_{\delta_f,\nu}$, etc.)

3. If it is, calculate $CM_{\delta_f}(x, p)$ (or $CM_{\delta_f,\nu}$, etc.)

The acceleration envelope in step 1 is generated approximately as a polygon. The end points of the sides of the polygon are computed as a set of points $\{(A_u, A_N)_i\}$ on the envelope corresponding to a sequence of values of the controls $\{\overline{u}_i\}$ that form a grid covering the regulator regime. For

convenience in later calculations, these points are generated in a clockwise manner around the envelope and the controls $\{\bar{u}_i\}$ must be taken in a definite sequence in order to do so. The required computations are then

1. Construct grids of values of the controls, α, δ_t, ν, covering their permitted ranges for regulation, $[\alpha_{min}, \alpha_{max}]$, $[\delta_{t_{min}}, \delta_{t_{max}}]$, $[\nu_{min}, \nu_{max}]$. For example,

$$
\left.
\begin{aligned}
\alpha_i &= \alpha_{min} + \left(\alpha_{max} - \alpha_{min}\right)\frac{i-1}{n-1} \\[1em]
\delta_{t_i} &= \delta_{t_{min}} + \left(\delta_{t_{max}} - \delta_{t_{min}}\right)\frac{i-1}{n-1} \\[1em]
\nu_i &= \nu_{min} + \left(\nu_{max} - \nu_{min}\right)\frac{i-1}{n-1}
\end{aligned}
\right\}
\qquad i = 1, \ldots, n
$$

2. Generate and store values of $(A_u(V_E, p, u_i), A_N(V_E, p, u_i))$ in the following order:

$$
\begin{aligned}
u_i &= (\delta_f, \alpha_1, \delta_{t_1}, \nu_i) & i &= 1, \ldots, n \\[0.6em]
u_{n+i} &= (\delta_f, \alpha_i, \delta_{t_1}, \nu_n) & i &= 1, \ldots, n \\[0.6em]
u_{2n+i} &= (\delta_f, \alpha_n, \delta_{t_i}, \nu_n) & i &= 1, \ldots, n \\[0.6em]
u_{4n+1-i} &= (\delta_f, \alpha_n, \delta_{t_n}, \nu_i) & i &= n, \ldots, 1 \\[0.6em]
u_{5n+1-i} &= (\delta_f, \alpha_i, \delta_{t_n}, \nu_i) & i &= n, \ldots, 1 \\[0.6em]
u_{6n+1-i} &= (\delta_f, \alpha_1, \delta_{t_i}, \nu_1) & i &= n, \ldots, 1
\end{aligned}
$$

The envelope, $\mathscr{A}_{\delta_f}(V_E, p)$, now consists of 6n points $\{(A_{u_i}, A_{N_i}), i = 1, \ldots, 6n\}$ with successive points connected by straight lines. A typical $\mathscr{A}_{\delta_f}$ is shown in figure 35. The envelopes, $\mathscr{A}_{\delta_f,\delta_t}$, $\mathscr{A}_{\delta_f,\nu}$, $\mathscr{A}_{\delta_f,\alpha}$, are generated similarly except that another control in addition to flap is held fixed, and this reduces the number of points to 4n.

A simple geometric criterion can be used to determine whether the given operating point (A_{u_c}, A_{N_c}) is inside the envelope (step 2 of the computations). Let $\{\bar{p}_i, i = 1, \ldots, 6n\}$ refer to the points generated in step 1 to define the figure, and let θ_i be the angle subtended at the operating point, $\bar{p}_c$, by the directed line segment joining $\bar{p}_i$, $\bar{p}_{i+1}$ (see fig. 36)

$$
\theta_i = \sin^{-1}\left(\frac{\bar{\ell}_i \otimes \bar{\ell}_{i+1}}{|\bar{\ell}_i| \; |\bar{\ell}_{i+1}|}\right) \qquad -\frac{\pi}{2} < \theta_i < \frac{\pi}{2}
$$

where

$$\bar{\ell}_i = \bar{p}_i - \bar{p}_c$$

$$\bar{\ell}_{i+1} = \bar{p}_{i+1} - \bar{p}_c$$

and then

$$\bar{p}_c \in \mathscr{A} \quad \text{IFF} \quad \Sigma\ \theta_i = 2\pi$$

$$\bar{p}_c \notin \mathscr{A} \quad \text{IFF} \quad \Sigma\ \theta_i = 0$$

Assuming $\bar{p}_c$ is in $\mathscr{A}$, the control margin can now be calculated. The problem of calculating the largest ellipse of the form given in equation (C2), with center at (A_{u_c}, A_{N_c}) which can be inscribed in the envelope, $\mathscr{A}$, generated by the points $\{(A_{u_i}, A_{N_i})\}$ is equivalent to finding the radius of the largest circle centered at $(5A_{u_c}, A_{N_c})$ which can be inscribed in the envelope $\mathscr{A}'$, generated by the points $\{(5A_{u_i}, A_{N_i})\}$. For simplicity, the notation $\bar{p}'$ will refer to points $(5A_u, A_N)$. The control margin is calculated as the smallest distance from the operating point $\bar{p}'_c$ to any one of the sides of the polygon $\mathscr{A}'$, as described next.

Let L_i be the line segment forming the ith side of the envelope. The minimum distance, R_i, from the point, $\bar{p}'_c$, to this segment is the perpendicular distance to the segment if the intersection of the perpendicular occurs within L_i. Otherwise, it is the lesser of the distances to the end points of L_i. To calculate R_i first define unit vectors, $\bar{u}$, $\bar{n}$ along and normal to the line segment L_i (see fig. 37).

$$\bar{u} = \frac{\bar{p}'_{i+1} - \bar{p}'_i}{|\bar{p}'_{i+1} - \bar{p}'_i|} = (\cos \sigma, \sin \sigma)^T$$

$$\bar{n} = (\sin \sigma, -\cos \sigma)^T$$

Then the line segment, L_i, can be given as

$$L_i = \left\{ \bar{p}' = \bar{p}'_i + \alpha\bar{u}; \quad \alpha \in \left[0, |\bar{p}'_{i+1} - \bar{p}'_i|\right] \right\}$$

where α measures the distance along $\bar{u}$ from the point, $\bar{p}'_i$. The perpendicular from $\bar{p}'_c$ intersects the extension of L_i at

$$\alpha_i = (\bar{p}'_c - \bar{p}'_i) \cdot \bar{u}$$

and then the minimum distance to L_i is

$$R_i = \begin{cases} |\bar{p}'_c - \bar{p}'_i| & \text{If } \alpha_i \leqslant 0 \\ |(\bar{p}'_c - \bar{p}'_i) \cdot \bar{n}| & \text{If } \alpha_i \in \left[0, |\bar{p}'_{i+1} - \bar{p}'_i|\right] \\ |\bar{p}'_c - \bar{p}'_{i+1}| & \text{If } \alpha_i \geqslant |\bar{p}'_{i+1} - \bar{p}'_i| \end{cases}$$

Finally, the control margin is the smallest such distance among the sides of the polygon

$$CM(\bar{p}_c) \equiv \min\{R_i, \quad i = 1, \ldots, N\}$$

Admissible Flap Settings

The flap schedule was calculated empirically by determining the range of acceptable flap settings at each flight condition and selecting the maximum such setting. The computational steps required are described below; they utilize the previously defined trim solution and control margin algorithms as well as the constraint list from the text.

1. Define grids $\{V_{E_i}\}$, $\{A_{u_j}\}$ and $\{\delta_{f_i}\}$ which cover the design ranges of interest for V_E, A_u and δ_f given in $\mathscr{X}_o$, $\mathscr{U}_o$.

2. Generate and store acceleration envelopes for these grids

$$\left\{ \mathscr{A}_{\delta f}\left(V_{E_i}, \delta_{f_\ell}, \bar{p}_s\right) \right\}$$

The standard parameter values, $\bar{p}_s$, are used.

3. For each value of $\bar{x}$ in the set given by

$$A_N = 1$$

$$A_u \in \{A_{u_j}\}$$

$$V_E \in \{V_{E_i}\}$$

determine those δ_f in $\{\delta_{f_\ell}\}$ for which

$$CM_{\delta_f}(\bar{x}, \bar{p}_s) \geqslant 0.25 \text{ g}$$

and at least one trim solution exists satisfying the remaining constraints. This is done by enumerating solutions for a given throttle grid covering its permitted range and evaluating the constraint functions $\{f_i(\bar{x}, \bar{p}_s, \bar{u})\}$ listed in the text (fig. 15).

These steps produced the principal empirical data on which the schedule was based; that is, the acceptable range at each point in a grid covering a subregion of the design flight regime, $\mathscr{X}_o$, $\mathscr{P}_o$, given by

$$A_N = 1, \quad \bar{p} = \bar{p}_s$$

The flap schedule was selected approximately as the maximum acceptable flap at each point and a schedule, which is a function of only two variables, $F^*(V_E, A_u)$, is produced. Step 3 is repeated at other A_N in a grid $\{A_{N_k}\}$ covering the design range of A_N to determine if the acceptable flight envelope for the schedule can be usefully maximized by either adjusting the

69

schedule or including A_N as an independent variable. Similarly, steps 2 and 3 are repeated over a grid $\{p_m\}$ covering $\mathscr{P}_o$ to determine if $\bar{p}$ should be an independent variable in the flap schedule.

Optimum Nozzle Schedule

The optimum nozzle schedule was determined empirically by calculating the range of acceptable nozzle values at each flight condition and at the scheduled flap setting for that flight condition, and then selecting the value with the maximum fixed-nozzle regulator control margin $CM_{\delta_f,\nu}(\bar{x}, \bar{p})$. An optimized throttle schedule for maximum fixed-throttle control margin, $CM_{\delta_f,\delta_t}(\bar{x}, \bar{p})$ can be calculated analogously. The required computational steps are described below; they utilize the previously defined trim solution and control margin algorithms (appendix B), the constraint list from the text (fig. 15), and the flap schedule, $F^*(V_E, A_u)$.

1. Define grids $\{V_{E_i}\}$, $\{A_{u_j}\}$, $\{A_{N_k}\}$ and $\{\nu_n\}$ which cover the design ranges for V_E, A_u, A_N and ν in $\mathscr{X}_o$, $\mathscr{U}_o$.

2. Generate and store fixed-nozzle acceleration envelopes for these grids

$$\left\{ \mathscr{A}_{\delta_{f_{i,j}}, \nu_n}\left(V_{E_i}, \bar{p}_s\right) \right\}$$

where the standard parameter values $\bar{p}_s$ are used and $\delta_{f_{i,j}}$ is taken from the the flap schedule, $\delta_{f_{i,j}} = F^*(V_{E_i}, A_{u_j})$.

3. For each value of $\bar{x}$ in the grid, calculate the trim solutions corresponding to $\{\nu_n\}$, and the corresponding values of the constraint parameters $\{f_i(\bar{x}, \bar{p}_s, \bar{u}\}$ and control margin, $CM_{\delta_f,\nu}(\bar{x}, \bar{p}_s)$. These data give the range of nozzle settings for which trim solutions exist, the subset of this range for which they are acceptable, and the acceptable nozzle angle having maximum control margin, ν^*.

These steps produced the empirical data from which the schedule, $\nu^*(x)$, given in the text was defined. These data are all taken at the standard parameter values $\bar{p}_s$, but steps 2 and 3 can be repeated over a grid $\{\bar{p}_m\}$ covering $\mathscr{P}_o$ to determine if the acceptable flight envelope of the schedule can be usefully maximized by including $\bar{p}$ as an independent variable in the flap schedule.

The effects of off-nominal parameter values on the flight envelope boundaries are significant since the STOL approach attempts to exploit the margins of the acceptable flight envelope, particularly

$$V_{E_{min}}(\bar{p}), \quad A_{u_{min}}(\bar{p})$$

However, a study of these effects and the possibilities for maximizing the acceptable envelope for the designed schedule by including the parameters as independent variables was outside the scope of the present effort.

APPENDIX D

ATTITUDE AND ATTITUDE RATE COMMANDS AND STABILITY AXIS

SPECIFIC FORCE COMMANDS

The attitude and attitude rate commands associated with the execution of the acceleration commands and the nominal path are calculated in the trim map as indicated in figure 25. The Euler angle attitude commands, (Φ, Θ, Ψ) and body axis rate commands (p, q, r) can be calculated from the values of the angles $\{\alpha, \beta, \Phi_V, \gamma, \Psi_V\}$ and their rates for the nominal path and acceleration commands, as derived in this appendix. In addition, the Trimmap requires the transformation of the input acceleration commands to stability axis components of the applied specific force. This transformation was given in the text (eqs. (5)-(7)) assuming zero steady-state sideslip angle. A more general formulation for the case of nonzero sideslip is derived in this appendix.

Attitude Commands

The notation T_{AB} will denote the transformation of vectors referred to axes A into vectors referred to axes B. The axes of interest here are inertial or runway (r), path (p), stability (s), and body (b).

The attitude of the aircraft body axes with respect to inertial axes is given by the standard Euler angles, Φ, Θ, Ψ, measured by gyros on the aircraft. The corresponding transformation is (ref. 10)

$$T_{br} \equiv \begin{bmatrix} \cos\Theta\cos\Psi & \cos\Theta\sin\Psi & -\sin\Theta \\ \sin\Phi\sin\Theta\cos\Psi - \cos\Phi\sin\Psi & \sin\Phi\sin\Theta\sin\Psi + \cos\Phi\cos\Psi & \sin\Phi\cos\Theta \\ \cos\Phi\sin\Theta\cos\Psi + \sin\Phi\sin\Psi & \cos\Phi\sin\Theta\sin\Psi - \sin\Phi\cos\Theta & \cos\Phi\cos\Theta \end{bmatrix}$$

$$(D1)$$

This can also be expressed in the form of a sequence of rotations about a single axis (ref. 10)

$$T_{br} = L_1(\Phi)L_2(\Theta)L_3(\Psi) \tag{D2}$$

where the subscript indicates the axis about which the rotation occurs

71

$$L_1(x) \equiv \begin{bmatrix} 1 & 0 & 0 \\ 0 & \cos x & \sin x \\ 0 & -\sin x & \cos x \end{bmatrix}$$

$$L_2(x) \equiv \begin{bmatrix} \cos x & 0 & -\sin x \\ 0 & 1 & 0 \\ \sin x & 0 & \cos x \end{bmatrix}$$

$$L_3(x) \equiv \begin{bmatrix} \cos x & \sin x & 0 \\ -\sin x & \cos x & 0 \\ 0 & 0 & 1 \end{bmatrix}$$

Expressions for the Euler angles can be given in terms of the angles $\{\alpha,\ \beta,\ \Phi_V,\ \Psi_V,\ \gamma\}$ by equating equal transformations between inertial and body axes

$$T_{br} = T_{bs} T_{sp} T_{pr} \tag{D3}$$

The transformation to path axes is defined from the air velocity vector $\bar{V}_A$ using equation (6) of the text

$$T_{pr} = L_2(\gamma) L_3(\Psi_V) \tag{D4}$$

The transformation from stability axes to body axes is simply

$$T_{bs} = L_2(\alpha) \tag{D5}$$

The remaining transformation from stability to path axes is defined with the aid of sketch (e). The path axes $\{\underline{u},\ \bar{m},\ \bar{n}\}$ are along the air velocity vector ($\underline{u}$) and normal to it with $\bar{m}$ and $\bar{n}$ in the horizontal and vertical planes, respectively. The stability axes $\{\bar{i}_s,\ \bar{j}_s,\ \bar{k}_s\}$ are, respectively, along the projection of $\bar{V}_A$ in the body plane of symmetry ($\bar{i}_b,\ \bar{j}_b$), along the body wing
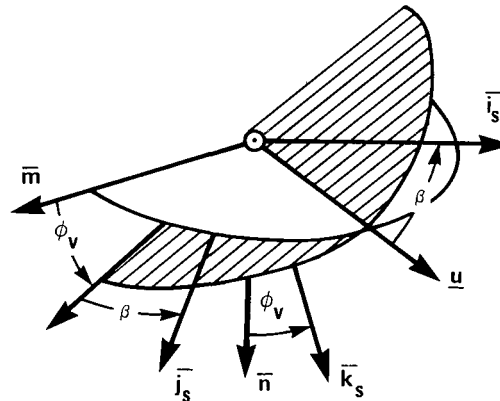
Sketch (e).- Stability and path axes.

axis $\bar{j}_b$, and in the plane of symmetry normal to $\bar{i}_s$. The stability axes are obtained from path axes by first rotating about the air velocity vector direction $\underline{u}$, through the angle Φ_v, and then about the $\bar{k}_s$ axis through the sideslip angle β, in a left-handed direction.

$$T_{sp} = L_3(-\beta)L_1(\Phi_v) \tag{D6}$$

The transformation identity in (D3) can now be given as

$$L_1(\Phi)L_2(\Theta)L_3(\Psi) = L_2(\alpha)L_3^T(\beta)L_1(\Phi_v)L_2(\gamma)L_3(\Psi_V) \tag{D7}$$

The attitude commands can therefore be calculated from the remaining five angles. In the Trimmap, α_c is obtained from the trim solution algorithm, β_c is usually taken as zero but can be nonzero in the case of decrabbed flight so is retained here for generality, Φ_{vc} is one of the cylindrical coordinates of the total acceleration command, and (γ, Ψ_V) are given by the commanded air velocity vector, $\overline{VAC}$.

To derive formulas for the Euler angles, represent the elements of the matrix on the right-hand side of equation (D7) as $[a_{ij}]$ and then, using equation (D1) obtain

$$\Theta = \sin^{-1}(-a_{13}) \qquad -\frac{\pi}{2} < \Theta < \frac{\pi}{2}$$

$$\Psi = \tan^{-1}\left(\frac{a_{12}}{a_{11}}\right) \qquad -\pi \leqslant \Psi < \pi \tag{D8}$$

$$\Phi = \tan^{-1}\left(\frac{a_{23}}{a_{33}}\right)$$

or, for computational convenience

$$\Phi = \sin^{-1}\frac{a_{23}}{\cos \Theta}$$

The required terms for the calculation of the Euler angles are

$$a_{13} = -\cos \alpha[\cos \beta \sin \gamma + \sin \beta \sin \phi_v \cos \gamma] - \sin \alpha \cos \phi_v \cos \gamma$$

$$a_{23} = -\sin \beta \sin \gamma + \cos \beta \sin \phi_v \cos \gamma$$

$$a_{33} = -\sin \alpha(\cos \beta \sin \gamma + \sin \beta \sin \phi_v \cos \gamma) + \cos \alpha \cos \phi_v \cos \gamma$$

$$a_{11} = \sin \Psi_v[\cos \alpha \sin \beta \cos \phi_v - \sin \alpha \sin \phi_v]$$
$$\qquad + \cos \Psi_v[\cos \alpha(\cos \beta \cos \gamma - \sin \beta \sin \phi_v \sin \gamma) - \sin \alpha \cos \phi_v \sin \gamma]$$

$$a_{12} = \sin \Psi_v[\cos \alpha(\cos \beta \cos \gamma - \sin \beta \sin \phi_v \sin \gamma) - \sin \alpha \cos \phi_v \sin \gamma]$$
$$\qquad + \cos \Psi_v[-\cos \alpha \sin \beta \cos \phi_v + \sin \alpha \sin \phi_v]$$

$$\tag{D9}$$

73

The heading angle expression can be simplified by denoting the coefficients of $\sin \Psi_V$, $\cos \Psi_V$ in a_{12} as A, B and then we have

$$\left. \begin{array}{l} a_{12} = A \sin \Psi_V + B \cos \Psi_V \\[8pt] a_{11} = B \cos \Psi_V - A \sin \Psi_V \\[8pt] \Psi = \Psi_V + \tan^{-1} \dfrac{B}{A} \end{array} \right\} \qquad (D10)$$

For passenger operations in STOL aircraft, the angles α, β, γ, Θ can be taken as small angles and second and higher-order terms (H.O.T.'s) in these angles can be neglected to obtain the approximation

$$\left. \begin{array}{l} \Theta = \gamma + \alpha \cos \Phi_V + \beta \sin \Phi_V + \text{H.O.T.'s} \\[8pt] \Phi = \Phi_V + \text{H.O.T.'s} \\[8pt] \Psi = \Psi_V + \alpha \sin \Phi_V - \beta \cos \Phi_V + \text{H.O.T.'s} \end{array} \right\} \qquad (D11)$$

Attitude Rate Commands

The body axis attitude commands are calculated from the five independent angles, $\{\alpha,\ \beta,\ \Phi_V,\ \gamma,\ \Psi_V\}$, and therefore the body rate commands can be constructed from the angular rates of these angles and oriented along their appropriate axes about which the rotation occurs; that is, from the vector identity

$$\bar{\omega} = \dot{\alpha}\bar{j}_b + \dot{\beta}\bar{k}_s + \dot{\phi}_V\underline{u} + \dot{\gamma}\bar{m} + \dot{\Psi}_V\bar{k}_r \qquad (D12)$$

All vectors are unit vectors from one or another of the axis frames previously defined, and all can be transformed to body axes using equations (D4)-(D6); that is, the body axis rate commands are

$$(\omega)_b = \dot{\alpha}\begin{pmatrix} 0 \\ 1 \\ 0 \end{pmatrix} + \dot{\beta} T_{bs}\begin{pmatrix} 0 \\ 0 \\ 1 \end{pmatrix} + T_{bs}T_{sp}\left[\begin{pmatrix} 1 \\ 0 \\ 0 \end{pmatrix}\dot{\phi}_V + \begin{pmatrix} 0 \\ 1 \\ 0 \end{pmatrix}\dot{\gamma}\right] + \dot{\Psi}_V T_{br}\begin{pmatrix} 0 \\ 0 \\ 1 \end{pmatrix} \qquad (D13)$$

or

$$(\omega)_b = \begin{pmatrix} 0 \\ 1 \\ 0 \end{pmatrix}\dot{\alpha} + \begin{pmatrix} -\sin \alpha \\ 0 \\ \cos \alpha \end{pmatrix}\dot{\beta} + \begin{pmatrix} \cos \alpha \cos \beta \\ \sin \beta \\ \sin \alpha \cos \beta \end{pmatrix}\dot{\phi}_V \pm \begin{pmatrix} \sin \alpha \sin \phi_V - \cos \alpha \sin \beta \cos \phi_V \\ \cos \beta \cos \phi_V \\ -\cos \alpha \sin \phi_V - \sin \alpha \sin \beta \cos \phi_V \end{pmatrix}\dot{\gamma}$$

$$+ \begin{pmatrix} -\cos \alpha[\sin \gamma \cos \beta + \sin \beta \sin \phi_V \cos \gamma] - \sin \alpha \cos \phi_V \cos \gamma \\ -\sin \gamma \sin \beta + \cos \beta \sin \phi_V \cos \gamma \\ -\sin \alpha[\sin \gamma \cos \beta + \sin \beta \sin \phi_V \cos \gamma] + \cos \alpha \cos \phi_V \cos \gamma \end{pmatrix}\dot{\Psi}_V$$

The small angle approximation is obtained by neglecting terms which are second or higher in γ, α, β, $\dot{\alpha}$, $\dot{\beta}$, $\dot{\Phi}_V$, $\dot{\gamma}$, $\dot{\Psi}_V$

$$(\omega)_b = \begin{pmatrix} 0 \\ 1 \\ 0 \end{pmatrix} \dot{\alpha} + \begin{pmatrix} 0 \\ 0 \\ 1 \end{pmatrix} \dot{\beta} + \begin{pmatrix} 1 \\ 0 \\ 0 \end{pmatrix} \dot{\Phi}_V + \begin{pmatrix} 0 \\ \cos \Phi_V \\ -\sin \Phi_V \end{pmatrix} \dot{\gamma} + \begin{pmatrix} 0 \\ \sin \Phi_V \\ \cos \Phi_V \end{pmatrix} \dot{\Psi}_V + \text{H.O.T.'s} \qquad \text{(D14)}$$

The angular rates for $\dot{\Phi}_V$, $\dot{\gamma}$, $\dot{\Psi}_V$ can be generated from the nominal acceleration commands, using equations (5) and (7) of the text

$$\left.\begin{aligned} \dot{\gamma}_c &= \frac{-\overline{ac} \cdot \overline{n}}{V} \\[2mm] \dot{\Psi}_{vc} &= \frac{\overline{ac} \cdot \overline{m}}{V \cos \gamma} \\[2mm] \dot{\Phi}_{vc} &\simeq \frac{\cos^2 \Phi_V}{g \cos \gamma - \overline{ac} \cdot \overline{n}} \frac{d}{dt} (\overline{ac} \cdot \overline{m}) + \text{H.O.T.'s} \end{aligned}\right\} \qquad \text{(D15)}$$

Of these angular rates $\dot{\Psi}_V$ has a steady value during turns (of the order of 3 to 5 deg/sec), varies transiently at turn entry and exit and is zero otherwise, and appears in both q, r. The flight-path angle rate $\dot{\gamma}$ occurs transiently in relatively short duration flares and pitchovers and affects q principally. The roll rate, $\dot{\Phi}_V$, occurs only transiently at turn entry and exit. It is calculated from the lateral jerk, which is available from the command generator as a result of its transition maneuver command generation calculations. Of the remaining rates in equation (D14), $\dot{\beta}_c(t)$ can be assumed zero almost everywhere, and $\dot{\alpha}_c$ can be constructed as the derivative of the output of the trim solution algorithm. However, for the nominal path, α and γ transients are associated but the α transient usually has a higher frequency and is less significant as a rate command for following the nominal maneuver.

Stability Axis Specific Force Commands

The inputs to the basic Trimmap are the stability axis components of the applied specific force commands. This applied specific force command, referenced to path axes, is readily computed from the commanded acceleration $\overline{ac}$ and air velocity vector $\overline{VAC}$, using equations (3) and (6) from the text

$$\begin{pmatrix} A_u \\ A_m \\ A_n \end{pmatrix} = \begin{pmatrix} \overline{ac} \cdot \underline{u} \\ \overline{ac} \cdot \overline{m} \\ \overline{ac} \cdot \overline{n} \end{pmatrix} - g \begin{pmatrix} -\sin \gamma \\ 0 \\ \cos \gamma \end{pmatrix} \qquad \text{(D16)}$$

This is transformed to stability axis components using (D6)

$$\begin{pmatrix} A_x \\ A_y \\ A_z \end{pmatrix} = E_3(-\beta)E_1(\Phi_v) \begin{pmatrix} A_u \\ A_m \\ A_n \end{pmatrix} = \begin{bmatrix} \cos\beta & -\sin\beta\cos\Phi_v & -\sin\beta\sin\Phi_v \\ \sin\beta & \cos\beta\cos\Phi_v & \cos\beta\sin\Phi_v \\ 0 & -\sin\Phi_v & \cos\Phi_v \end{bmatrix} \begin{pmatrix} A_u \\ A_m \\ A_n \end{pmatrix} \quad (D17)$$

These three equations contain five unknowns: β, Φ_v, A_x, A_y, A_z. Normally, it is assumed that β, A_y are zero after which A_x, A_z, Φ_v can be solved with the same result previously given by equation (7). More generally, the steady-state value of β_c need not be zero, as in decrabbed flight in the presence of lateral winds, and can be assumed given independently of the trajectory command. The value of A_y in this case is not arbitrary but follows from β_c and the directional equilibrium of the aircraft; in steady state, β generates both lateral acceleration (proportional to $C_{y\beta}\beta$) and yawing moment ($C_{n\beta}\beta$) which is balanced by additional lateral force from the rudder. The resulting lateral acceleration in steady state is then

$$A_y = \frac{QS_w}{m}\left(C_{y\beta} - C_{n\beta}\frac{b}{\ell_v}\right)\beta_c \quad (D18)$$

where b, ℓ_v are, respectively, the wingspan and the moment arm of the rudder center of pressure about the aircraft center of gravity. Consequently, equation (D17) can now be solved for A_x, A_z, Φ_v assuming that A_u, A_m, A_n and β_c are given and that A_y is computed from β_c. The solution is

$$\left. \begin{aligned} A_x &= \frac{A_u - \sin\beta_c A_y}{\cos\beta_c} \\[2mm] A_z &= -\sqrt{A_m^2 + A_n^2 - A_y^{*2}} \\[2mm] \Phi_v &= \tan^{-1}\left(\frac{A_m}{-A_n}\right) + \Sigma \end{aligned} \right\} \quad (D19)$$

where

$$A_y^* = \frac{A_y - \sin\beta_c A_u}{\cos\beta_c}$$

$$\Sigma = \sin^{-1}\frac{A_y^*}{\sqrt{A_m^2 + A_n^2}}$$

Equations (D16), (D18), and (D19) comprise the map of the applied specific force commands to stability axes used in the Trimmap of figure 25.

REFERENCES

1. Meyer, George; and Cicolani, Luigi S.: A Formal Structure for Advanced Automatic Flight Control Systems. NASA TN D-7940, 1975.

2. Cicolani, Luigi S.; and Weissenberger, Stein: A Nonlinear Trajectory Command Generator for a Digital Flight Control System. NASA TP-1221, 1978.

3. Benner, Margaret S.; McLaughlin, Milton; Sawyer, Richard H.; Van Gunst, Roser; and Ryan, John J.: A Flight Investigation with a STOL Airplane Flying Curved Descending Instrument Approach Paths. NASA TN D-7669, 1974.

4. Cleveland, William B.; Vomaske, Richard F.; and Sinclair, S. R. M.: Augmentor Wing Jet STOL Research Aircraft Digital Simulation Model. NASA TN X-62,149, 1972.

5. Whittley, D. C.; and Cook, W. L.: Comparison of Model and Flight Test Data for an Augmentor-Wing STOL Research Aircraft. AGARD Conf. Proc. No. 187, Flight Ground Testing Facilities Correlation, June 1975, p. 17-1.

6. Grossmith, S. W.: Augmentor Wing Jet STOL Research Aircraft Update and Powered-Lift Vehicle Certification Standards. Canadian Aeronaut. Space J., vol. 21, no. 7, Sept. 1975, pp. 254-261.

7. Scott, B. C.; Martin, P. W.; Hynes, C. S.; and Bryder, R. B.: Progress Toward Development of Civil Airworthiness Criteria for Powered-Lift Aircraft. NASA TM X-73,124, 1976.

8. Heffley, Robert K.; Stapelford, Robert L.; and Rumold, Robert C.: Airworthiness Criteria Development for Powered-Lift Aircraft. NASA CR-2791, FAA-RD-76-195, 1977.

9. Cicolani, L. S.; and Meyer, G.: Digital Simulation of V/STOL Aircraft for Autopilot Research. Large-Scale Dynamic Systems, NASA SP-371, 1975.

10. Etkin, Bernard: Dynamics of Atmospheric Flight. John Wiley & Sons, Inc., New York, 1972.

11. Pecsvaradi, Thomas: Four-Dimensional Guidance Algorithms for Aircraft in an Air Traffic Environment. NASA TN D-7829, 1975.

12. Lee, Homer Q.; Neuman, Frank; and Hardy, Gordon H.: 4-D Area Navigation System Description and Flight Test Results. NASA TN D-7874, 1975.

13. Murrey, W., ed.: Numerical Methods for Unconstrained Optimization. Academic Press, London and New York, 1972.

14. Powell, M. D. D.: A Fortran Subroutine for Solving Systems of Nonlinear Algebraic Equations. AERE-R,5947, AERE, Harwell, Berks, UK, Nov. 1968.

15. Apostol, Tom M.: Mathematical Analysis. Addison-Wesley, Reading, Mass., 1957.

TABLE 1.– TABULATED AWJSRA ENGINE MODEL – ONE ENGINE, CORRECTED HOT THRUST, COLD THRUST, INLET MASS FLOW AND FUEL FLOW AND THROTTLE – POWER RELATION

$N_H/\sqrt{\tau}$ \ V_A Knots	0	53.6	84.0	89.5	92.5	95.0	98.0	103.515	Tabulated parameter
0	0	380	4552	10,688	16,521	21,506	26,098	31,198	
60	0	509	4858	10,928	16,740	21,692	26,256	31,325	$\dfrac{T_H}{\delta} \sim N$
250	0	2473	9350	14,368	19,911	24,309	28,518	33,125	
0	0	363	3444	7385	11,096	13,246	14,684	15,712	
60	0	378	3486	7414	11,074	13,142	14,632	15,809	$\dfrac{T_c}{\delta} \sim N$
250	0	596	4068	8039	11,870	13,836	15,315	16,380	
	0	19.8	36.7	58.4	72.4	80.4	86.6	94.7	$\dot{m}_E \dfrac{\sqrt{\tau}}{\delta} \sim kg/sec$
	0	551.6	864.7	1401.0	2206.9	2452.7	2965.0	3782.9	$\dfrac{\dot{m}_E}{\delta\sqrt{\tau}} \sim kg/hr$

Note: Throttle-power relation:

$$\delta_T = \max(0.0618\,N_H,\ 1.3866\,N_H - 107.17)$$

79

TABLE 2.- AWJSRA DRAG AND LIFT COEFFICIENTS

(a) C_D

α / C_J	-10.5	-6.5	-2.5	1.5	5.5	9.5	13.5	17.5	19.5	27.5
Flap = 5.6										
0	0.092	0.068	0.073	0.095	0.136	0.188	0.261	0.375	0.443	0.811
.2	-.111	-.135	-.124	-.105	-.062	-.005	.070	.200	.269	.648
.4	-.313	-.335	-.324	-.299	-.256	-.198	-.117	.018	.092	.484
.6	-.510	-.532	-.520	-.495	-.446	-.378	-.297	-.161	-.087	.321
.8	-.708	-.730	-.718	-.688	-.638	-.570	-.478	-.337	-.257	.146
1.2	-1.101	-1.127	-1.116	-1.078	-1.023	-.949	-.846	-.690	-.610	-.184
2.0	-1.883	-1.905	-1.901	-1.850	-1.780	-1.674	-1.562	-1.394	-1.304	-.847
Flap = 30.0										
0	0.040	0.110	0.160	0.220	0.270	0.330	0.370	0.410	0.430	0.500
.2	-.240	-.150	-.070	.020	.110	.190	.270	.340	.380	.510
.4	-.480	-.370	-.270	-.160	-.060	.040	.140	.240	.290	.480
.6	-.700	-.580	-.470	-.350	-.230	-.110	.000	.120	.170	.390
.8	-.900	-.780	-.660	-.530	-.400	-.270	-.140	-.010	.050	.300
1.2	-1.260	-1.155	-1.025	-.870	-.720	-.560	-.405	-.250	-.175	.140
2.0	-1.800	-1.690	-1.540	-1.370	-1.180	-.990	-.800	-.620	-.520	-.140
Flap = 50.0										
0	0.300	0.300	0.315	0.330	0.370	0.400	0.440	0.470	0.485	0.550
.2	.080	.130	.180	.240	.305	.375	.455	.540	.580	.750
.4	-.100	-.020	.065	.160	.260	.375	.500	.620	.680	.930
.6	-.255	-.155	-.050	.080	.220	.375	.520	.670	.740	1.050
.8	-.380	-.280	-.160	-.015	.150	.325	.515	.710	.820	1.260
1.2	-.665	-.550	-.415	-.250	-.050	.178	.435	.700	.840	1.402
2.0	-1.250	-1.110	-.925	-.720	-.480	-.200	.100	.440	.610	1.320
Flap = 65.0										
0	0.300	0.300	0.320	0.340	0.370	0.410	0.450	0.500	0.520	0.620
.2	.200	.240	.270	.320	.380	.460	.540	.620	.660	.860
.4	.130	.170	.230	.320	.430	.540	.660	.800	.860	1.120
.6	.040	.110	.220	.330	.480	.640	.810	.970	1.050	1.380
.8	-.050	.050	.180	.340	.510	.700	.890	1.100	1.200	1.660
1.2	-.220	-.110	.040	.215	.425	.655	.890	1.150	1.285	1.925
2.0	-.640	-.490	-.290	-.060	.200	.470	.760	1.070	1.240	2.140
Flap = 72.0										
0	0.290	0.300	0.320	0.335	0.350	0.380	0.420	0.455	0.480	0.575
.2	.240	.265	.300	.340	.400	.470	.545	.630	.670	.845
.4	.195	.245	.305	.380	.475	.590	.715	.825	.875	1.100
.6	.160	.230	.330	.447	.575	.725	.895	1.060	1.140	1.490
.8	.140	.235	.365	.495	.650	.820	1.006	1.215	1.320	1.770
1.2	-.000	.125	.282	.437	.625	.835	1.062	1.317	1.450	2.035
2.0	-.320	-.140	.065	.290	.530	.795	1.080	1.400	1.575	2.315

TABLE 2.- CONCLUDED.

(b) C_L

α C_J	-10.5	-6.5	-2.5	1.5	5.5	9.5	13.5	17.5	19.5	27.5
Flap = 5.6										
0	-0.928	-0.577	-0.207	0.215	0.612	1.004	1.353	1.670	1.748	1.624
.2	-.935	-.563	-.172	.252	.660	1.073	1.444	1.782	1.950	2.040
.4	-.948	-.556	-.163	.308	.720	1.144	1.525	1.874	2.032	2.254
.6	-.965	-.572	-.149	.319	.756	1.212	1.594	1.943	2.120	2.352
.8	-.971	-.577	-.144	.334	.820	1.269	1.651	2.050	2.218	2.462
1.2	-1.052	-.591	-.127	.391	.888	1.364	1.807	2.222	2.405	2.651
2.0	-1.149	-.614	-.079	.481	1.028	1.565	2.078	2.589	2.818	3.055
Flap = 30.0										
0	-0.717	-0.292	0.101	0.474	0.831	1.153	1.446	1.673	1.761	1.598
.2	-.178	.289	.703	1.116	1.522	1.880	2.223	2.512	2.631	2.723
.4	.186	.675	1.139	1.573	2.017	2.395	2.767	3.077	3.216	3.174
.6	.343	.842	1.327	1.793	2.237	2.644	3.027	3.346	3.473	3.236
.8	.430	.950	1.435	1.910	2.367	2.825	3.238	3.575	3.713	3.320
1.2	.560	1.096	1.598	2.102	2.594	3.062	3.525	3.919	4.074	3.562
2.0	.771	1.357	1.915	2.473	2.998	3.520	4.044	4.519	4.719	4.150
Flap = 50.0										
0	-0.118	0.256	0.596	0.946	1.268	1.542	1.795	1.981	2.059	2.112
.2	.464	.893	1.218	1.590	1.914	2.234	2.559	2.830	2.989	3.216
.4	.712	1.143	1.570	1.994	2.367	2.759	3.067	3.389	3.500	3.475
.6	.816	1.321	1.832	2.311	2.733	3.124	3.483	3.788	3.917	3.694
.8	.899	1.417	1.968	2.427	2.902	3.325	3.702	4.047	4.189	3.850
1.2	1.021	1.587	2.120	2.627	3.131	3.572	4.059	4.418	4.568	4.064
2.0	1.430	2.024	2.559	3.095	3.658	4.156	4.632	5.056	5.215	4.631
Flap = 65.0										
0	-0.007	0.330	0.689	1.042	1.344	1.615	1.860	2.034	2.092	2.108
.2	.753	1.163	1.559	1.904	2.248	2.588	2.918	3.200	3.328	3.363
.4	1.194	1.709	2.103	2.492	2.847	3.217	3.545	3.858	3.983	3.874
.6	1.510	2.001	2.451	2.894	3.313	3.711	4.043	4.313	4.426	4.080
.8	1.594	2.137	2.630	3.087	3.532	3.953	4.313	4.611	4.714	4.167
1.2	1.647	2.198	2.715	3.194	3.662	4.116	4.514	4.873	4.966	4.376
2.0	1.815	2.448	2.989	3.509	3.999	4.470	4.897	5.256	5.389	4.719
Flap = 72.0										
0	0.109	0.434	0.788	1.039	1.337	1.542	1.773	1.901	1.993	1.521
.2	.871	1.152	1.498	1.802	2.112	2.429	2.743	2.981	3.136	2.954
.4	1.354	1.687	2.056	2.423	2.795	3.154	3.519	3.798	3.913	3.365
.6	1.721	2.096	2.498	2.874	3.261	3.640	3.975	4.337	4.499	3.498
.8	2.060	2.450	2.832	3.229	3.626	3.988	4.386	4.738	4.840	3.913
1.2	2.452	2.823	3.244	3.644	4.037	4.455	4.849	5.272	5.303	4.359
2.0	3.031	3.435	3.876	4.287	4.738	5.121	5.562	5.996	6.037	5.089

TABLE 3.— AWJSRA ELEVATOR TRIM SETTINGS — DEG

α / C_J	-10.5	-6.5	-2.5	1.5	5.5	9.5	13.5	17.5	19.5	27.5
Flap = 5.6										
0.	17.0	9.6	3.5	-0.6	-3.3	-5.9	-7.9	-9.0	-9.9	-15.0
.2	16.0	8.7	2.7	-1.4	-3.9	-6.4	-8.2	-9.2	-9.4	-12.7
.4	15.1	7.8	1.9	-1.9	-4.4	-6.8	-8.6	-9.5	-9.7	-11.9
.6	13.7	6.5	.7	-2.8	-5.4	-7.4	-9.1	-9.9	-10.0	-12.4
.8	12.6	5.5	-.2	-3.7	-6.0	-8.0	-9.6	-10.2	-10.3	-12.6
1.2	9.8	3.4	-2.1	-5.3	-7.5	-9.5	-10.8	-11.2	-11.2	-13.2
2.0	4.0	-2.3	-7.2	-10.1	-11.9	-13.5	-14.2	-13.8	-13.4	-15.4
Flap = 30.0										
0.	11.2	7.6	3.8	0.2	-2.7	-5.0	-7.2	-10.1	-11.7	-23.3
.2	9.8	6.7	3.3	.1	-2.5	-4.8	-6.4	-8.5	-9.7	-18.7
.4	9.4	6.6	3.5	.6	-1.8	-3.0	-5.2	-6.9	-7.9	-17.7
.6	8.6	5.9	3.0	.5	-1.9	-3.8	-5.0	-6.6	-7.8	-19.1
.8	7.6	5.0	2.2	-.3	-2.4	-3.9	-4.9	-6.5	-7.5	-20.3
1.2	4.9	2.6	.0	-2.4	-4.3	-5.7	-6.3	-7.3	-8.0	-21.1
2.0	-2.3	-4.0	-6.0	-8.0	-9.8	-10.5	-10.6	-10.5	-10.8	-23.3
Flap = 50.0										
0.	11.1	8.2	5.1	2.2	-0.3	-2.6	-4.8	-7.9	-9.5	-18.7
.2	5.9	4.0	1.5	-.9	-3.0	-5.2	-6.6	-8.4	-9.3	-16.4
.4	1.4	-.3	-2.1	-4.0	-5.8	-7.3	-8.3	-9.6	-10.4	-18.9
.6	-2.8	-3.9	-5.0	-6.2	-7.8	-9.3	-9.7	-10.6	-11.5	-20.7
.8	-6.4	-7.1	-8.0	-9.1	-10.3	-11.3	-11.9	-12.4	-13.0	-22.1
1.2	-11.8	-12.1	-12.9	-13.5	-14.7	-14.7	-14.7	-15.1	-15.7	-26.5
2.0	-20.0	-19.7	-20.2	-20.3	-20.0	-20.1	-20.0	-20.0	-20.5	-31.6
Flap = 65.0										
0.	15.5	10.8	6.7	3.0	0.4	-1.1	-2.2	-3.6	-4.2	-9.4
.2	11.7	7.8	4.6	1.4	-.5	-1.4	-2.1	-2.7	-2.8	-7.0
.4	8.0	4.9	1.8	-.6	-2.2	-2.9	-3.6	-3.6	-3.8	-8.8
.6	3.3	1.0	-1.4	-3.0	-3.8	-4.4	-4.5	-4.8	-5.2	-11.9
.8	-.1	-2.1	-3.9	-5.2	-6.2	-6.3	-6.4	-6.6	-7.0	-15.7
1.2	-6.2	-7.9	-9.3	-10.2	-10.9	-11.0	-11.0	-10.8	-11.2	-20.6
2.0	-15.6	-16.4	-17.3	-17.9	-18.2	-18.0	-18.0	-17.6	-17.7	-27.4
Flap = 72.0										
0.	20.4	14.6	9.9	5.8	2.7	0.1	-1.3	-1.6	-0.8	-1.2
.2	17.8	12.5	8.2	4.7	2.3	.8	.3	.1	.8	.2
.4	14.4	9.6	5.7	3.0	1.2	.4	.5	1.0	1.7	-3.0
.6	11.0	6.7	3.3	.8	-.5	-.9	-.7	.6	1.4	-6.8
.8	7.7	4.0	.8	-1.6	-2.6	-2.8	-1.9	-.4	.1	-6.8
1.2	2.9	-.7	-3.3	-5.3	-6.1	-5.9	-4.7	-2.6	-2.5	-9.1
2.0	-5.0	-8.0	-10.0	-11.7	-11.8	-11.5	-9.7	-7.3	-6.9	-12.6
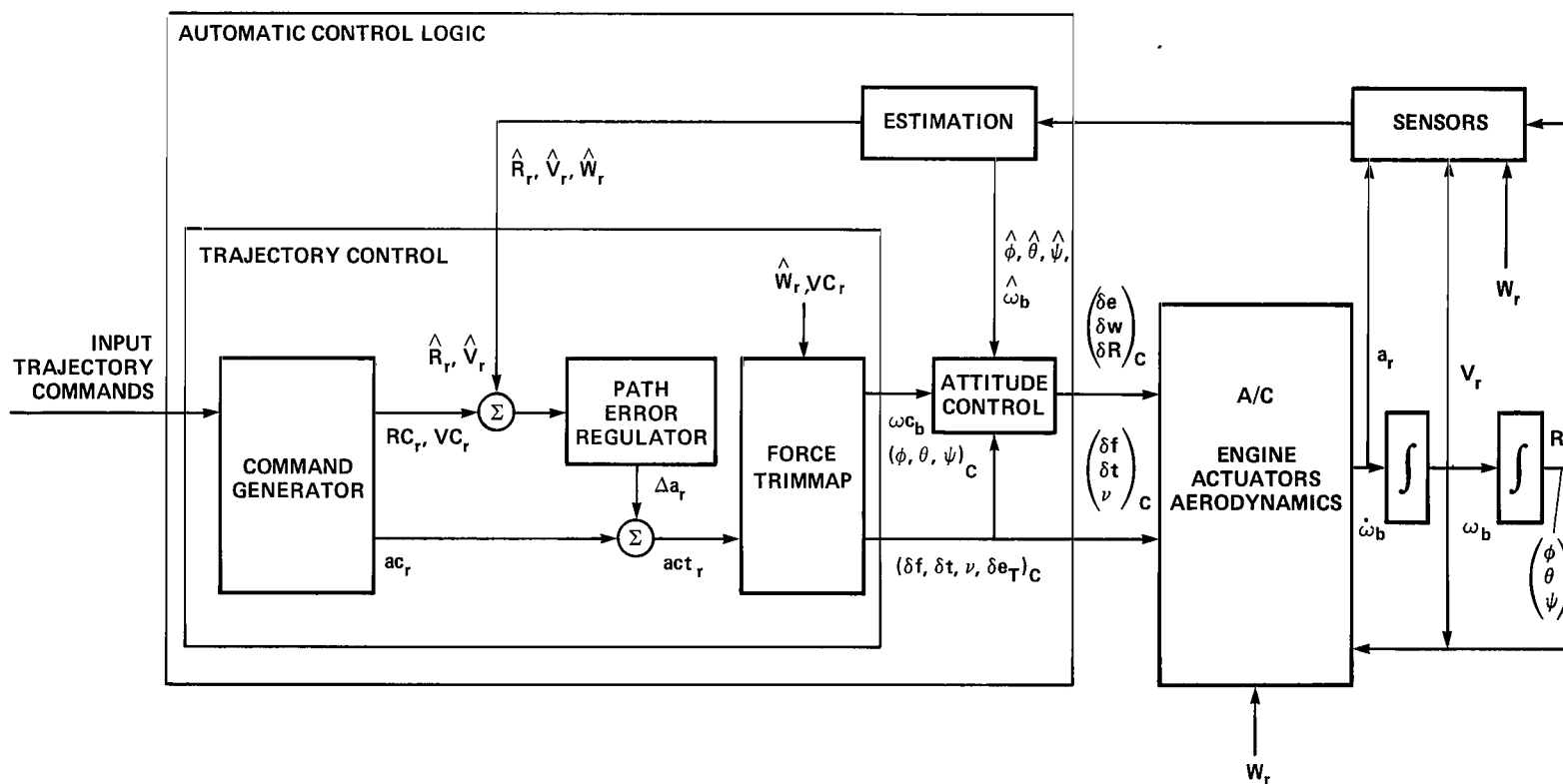
Figure 1.- Automatic control logic - AWJSRA.
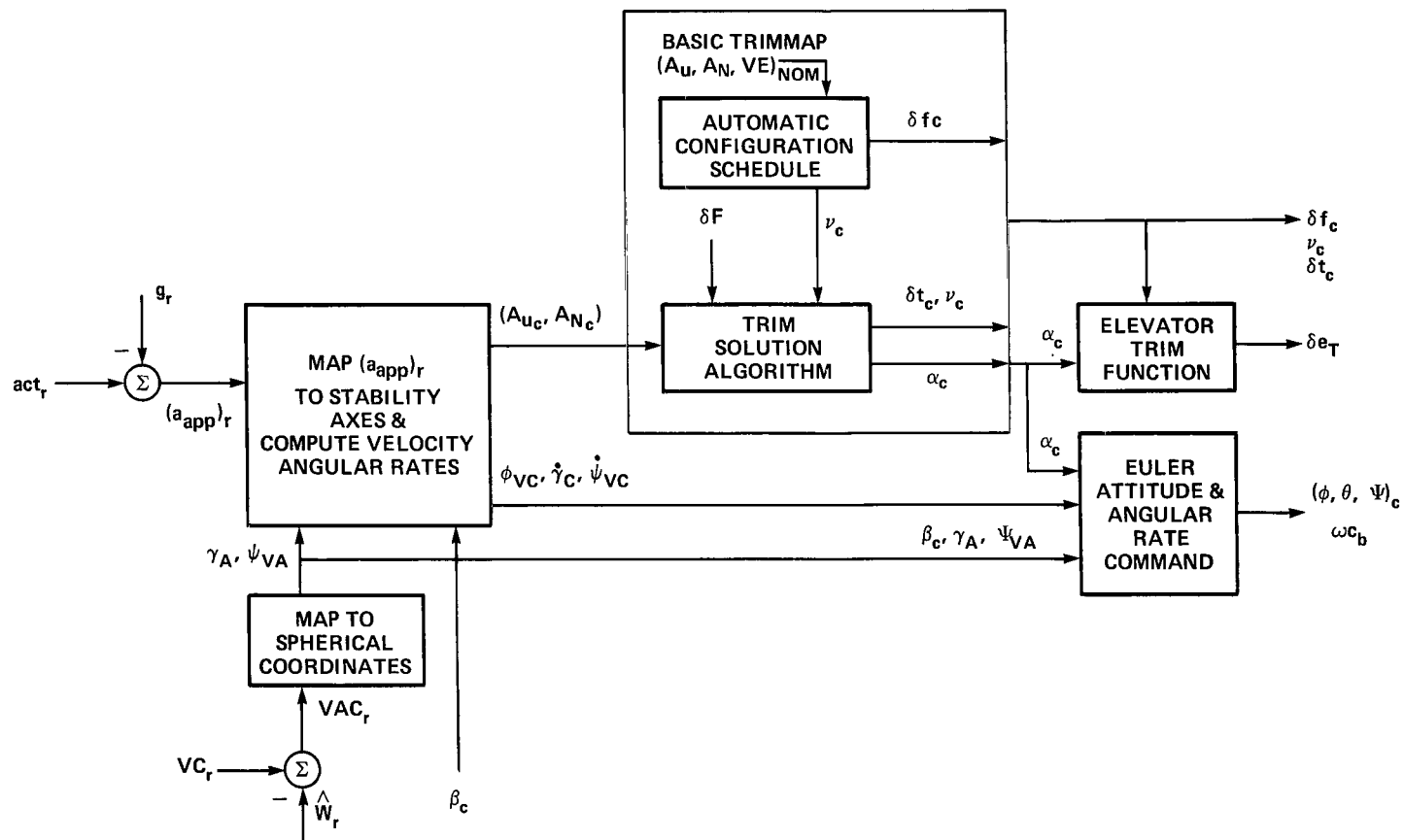
Figure 2.- AWJSRA Force Trimmap.
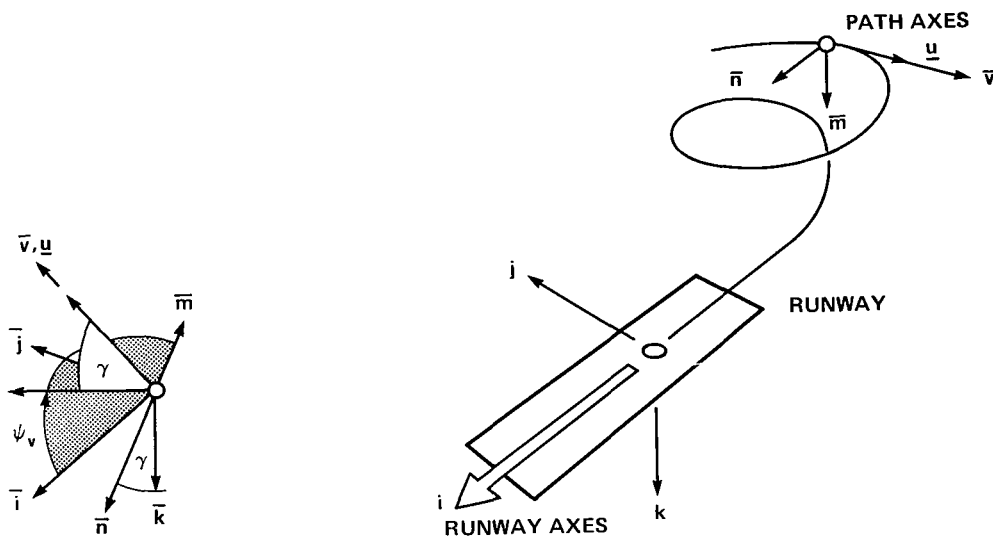
(a) Transformation angles.   (b) Path and runway axes.

Figure 3.- Axis systems and transformation angles.
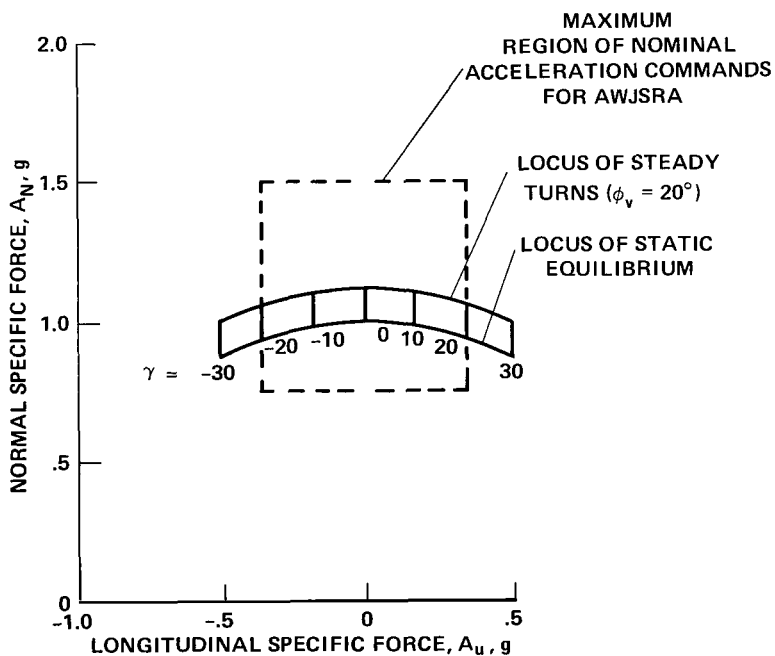
Figure 4.- Applied specific force commands - steady flight conditions.
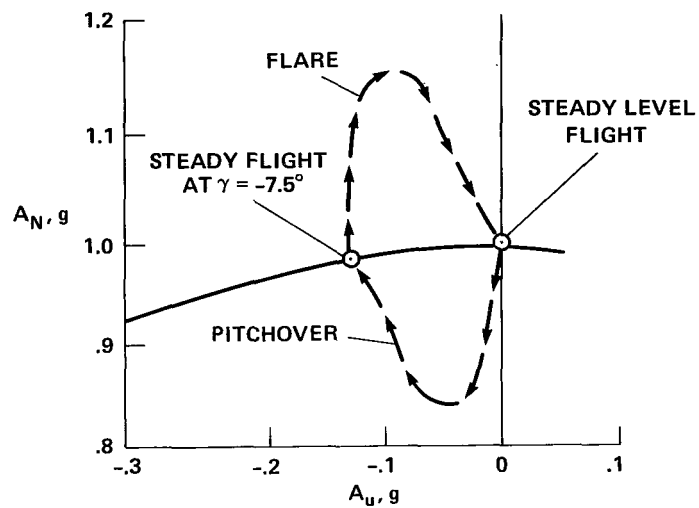
Figure 5.- Applied specific force commands - transient commands for flight-path angle changes.

1. STRAIGHT/LEVEL FLIGHT
2. DESCENDING TURN
3. DECELERATING LEVEL FLIGHT
4-5. LEVEL TURN WITH STEADY WIND
6. DECELERATING GLIDE SLOPE
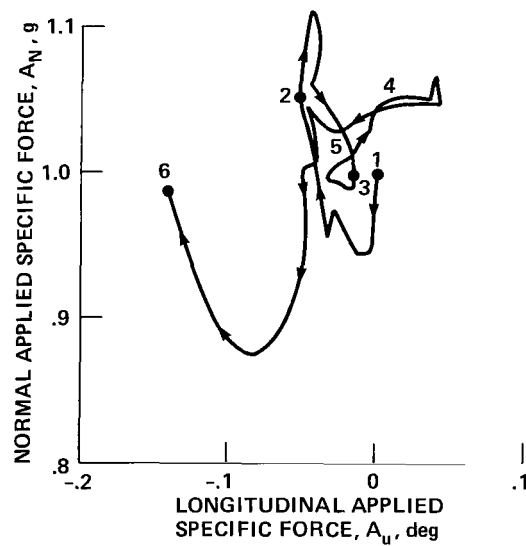
Figure 6.- STOL test approach path: hodograph of applied specific force command.

DUCT AND NOZZLE

WING REAR SPAR

INTAKE

SHROUD

δf

FLAP HINGE POINT

FLAP

CHOKE

DIFFUSER

AUGMENTOR FLAP

T_H

T_H

T_H

ν

ENGINE EXHAUST NOZZLES
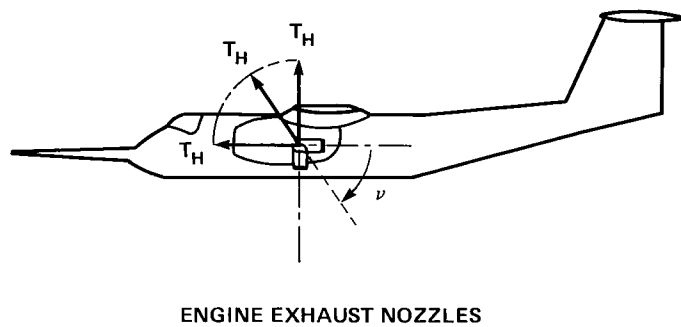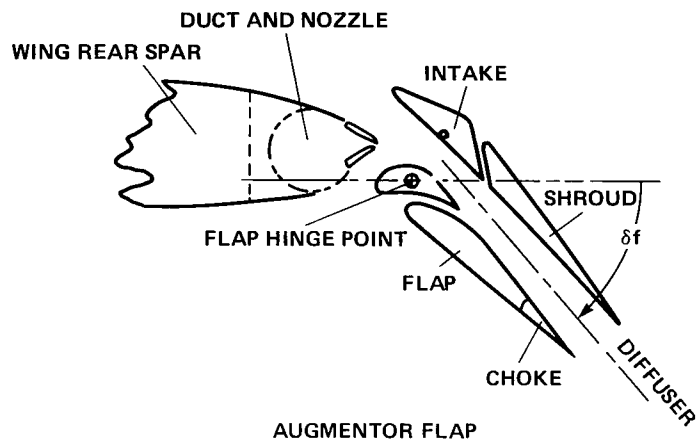
Figure 7.- Augmentor wing jet STOL research aircraft (AWJSRA).
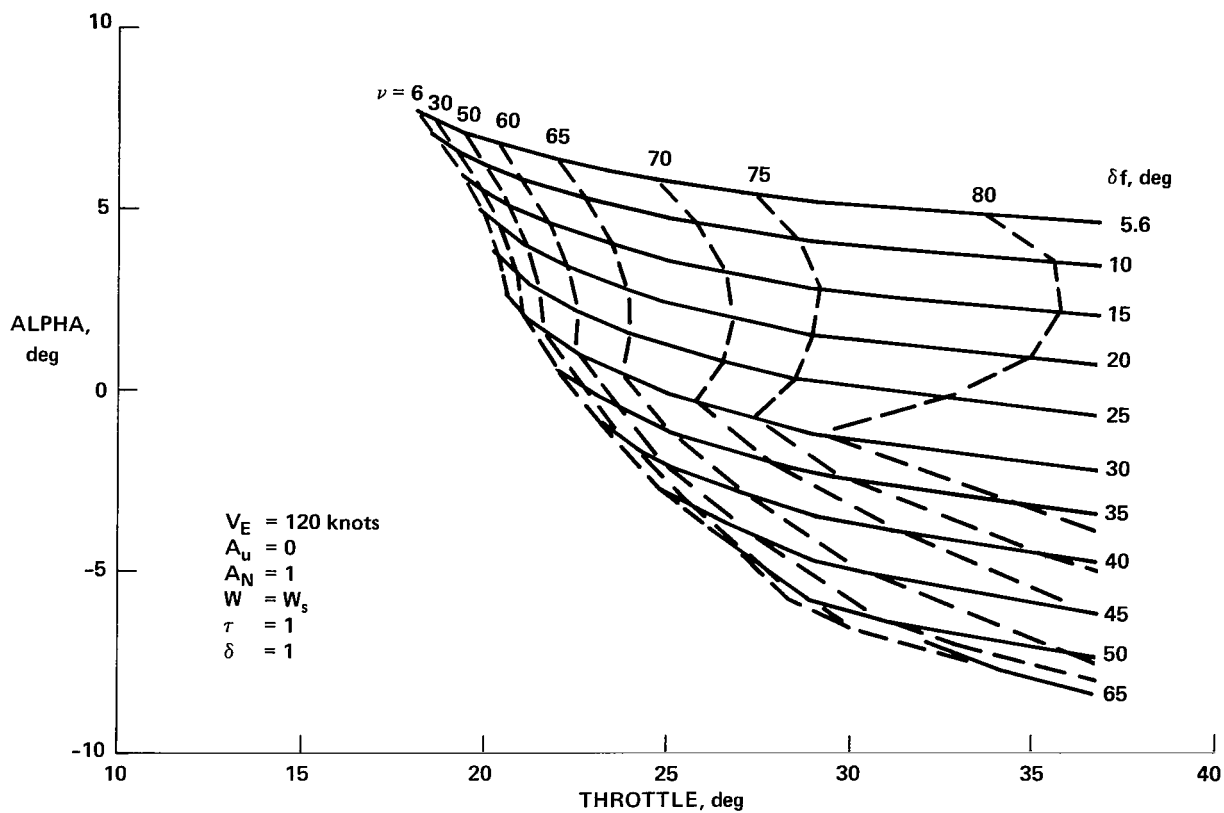
(a) Level flight.

Figure 8.- Trim solutions for AWJSRA.
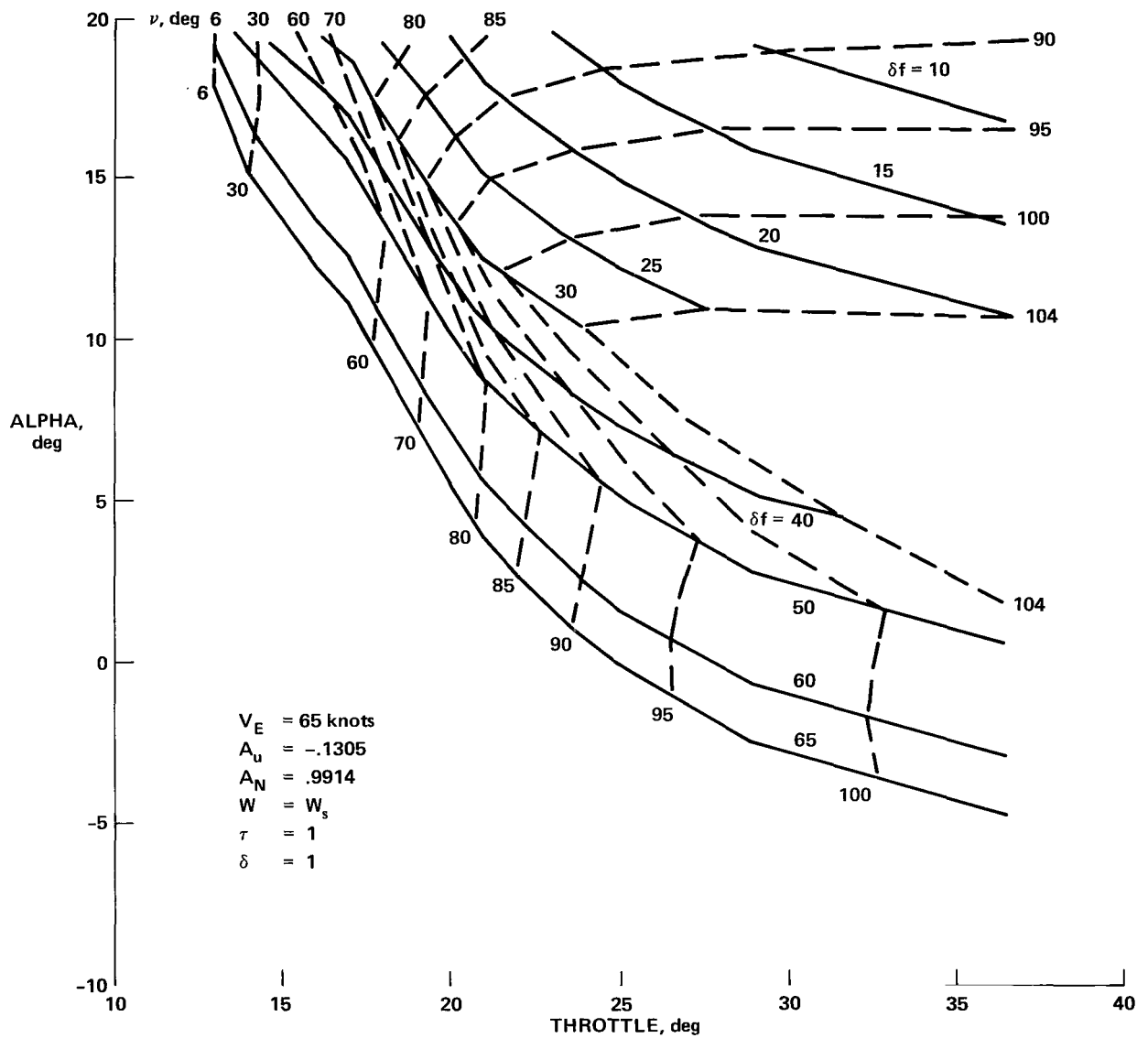
(b) Glide slope.

Figure 8.- Concluded.
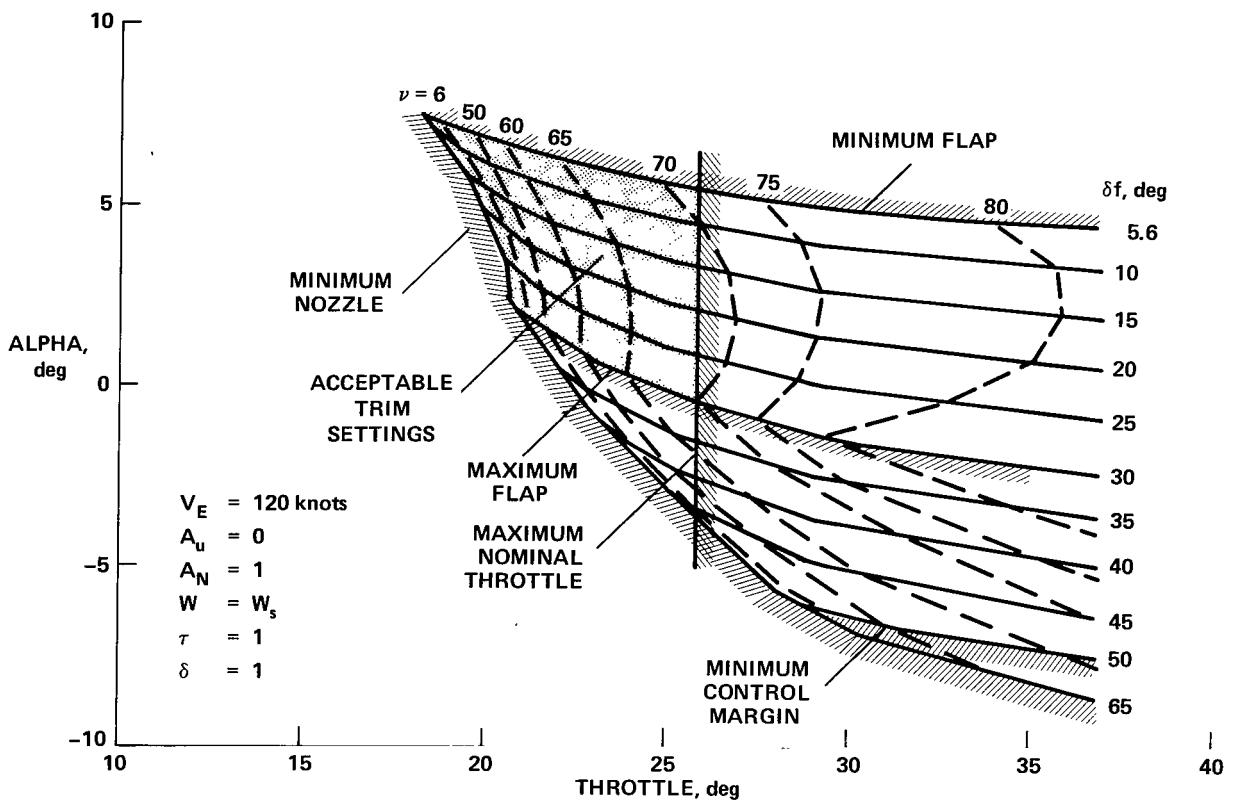
(a) Level flight.

Figure 9.- Acceptable trim settings for AWJSRA.
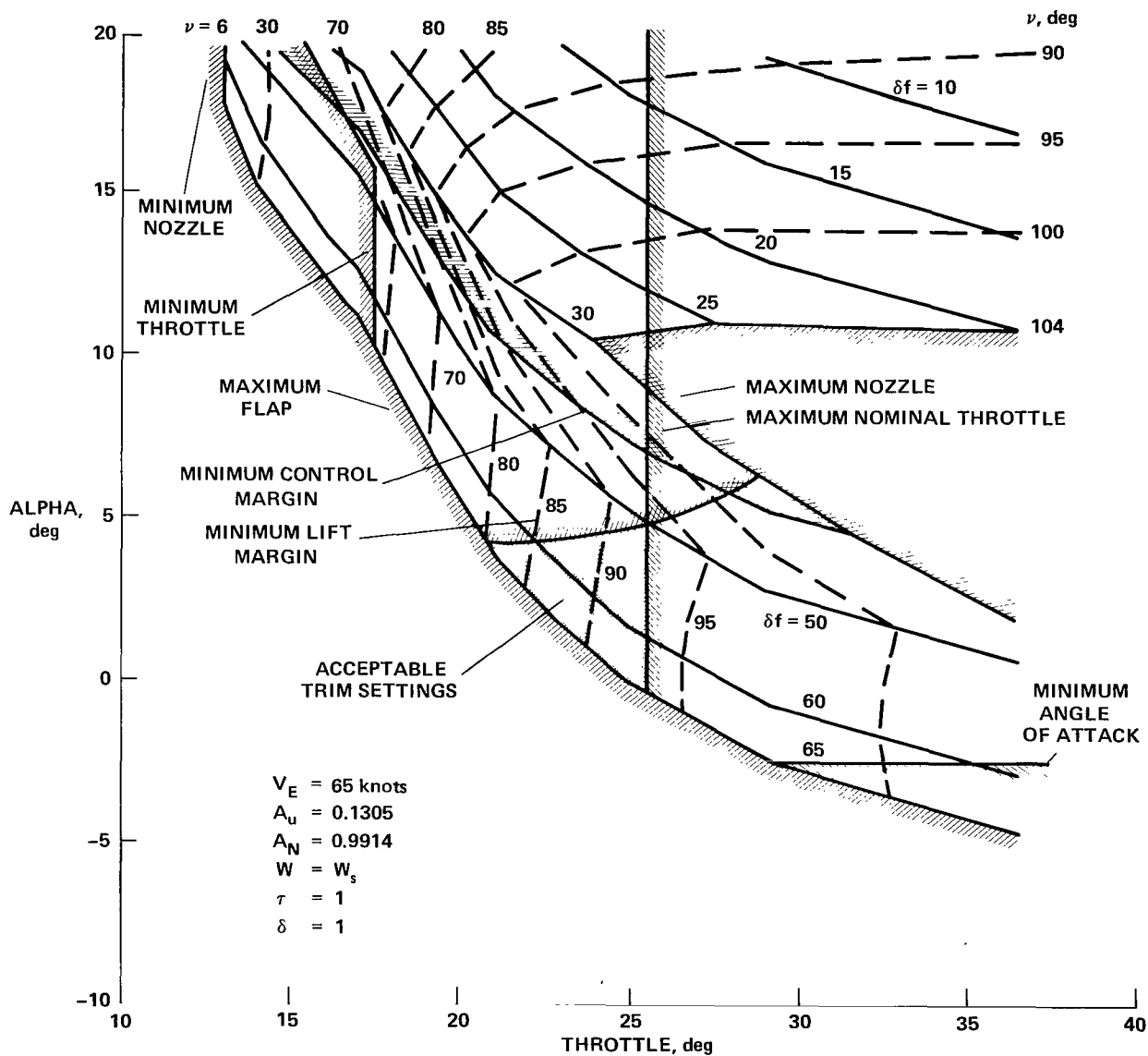
(b) Glide slope.

Figure 9.- Concluded.
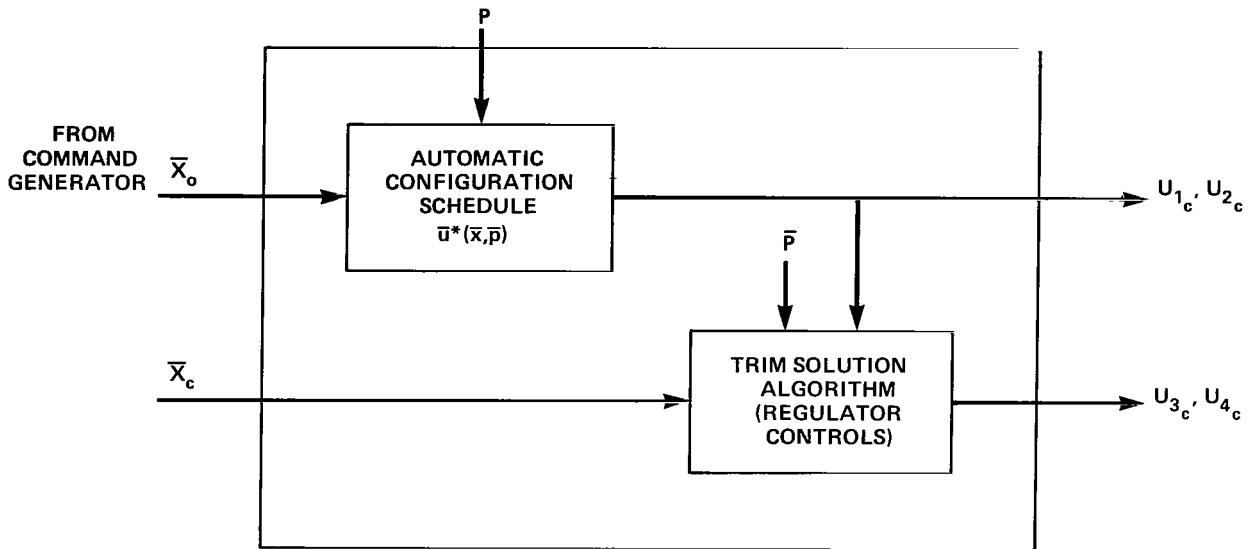
(a) Separation into scheduled
and feedback controls.
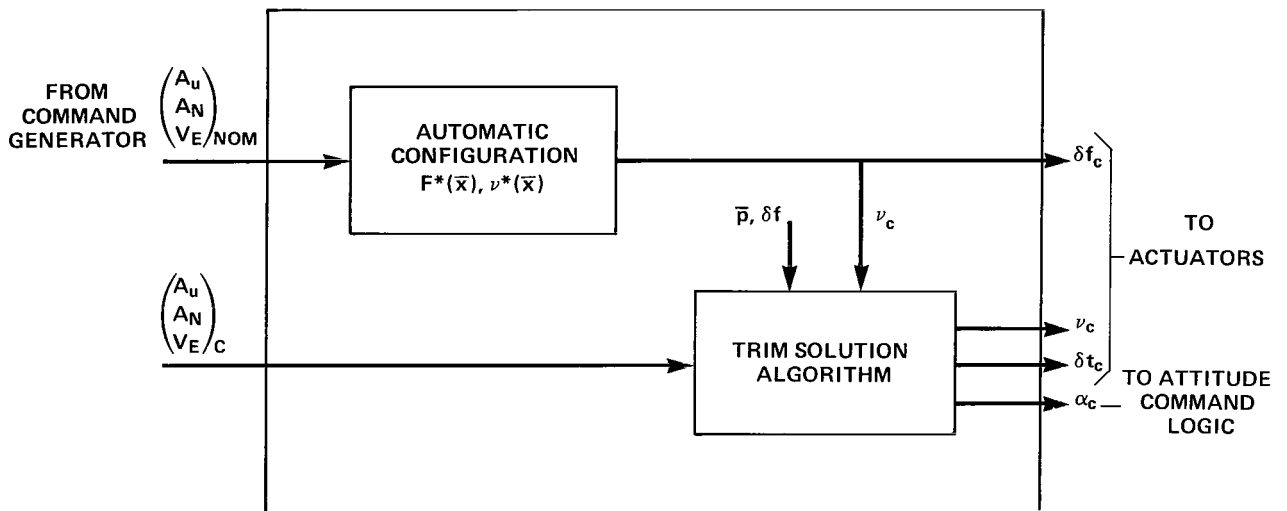
(b) Basic Trimmap – AWJSRA.

Figure 10.– Basic Trimmap structure – AWJSRA.
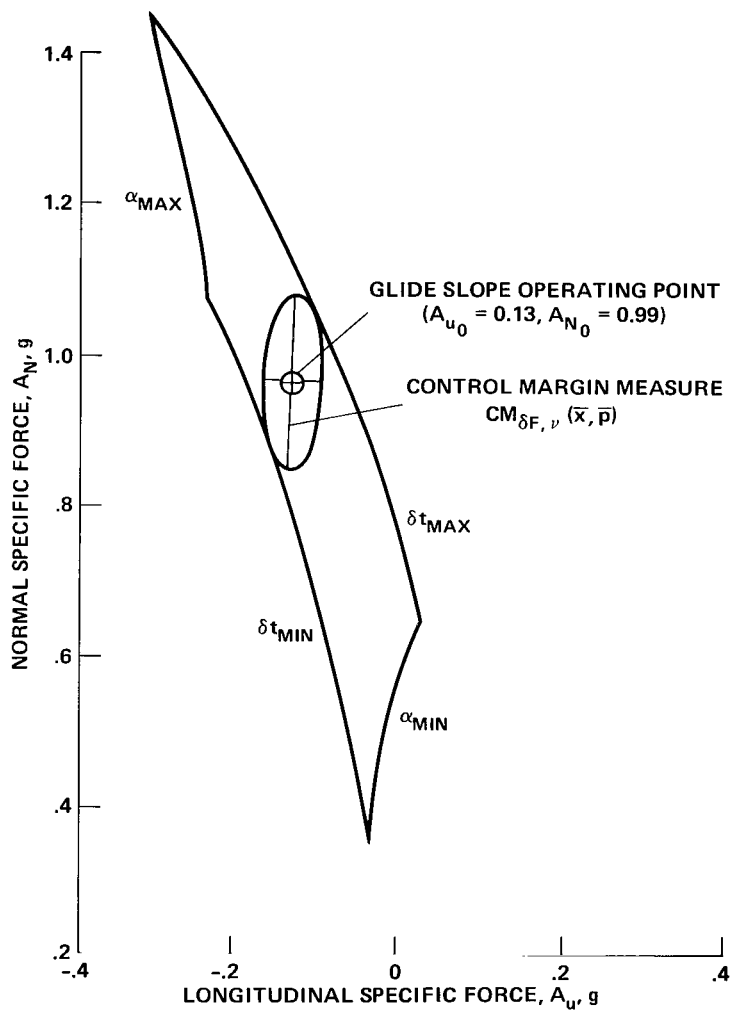
Figure 11.- Regulator control regime - fixed nozzle mode; V_E = 65 knots, δ_f = 65°, ν = 84.2°, p = p_s.
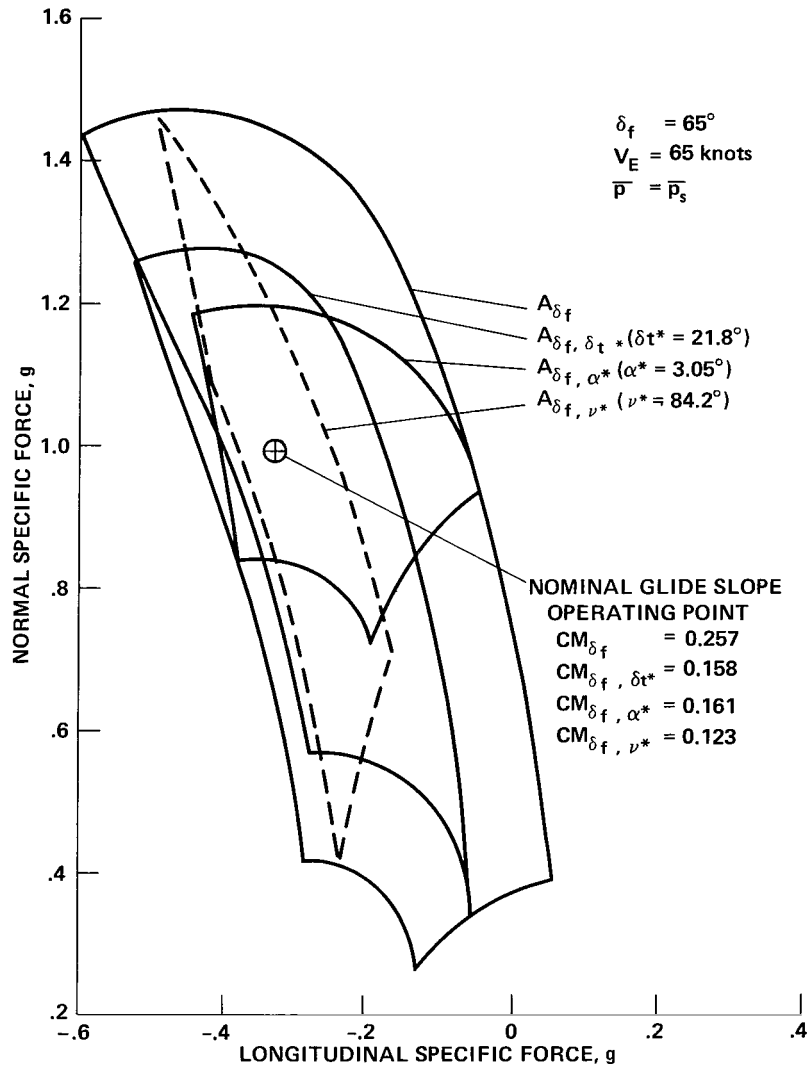
Figure 12.– Control regimes for the regulator modes – glide slope; $\delta_f = 65°$, $V_E = 65$ knots, $\overline{p} = \overline{p}_s$.

94
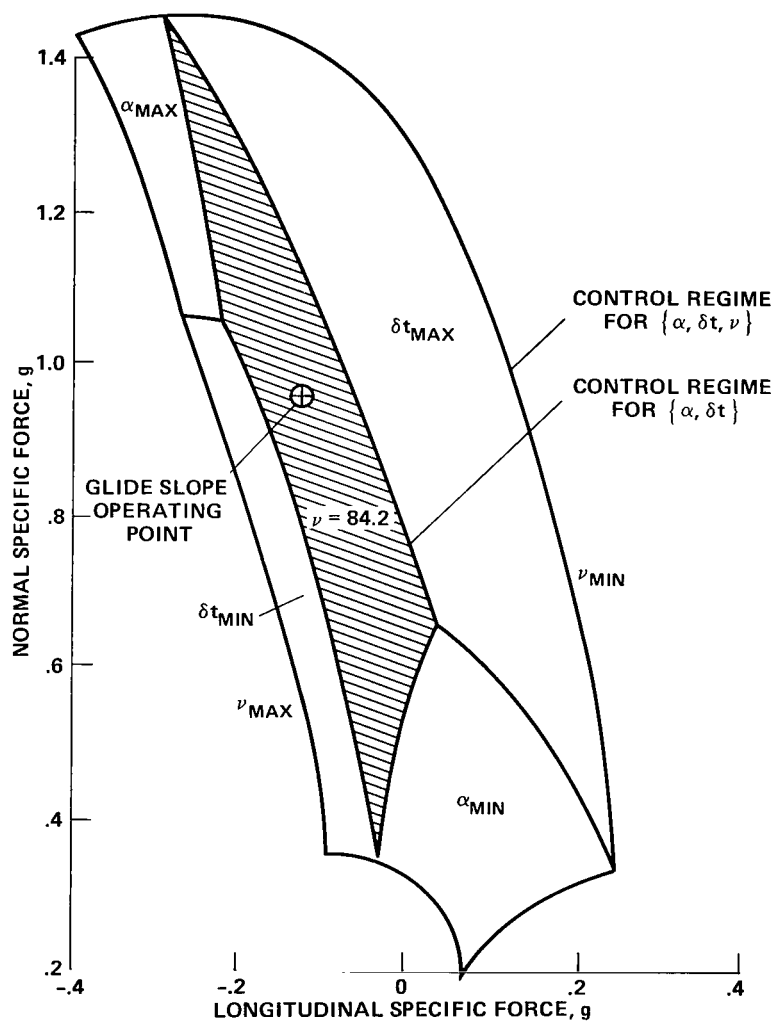
Figure 13.- Regulator control regime for three controls and mode switching
diagram - glide slope.
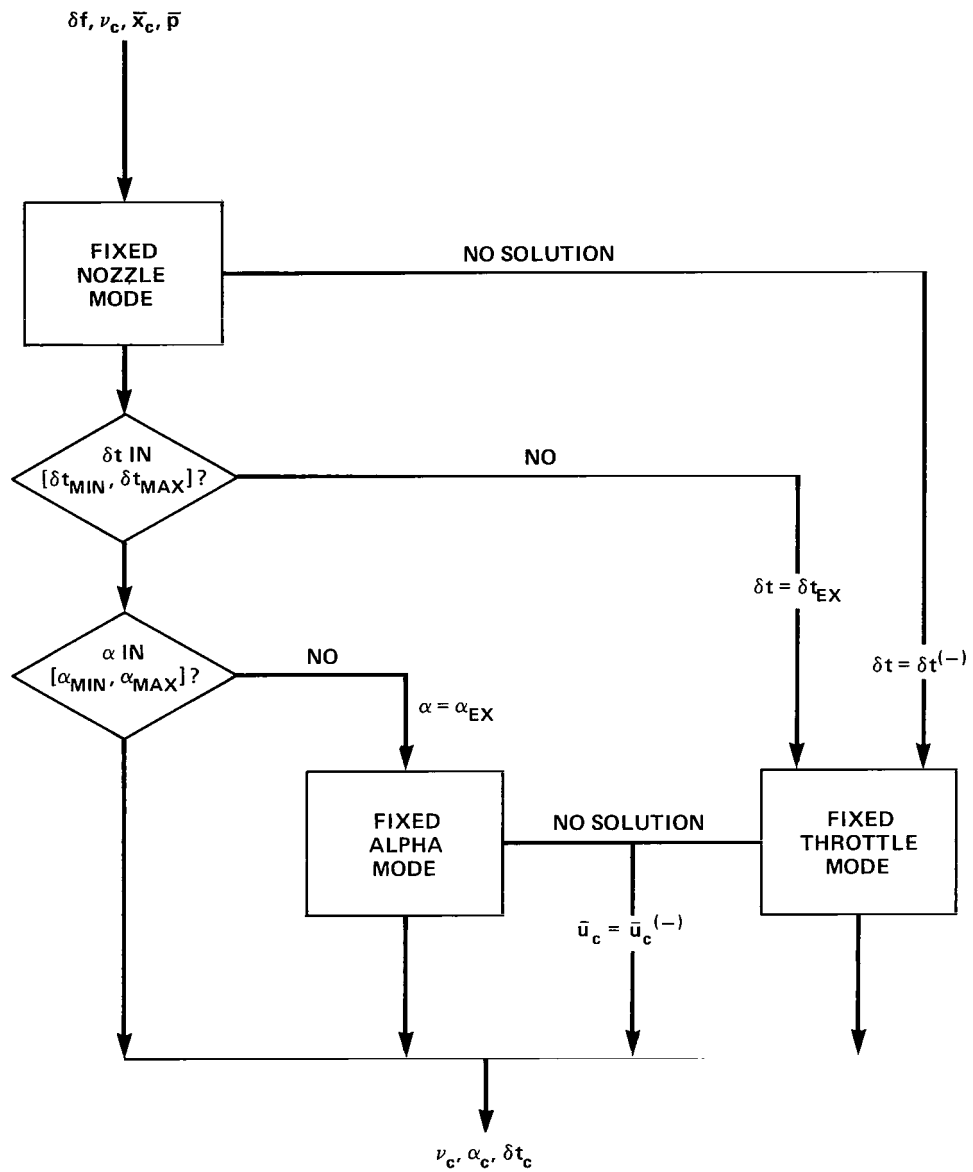
Figure 14.- Flow diagram - Trimmap regulator control logic.

Parameter	Steady flight limits	Regulator usage limits
Flap	$\delta_f \in [5.6°, \delta_{f_{max}}(V_e)]$	
Throttle	$\delta_t \in [\delta_{t_{min}}(\delta_f), \delta_{t_{max}}]$	$\delta_t \in [\delta_{t_{min}}(\delta_f), \delta_{t_{max,reg}}(\tau,\delta)]$
Nozzle	$\nu \in [6,104]$	$\nu \in [6,104]$
Lift margin	$LM(\bar{x},\bar{p},\bar{u}) \geqslant LM_{min}(\delta_f)$	
Pitch	$\theta \in [-10°, 15°]$	
	$\theta \geqslant 2°$ at touchdown	
Angle of attack		$\alpha \in [-10.5°, \alpha_{max,reg}(V_e)]$
Control margin	$CM_{\delta_f}(\bar{x},\bar{p}) \geqslant 0.25$	
Elevator	$\delta_{e_T}(x,u) \in [-17°, 7°]$	$\delta_e \in [-25°, 15°]$

(a) Constraint list.
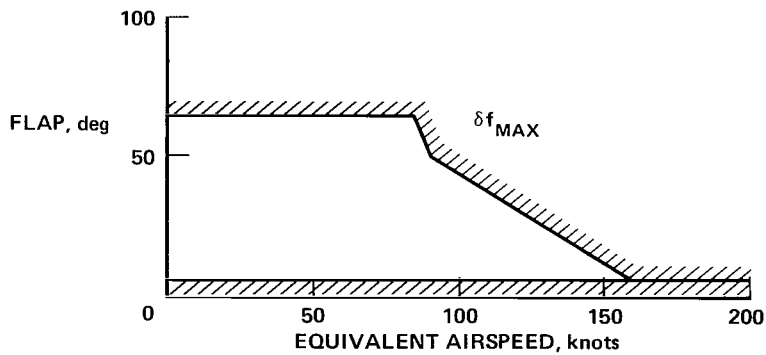
(b) Flap extremes.

Figure 15.- Operational constraints on control settings – AWJSRA.
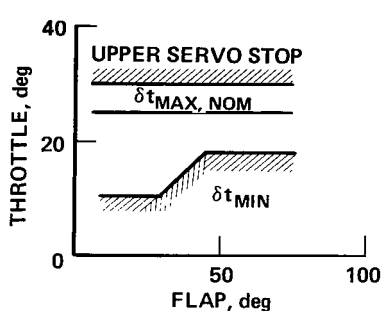
(c) Throttle extremes.
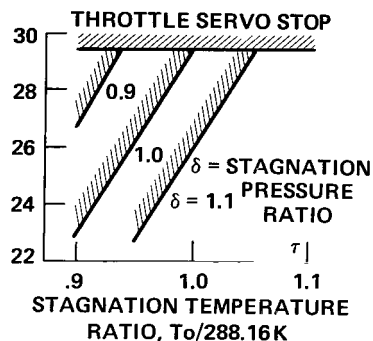
(d) Maximum throttle for regulator usage.
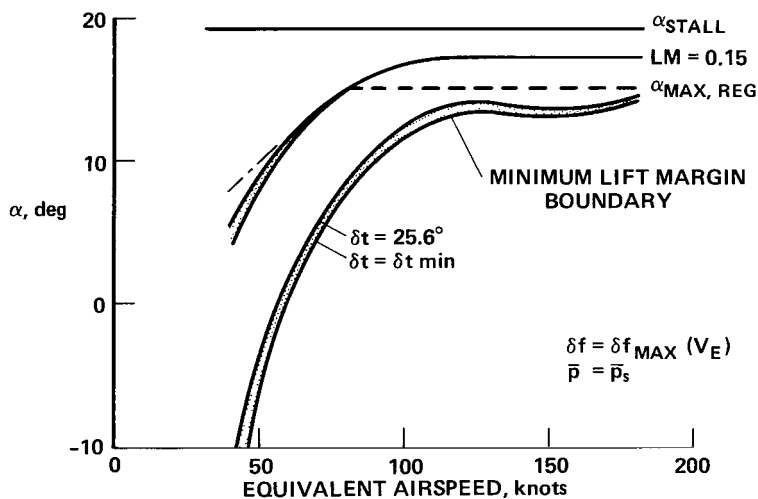
(e) Upper limits on angle of attack for lift margin constraint and regulator usage.

Figure 15.- Concluded.
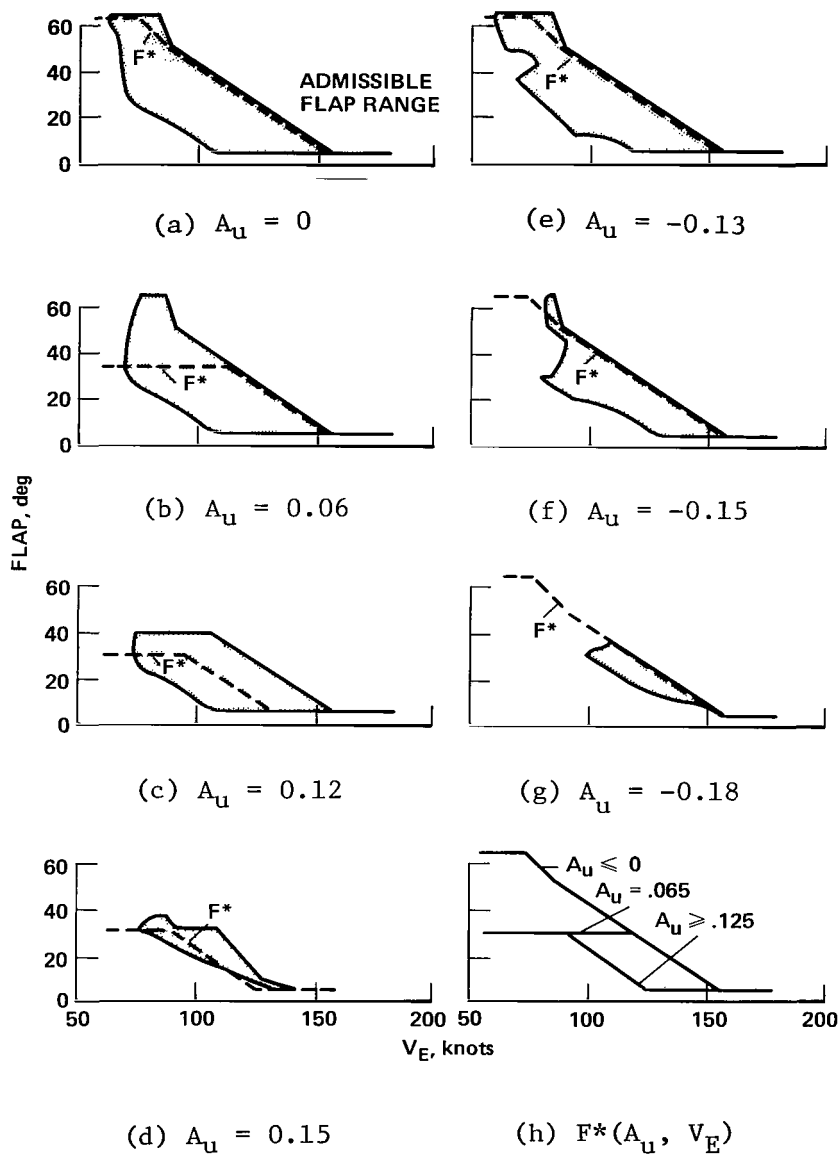
Figure 16.- Admissible flap range - standard case ($\bar{p} = \bar{p}_S$, $A_N = 1$).
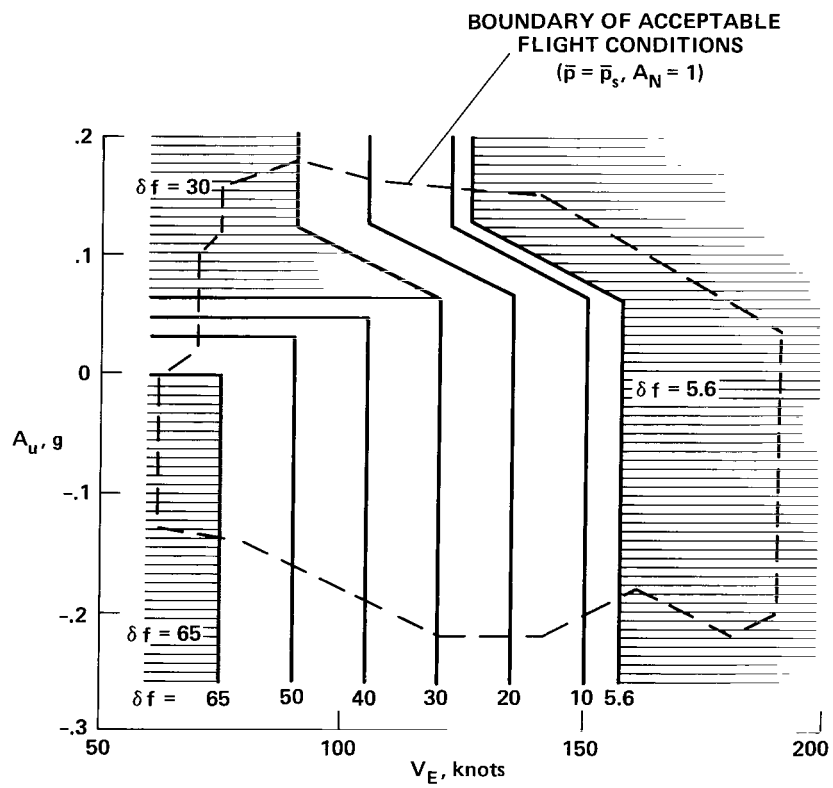
Figure 17.- Nominal flap schedule: contour plot.
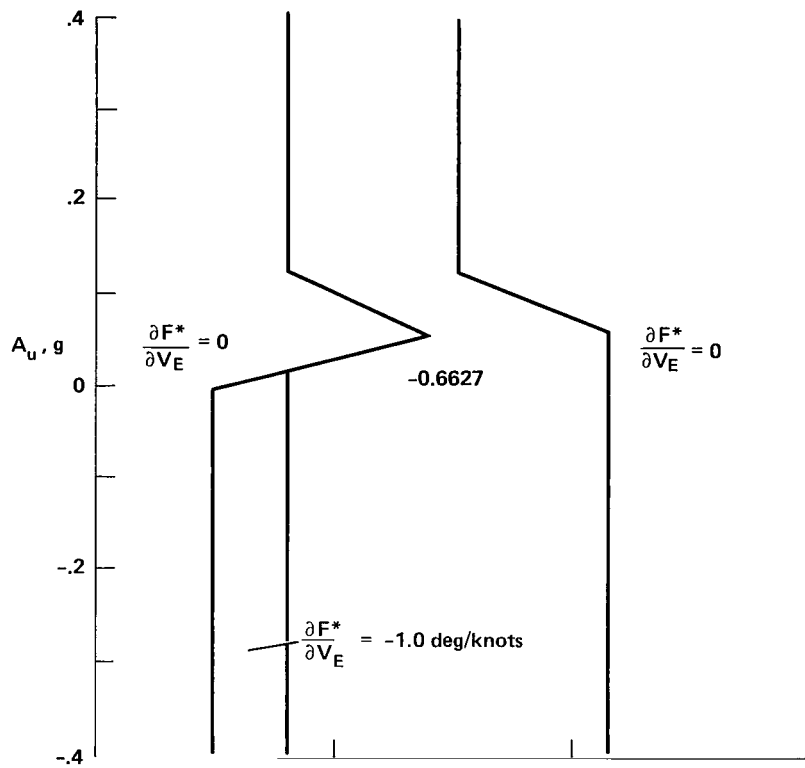
(a) Flap command rates for speed
changes $\sim \dfrac{\partial F^*}{\partial V_E} (A_u, V_E)$.
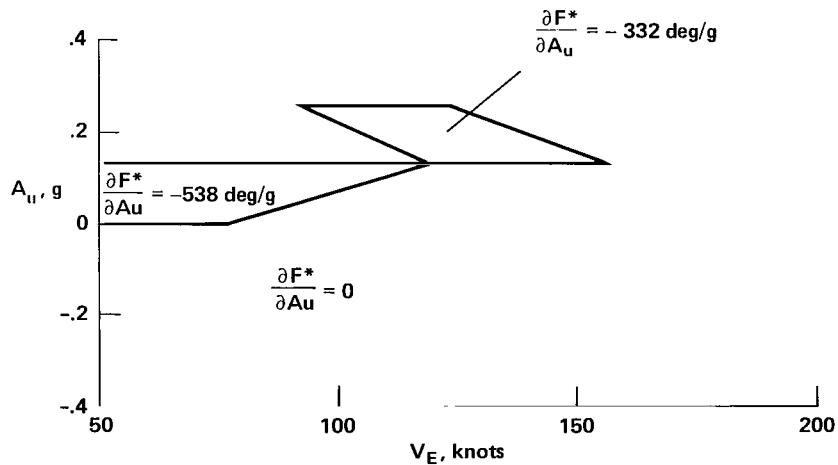
(b) Flap command rates for flight-
path angle changes $\sim \dfrac{\partial F^*}{\partial A_u} (A_u, V_E)$.

Figure 18.- Flap command rates.
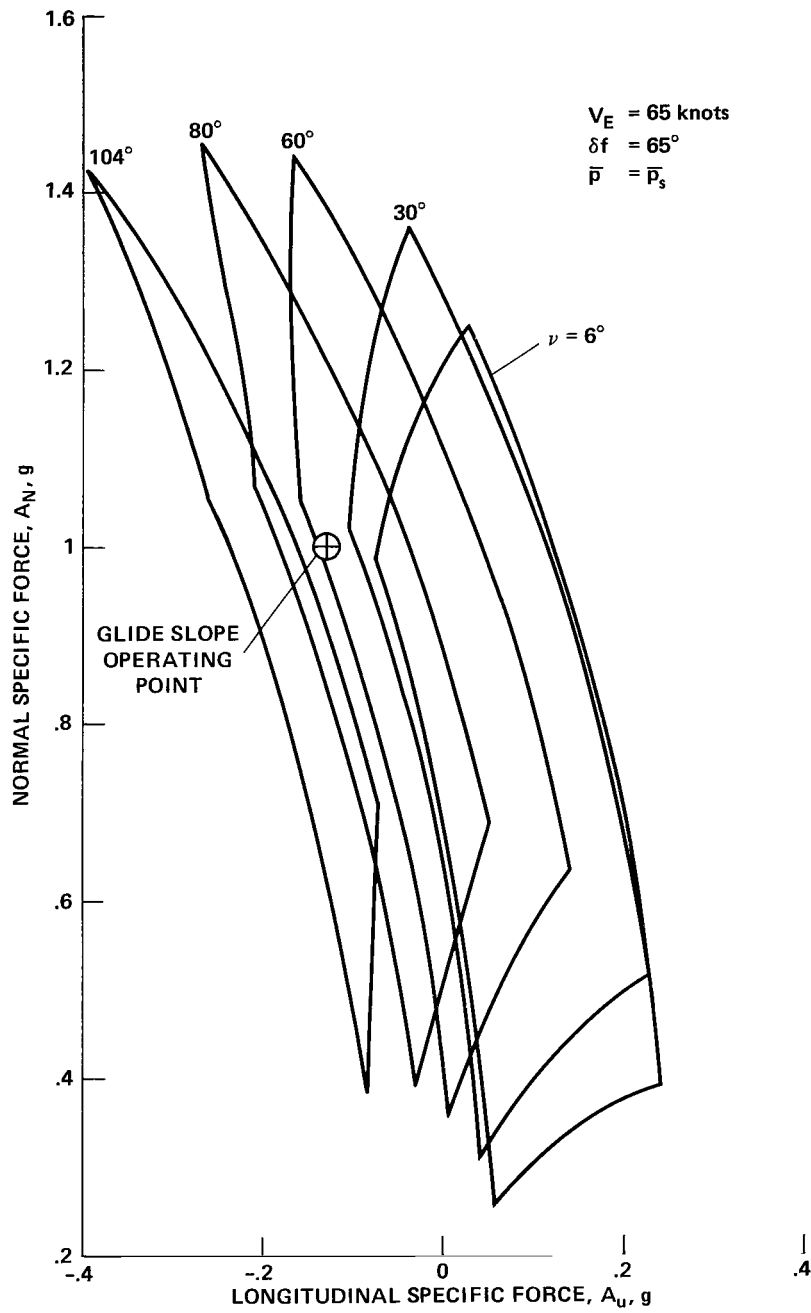
Figure 19.- Control regimes for fixed-nozzle mode; $V_E = 65$ knots, $\delta_f = 65°$, $\bar{p} = \bar{p}_s$.
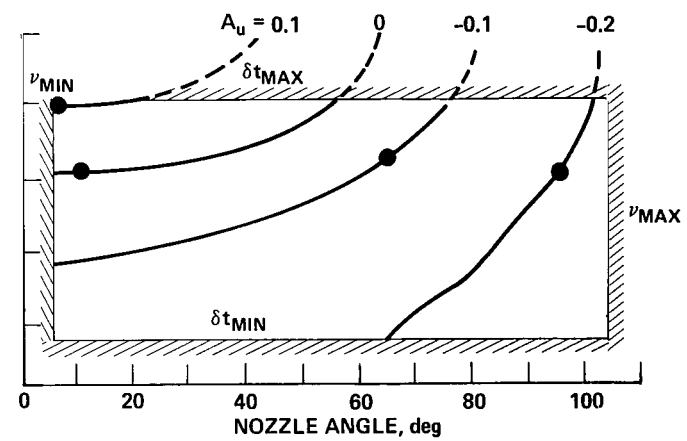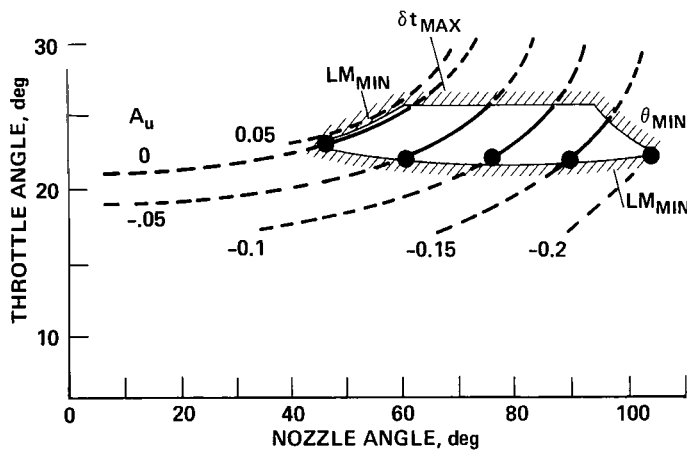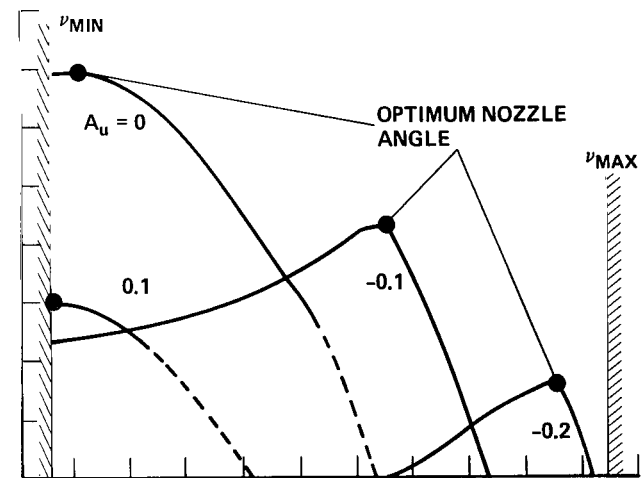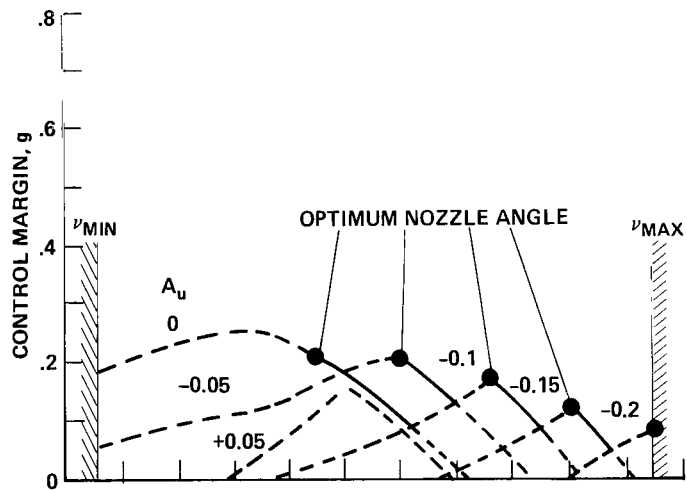
(a) V_E = 65 knots.

(b) V_E = 160 knots.

Figure 20.- Effect of nozzle angle on control margin and throttle setting
$(\bar{p} = \bar{p}_s, \quad \delta_f = F*(A_u, V_E), \quad A_N = 1)$.
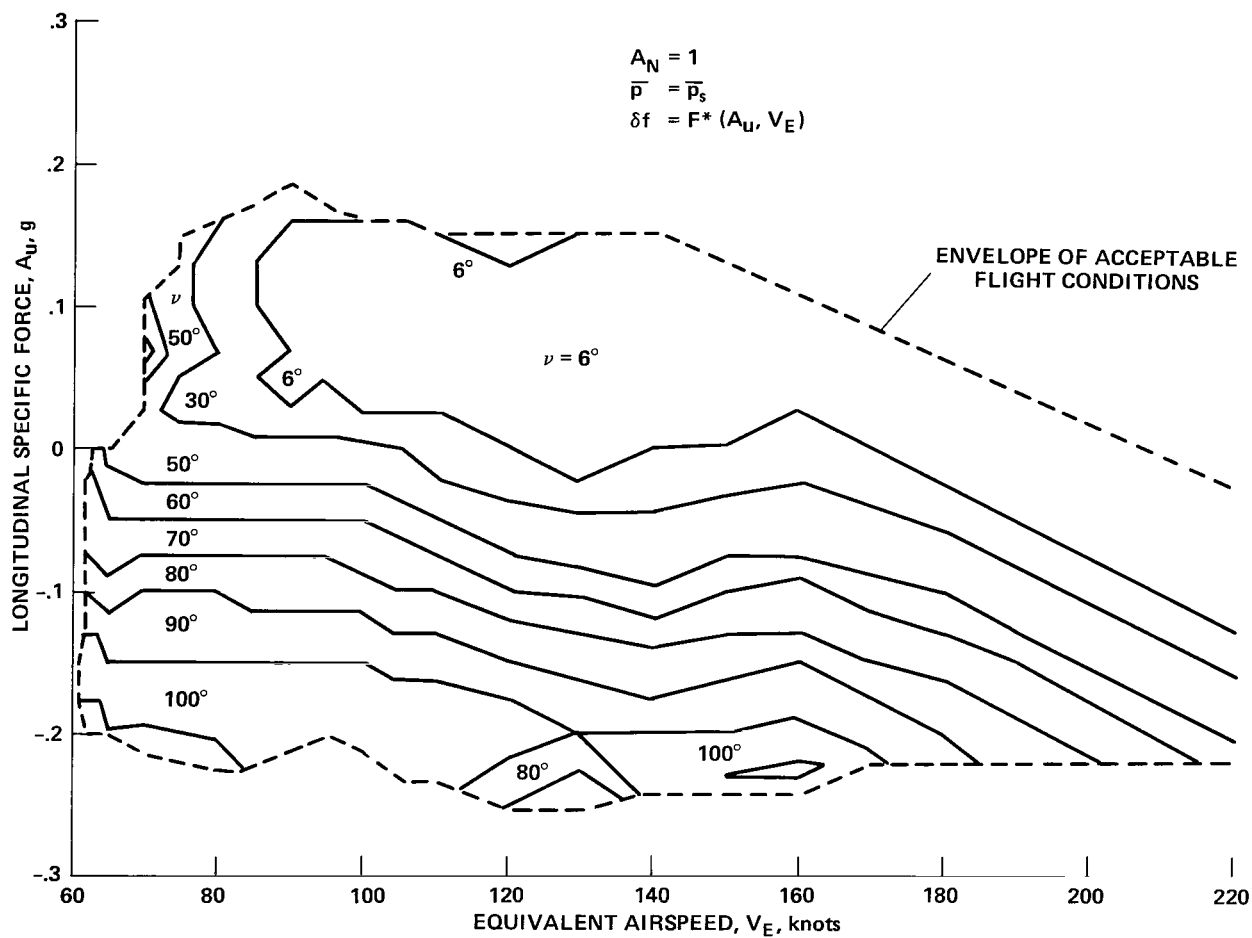
(a) Nozzle angle for maximum control margin – contour plot.

Figure 21.– Nozzle angle optimization; $A_N = 1$, $\bar{p} = \bar{p}_s$, $\delta_f = F^*(A_u, V_E)$.
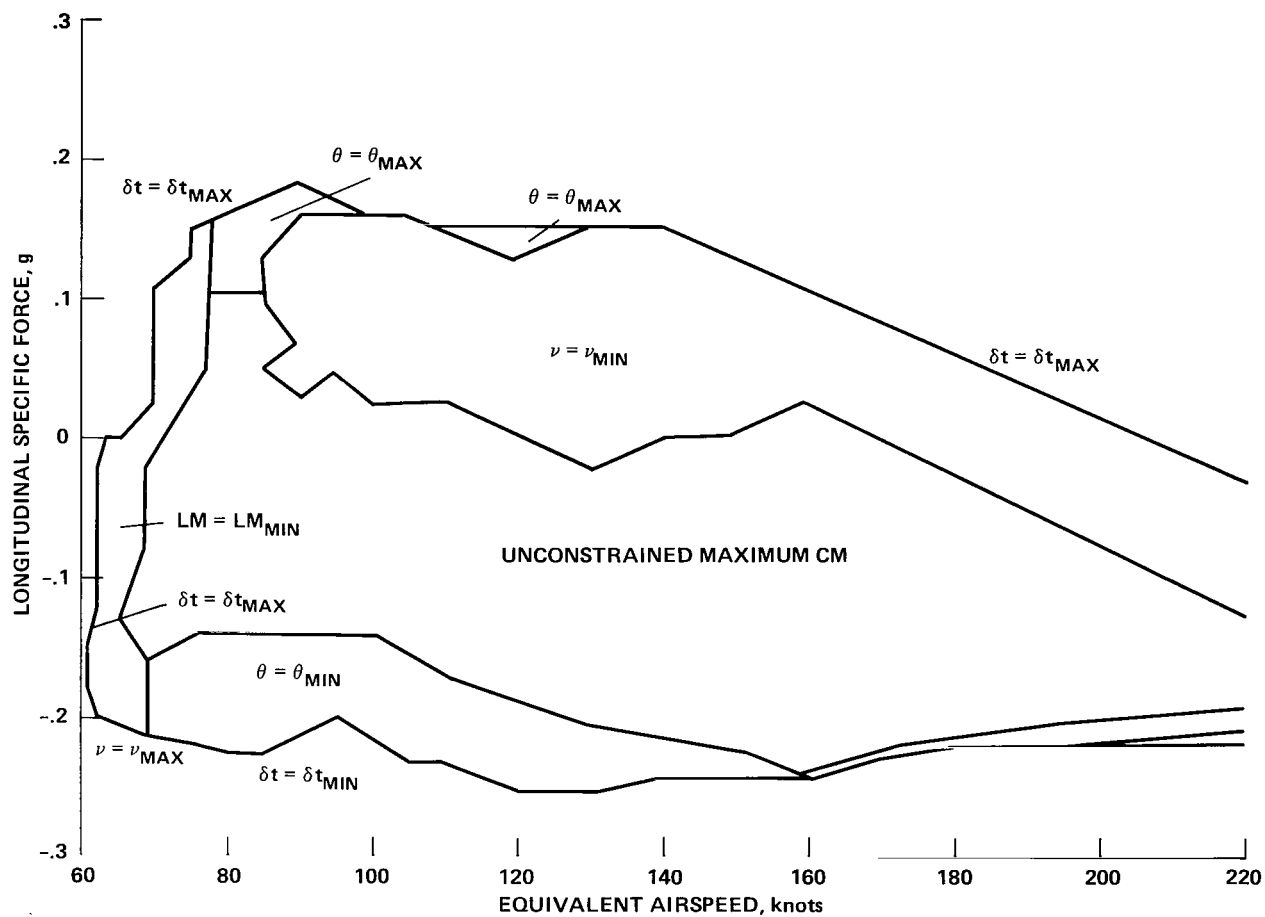
(b) Regions of constraint saturation.

Figure 21.- Concluded.

$$\nu^*(x) = \min\left\{104, \max\left[\ell_0(x)\,\ell_1(x), q(x), 6\right]\right\}$$

$$q(x) = \begin{cases} 6 - 645.33(A_u - \Delta)\,[1 + 1.57(A_u - \Delta)] & A_u - \Delta \geqslant -0.318 \\ 104 & A_u - \Delta < -0.318 \end{cases}$$

$$\Delta = \min(\Delta_1, \Delta_2)$$

$$\Delta_1 = 0.25(1.12 - A_N) - \max\left\{0, \min\left[0.15(1.14 - A_N), 0.06\right]\right\} * \max\left\{0, \min\left[(V_E - 100)/20, 1\right]\right\}$$

$$\Delta_2 = 0.0025\,[50(4.4 - A_N) - V_E]$$

$$\ell_0(x) = a_0 - 180\,A_u$$

$$a_0 = \min\left\{65, 125(1.52 - A_N), 4(V_{E_0} - V_E)\right\}$$

$$V_{E_0} = \max\left\{77, 65(2.185 - A_N)\right\}$$

$$\ell_1(x) = a_1 + \min\left\{0, 600(A_u - 0.065)\right\}$$

$$a_1 = \min\left\{80, 75(1.867 - A_N), 4[21.875(A_N + 2.97) - V_E]\right\}$$
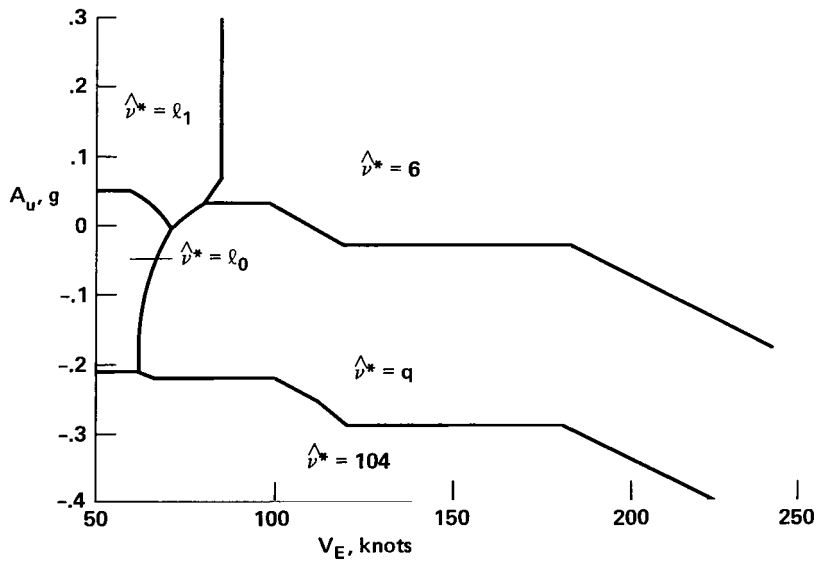
(a) Function generator for $\hat{\nu}^*$ and domains of each of the generating functions at $A_N = 1$.

Figure 22.- Nozzle schedule for maximum control margin.
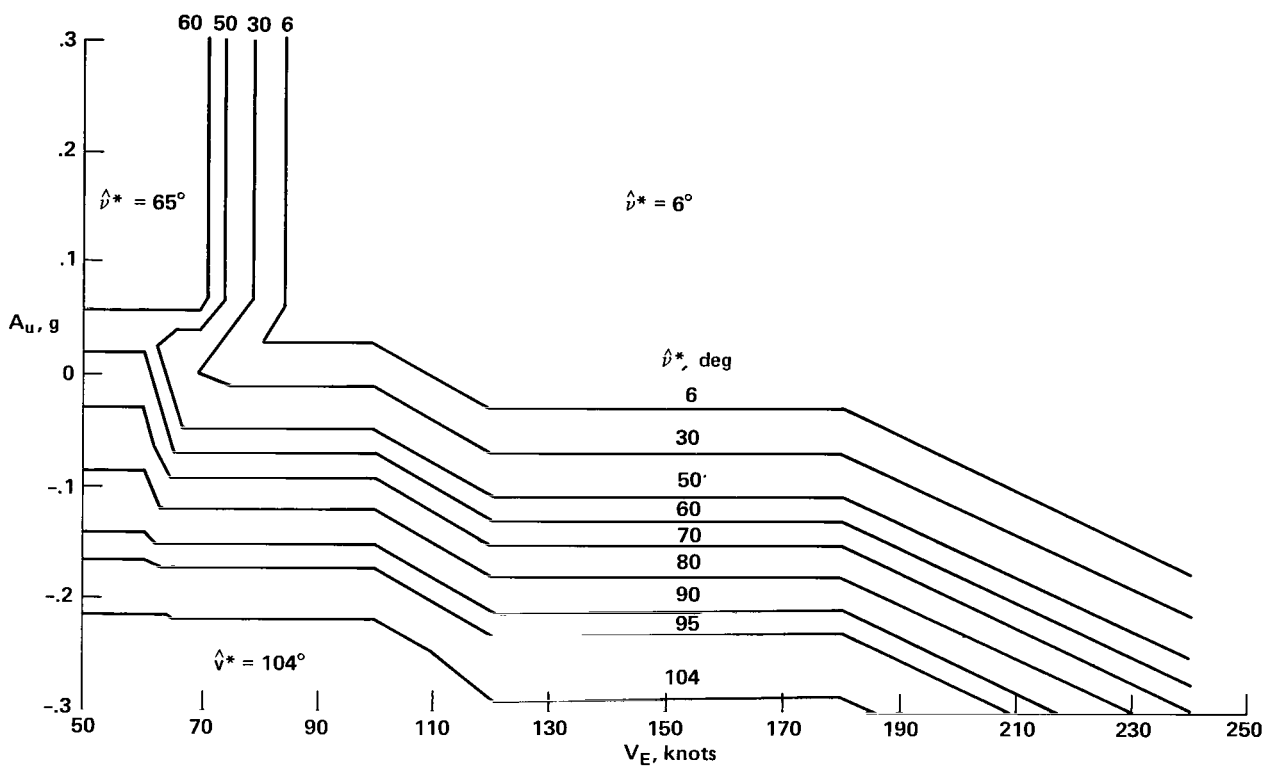
(b) Nozzle schedule – contour plot (A_N = 1).

Figure 22.– Continued.

(c) Nozzle schedule: acceptable flight envelope and envelope abuse buffer region ($A_N = 1$, $p = p_s$, $\delta_f = F*$).

Figure 22.- Concluded.
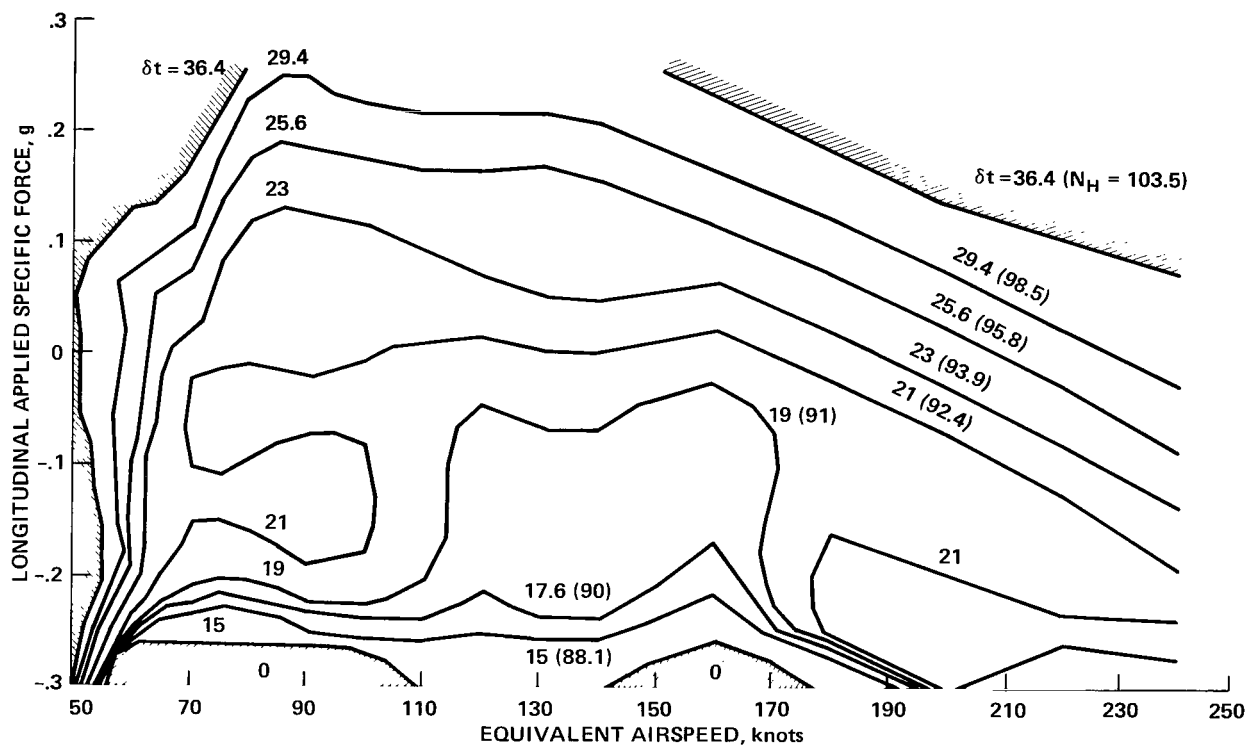
(a) Throttle setting, deg.

Figure 23.- Trim solutions for automatic configuration schedule $(A_N = 1, \ \bar{p} = \bar{p}_s)$.
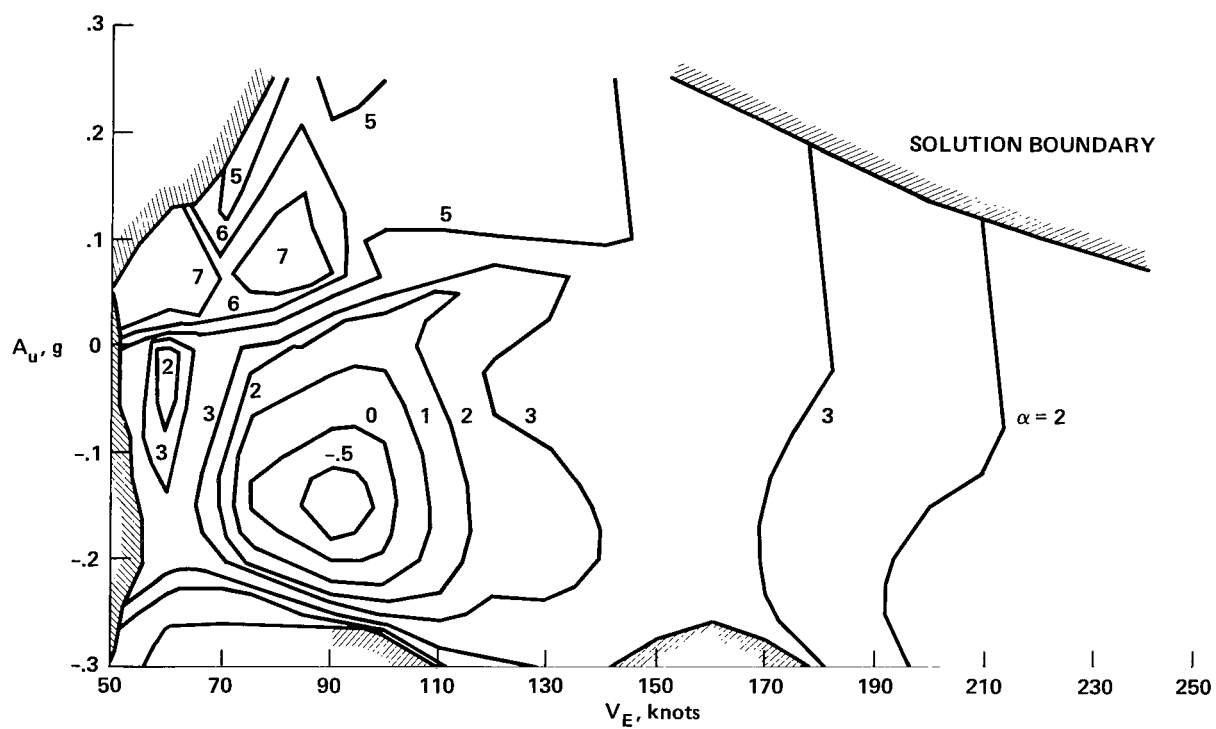
(b) Angle of attack, deg.

Figure 23.- Continued.
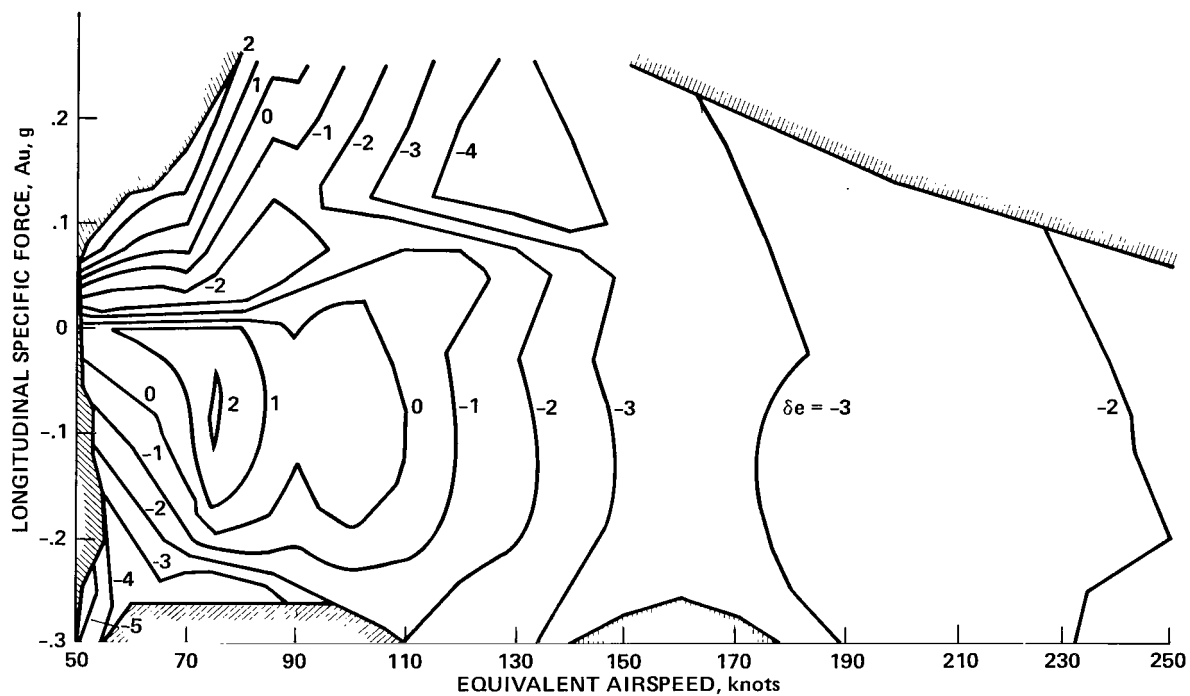
(c) Trim elevator setting, deg.

Figure 23.- Continued.
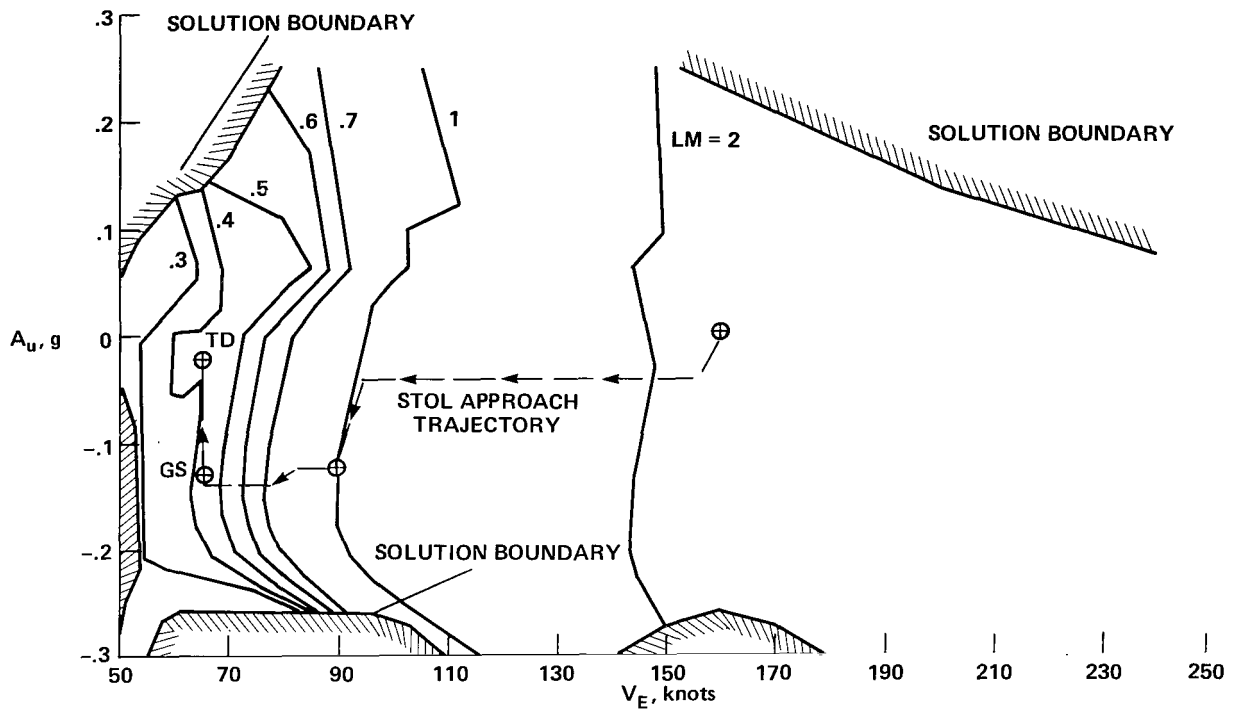
(d) Lift margin, g.
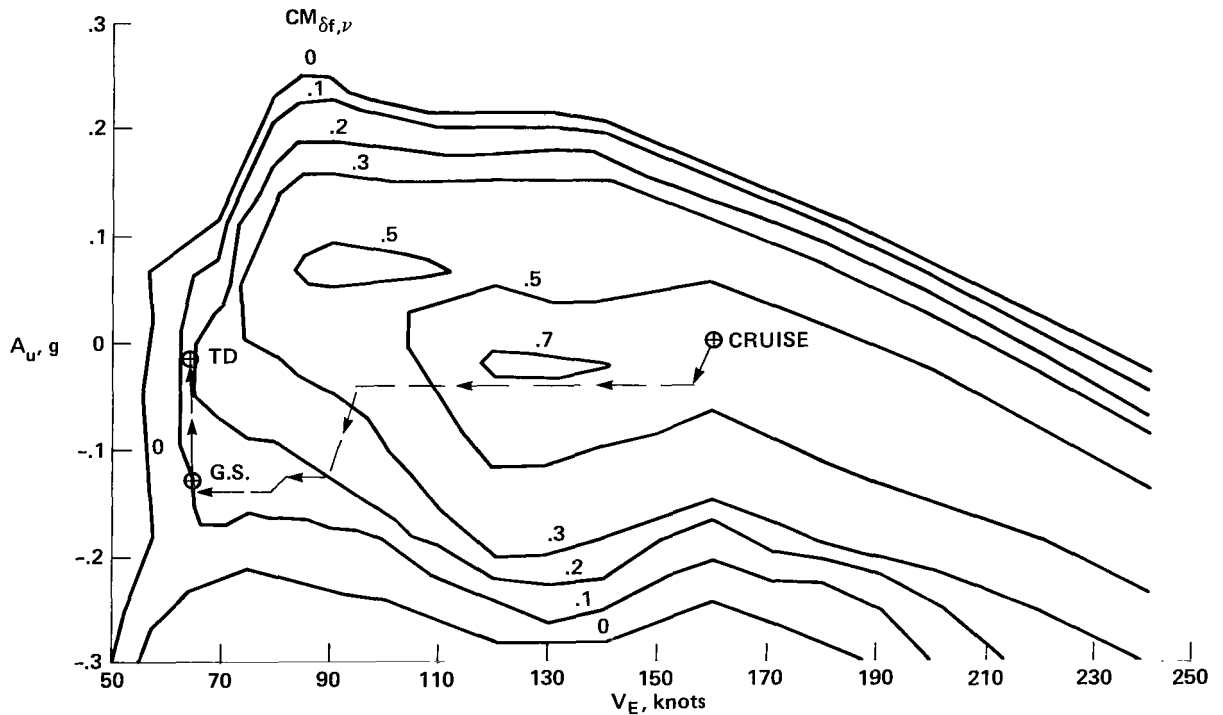
(e) Central mode control margin, $CM_{\delta_f,\nu}$, g.

Figure 23.- Concluded.
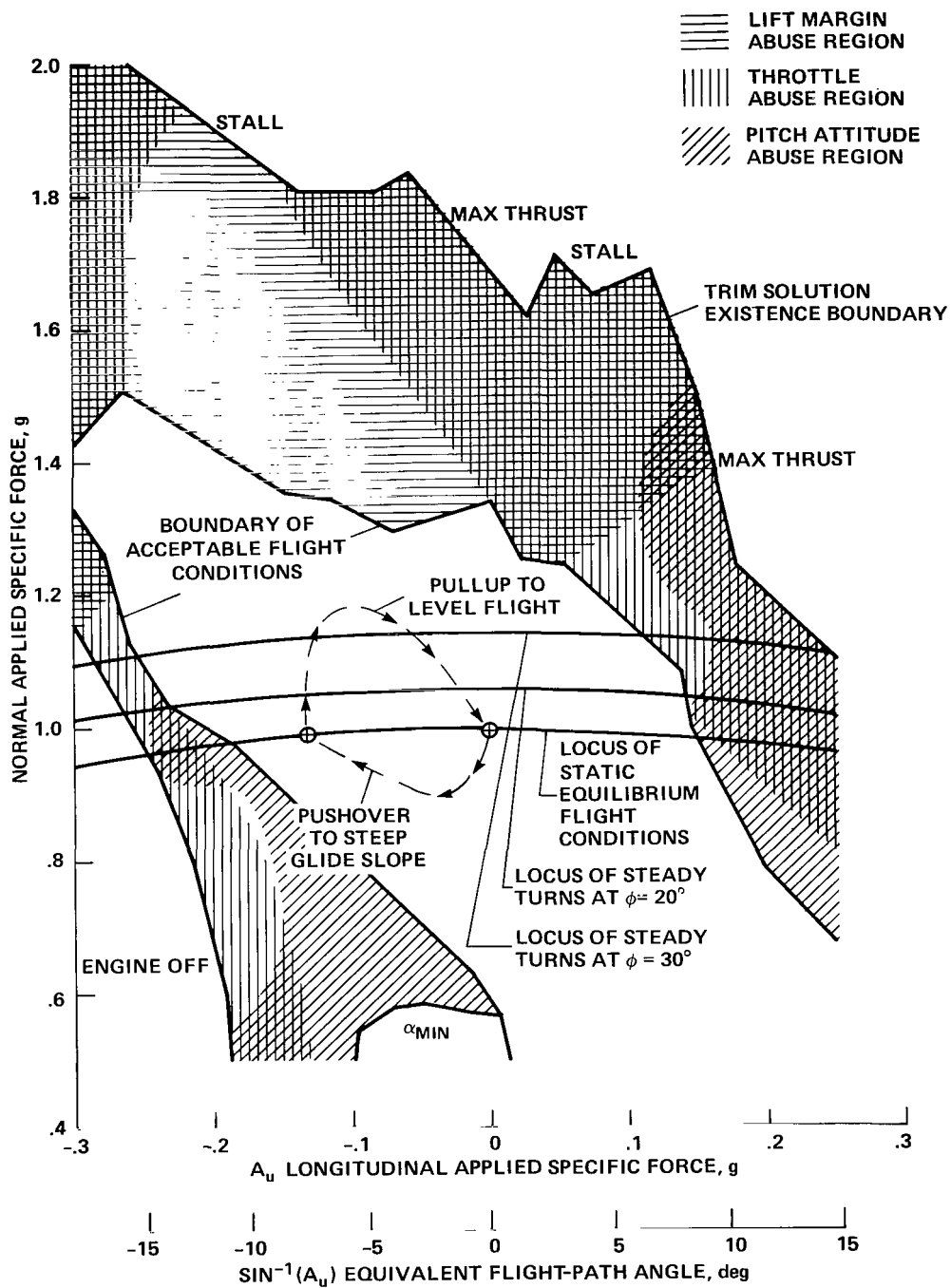
(a) Acceptable flight envelope and envelope abuse buffer region.

Figure 24.– Trim solutions for the configuration schedule –
V_E = 80 knots (p = p_s).

113
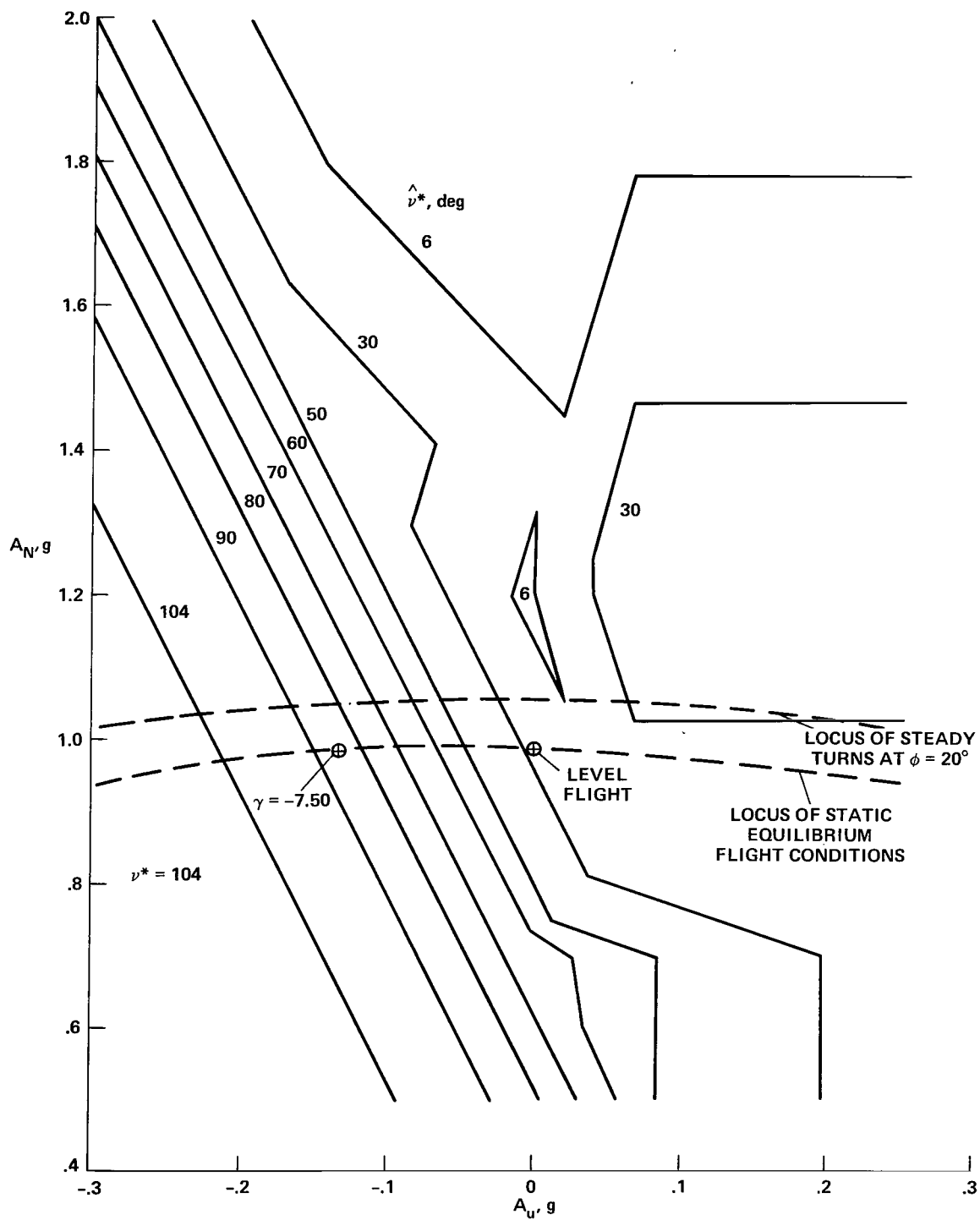
(b) Nozzle schedule contour plot (V_E = 80 knots).

Figure 24.– Continued.
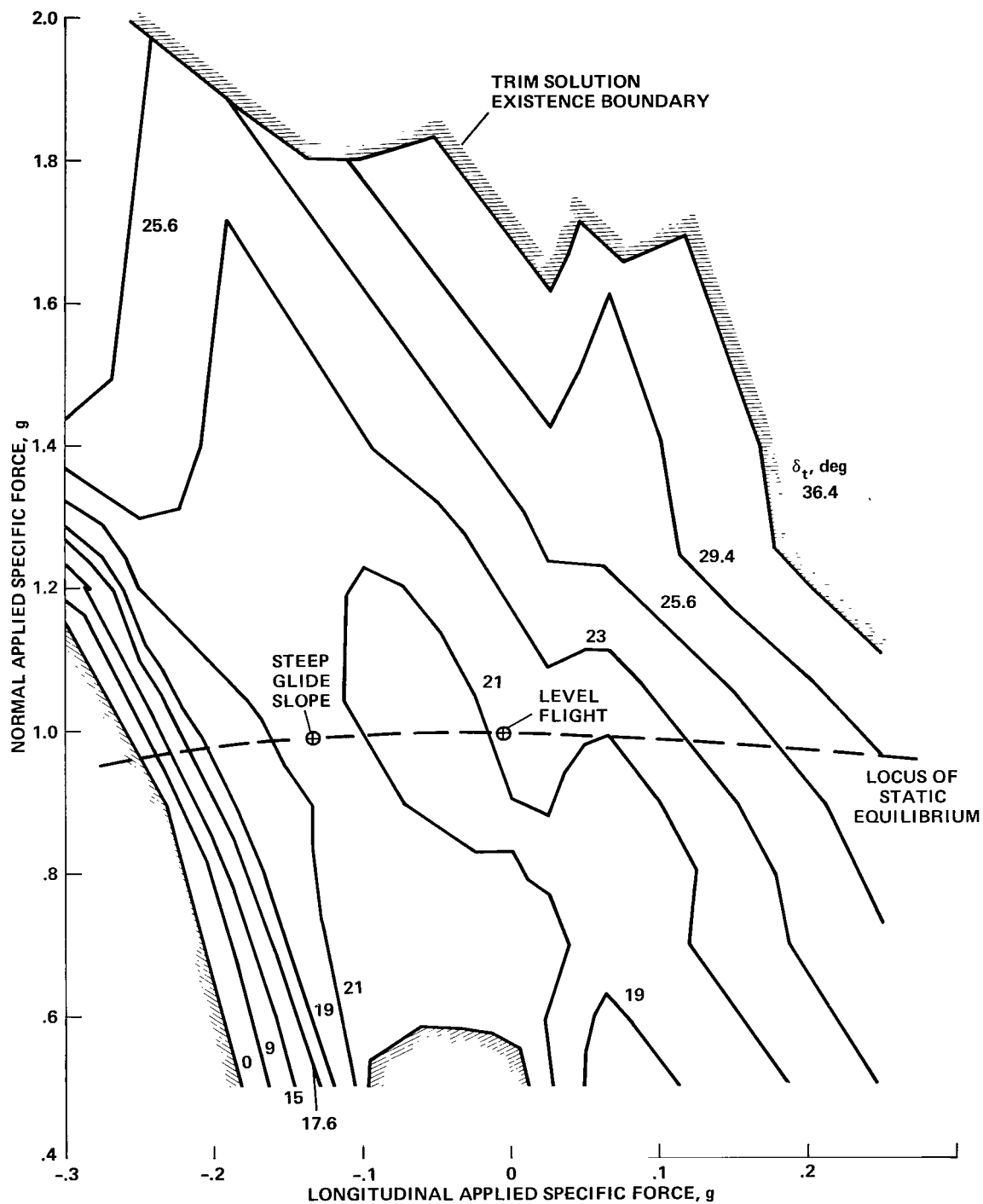
(c) Trim throttle setting contour plot (V_E = 80 knots).

Figure 24.- Continued.
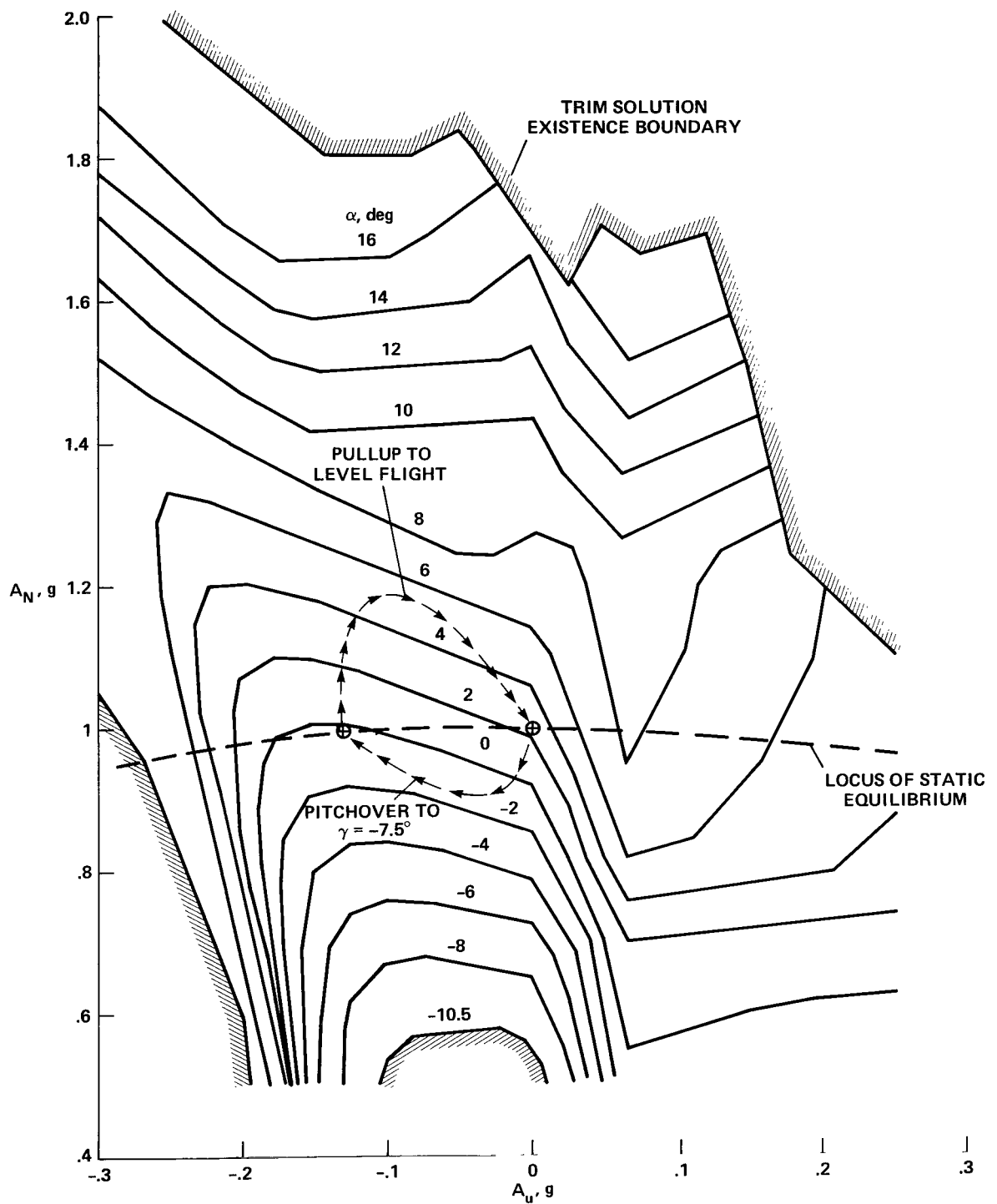
(d) Trim angle of attack contour plot (V_E = 80 knots).

Figure 24.- Continued.
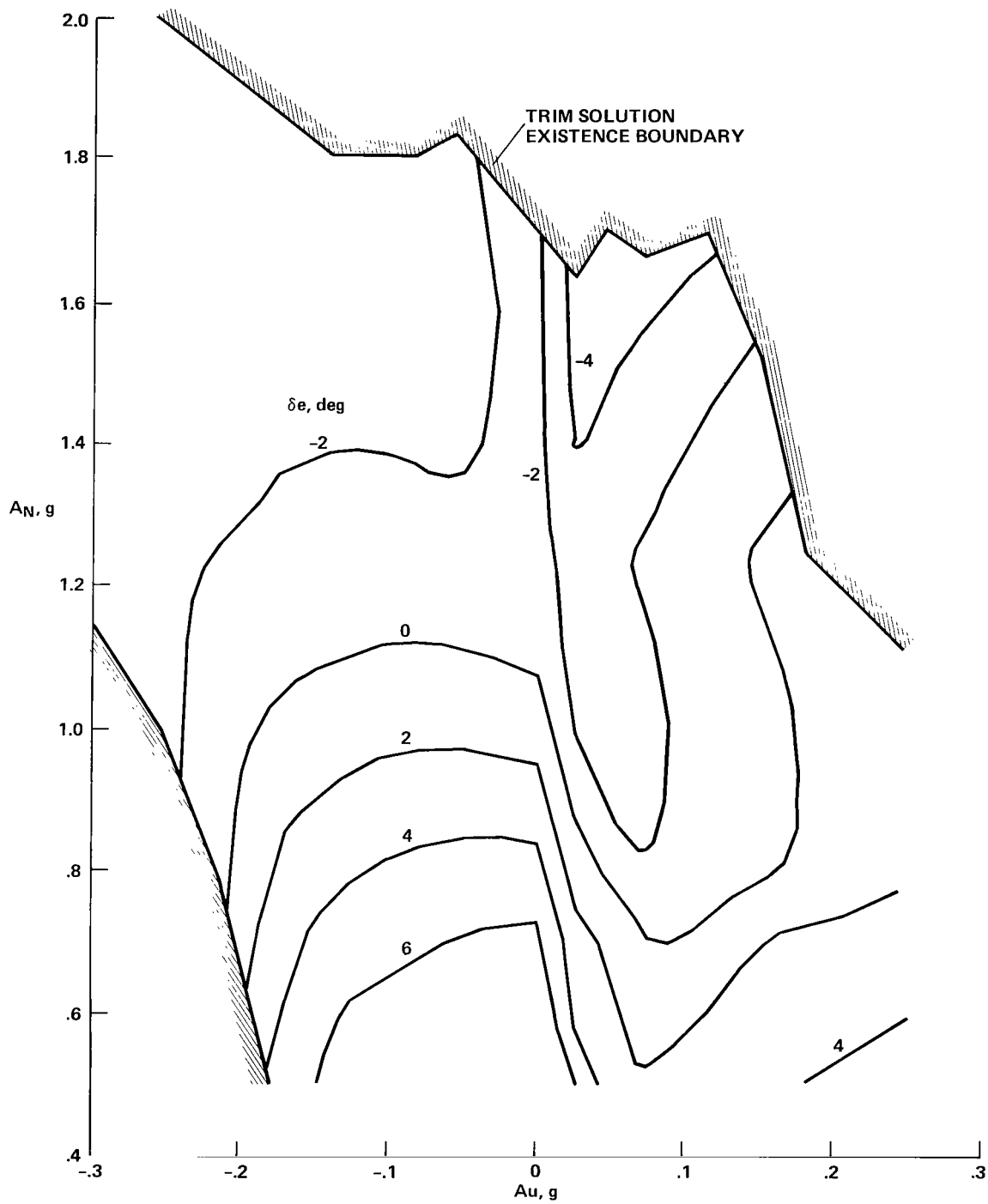
(e) Trim elevator setting contour plot (V_E = 80 knots).

Figure 24.- Concluded.
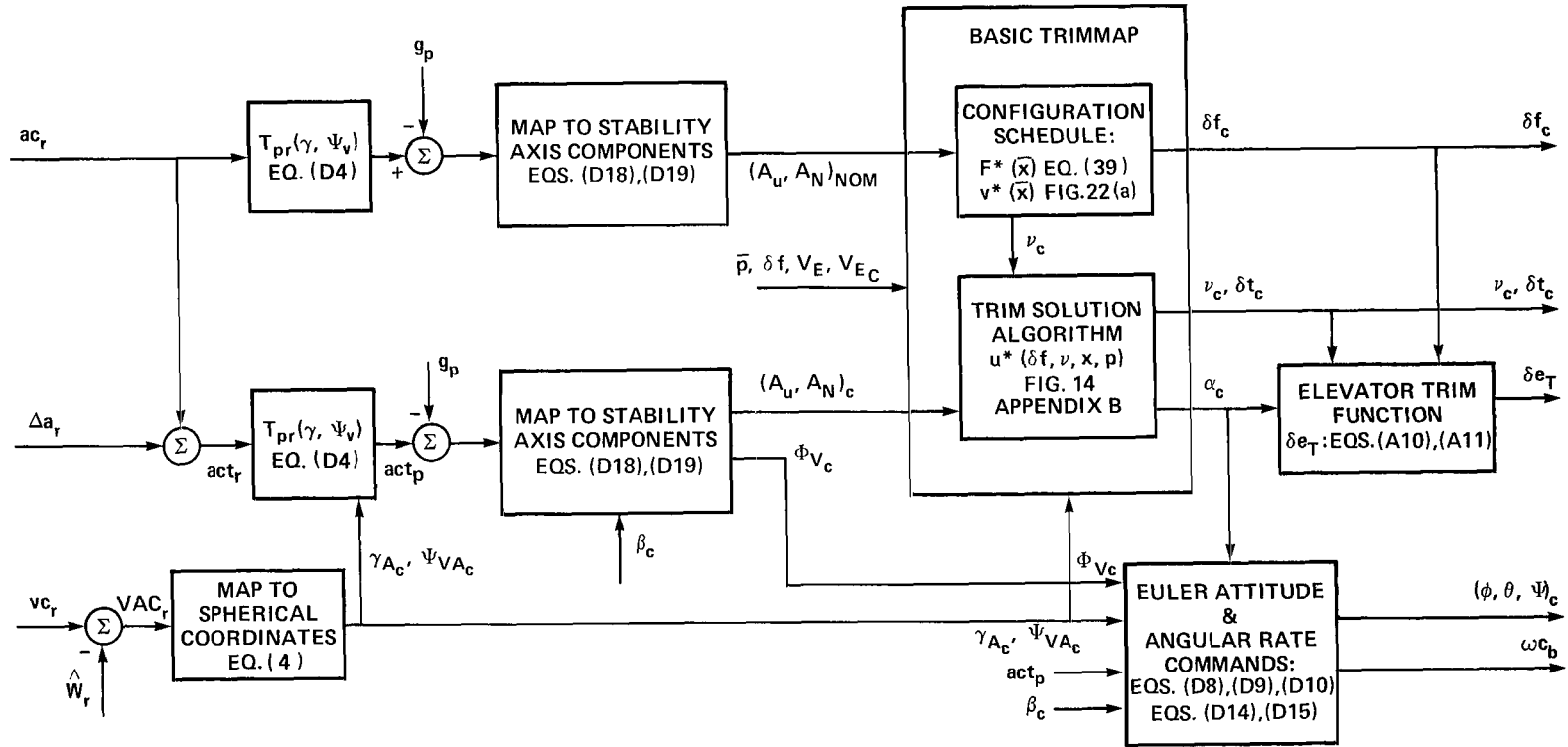
Figure 25.- AWJSRA Force Trimmap.
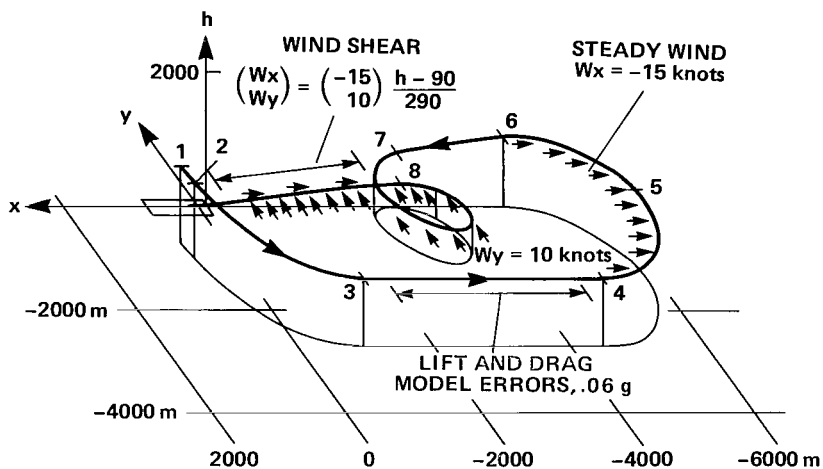
TRAJECTORY INPUT PARAMETERS

Leg	Initial time (sec)	Initial position			Initial velocity			Acceleration		
		x_o, m	y_o, m	z_o, m	V, knots	Φ_V, deg	γ, deg	$\dot{V}_H$, g	R_c, m	$\ddot{z}$, g
1	0	629.3	-800.6	-1161.6	140	270	0	0	∞	0
2	12	629.3	-914.6	-1161.6	140	270	-3	0	-1524	0
3	45	-894.8	-2439.0	-1036.0	140	180	0	-.02	∞	0
4	96	-4298.8	-2439.0	-1036.0	120	180	0	0	-1219	0
5	127	-5518.3	-1219.5	-1036.0	120	90	0	-.035	-1219	0
6	161	-4298.8	0	-1036.0	96.3	0	-5.9	-.021	∞	0
7	194	-2807.9	0	-884.1	83.7	0	-7.5	-.01	-610	0
8	294	-2807.9	0	-381.1	65	0	-7.5	0	∞	0
9	379.9	40.0	0	-6.1	65	0	-1.6	0	∞	0

Figure 26.- Four-dimensional simulation test approach path.
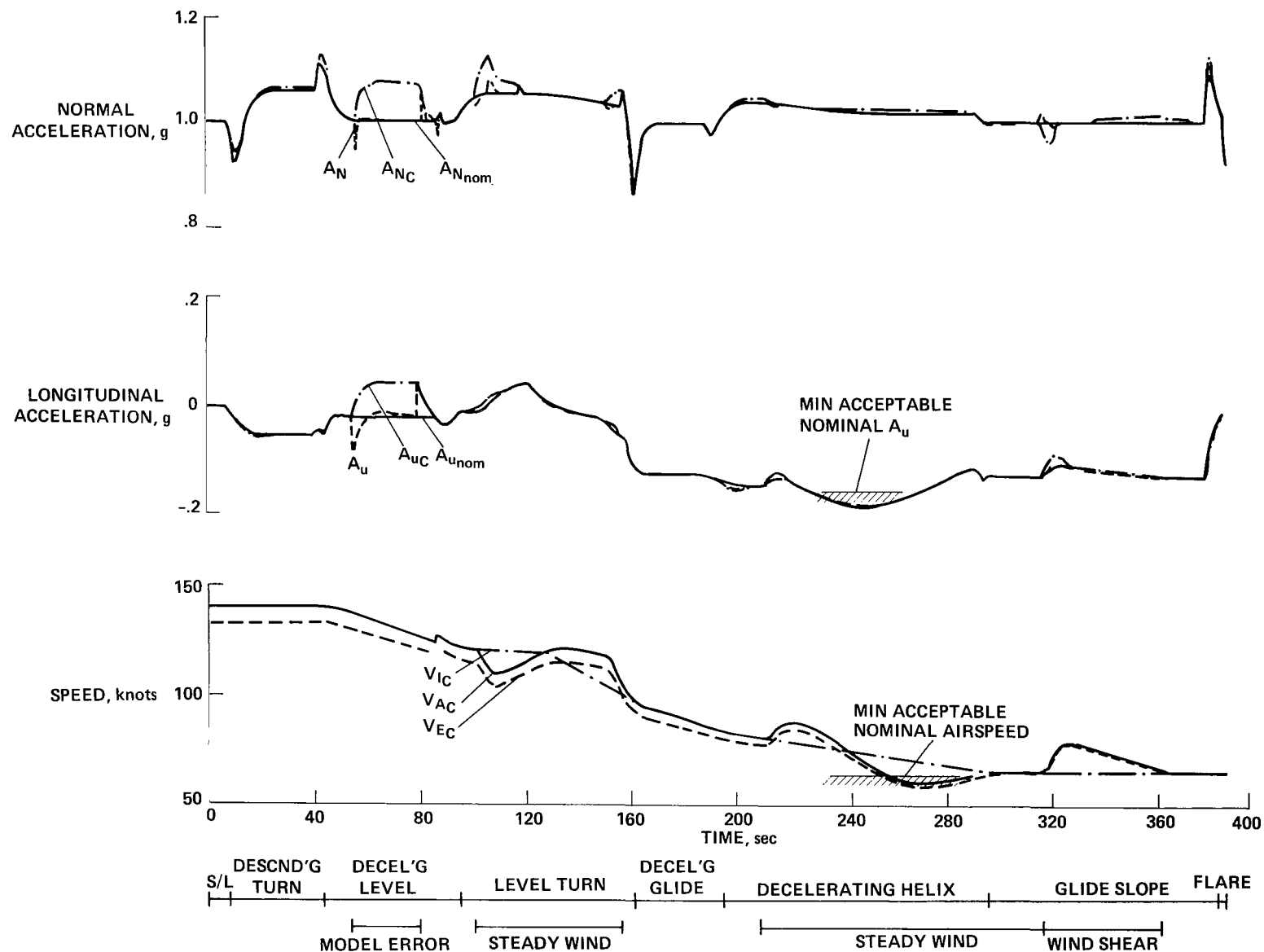
(a) Acceleration and speed commands.

Figure 27.- Simulation test path.
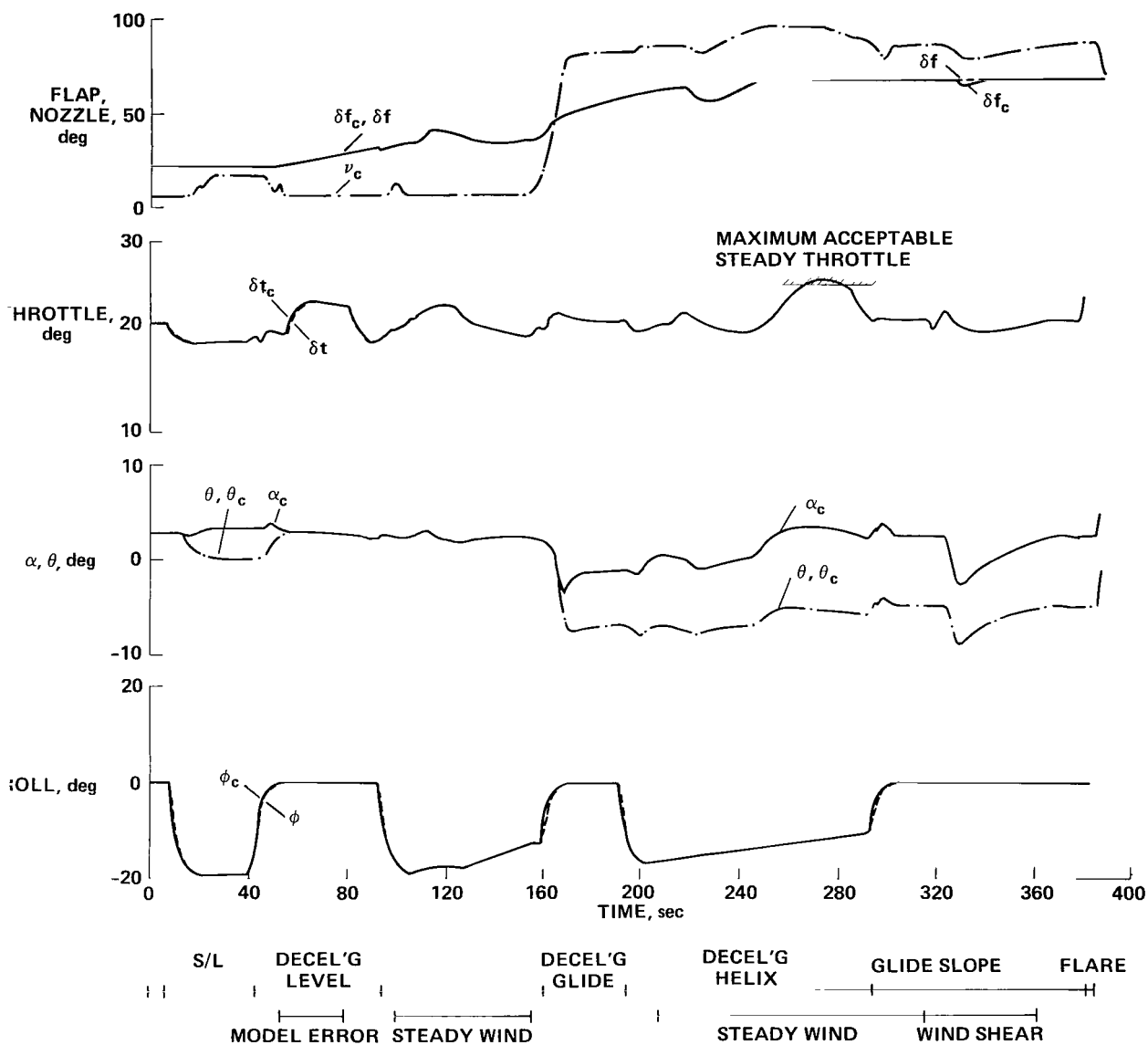
(b) Control commands time histories.

Figure 27.- Continued.
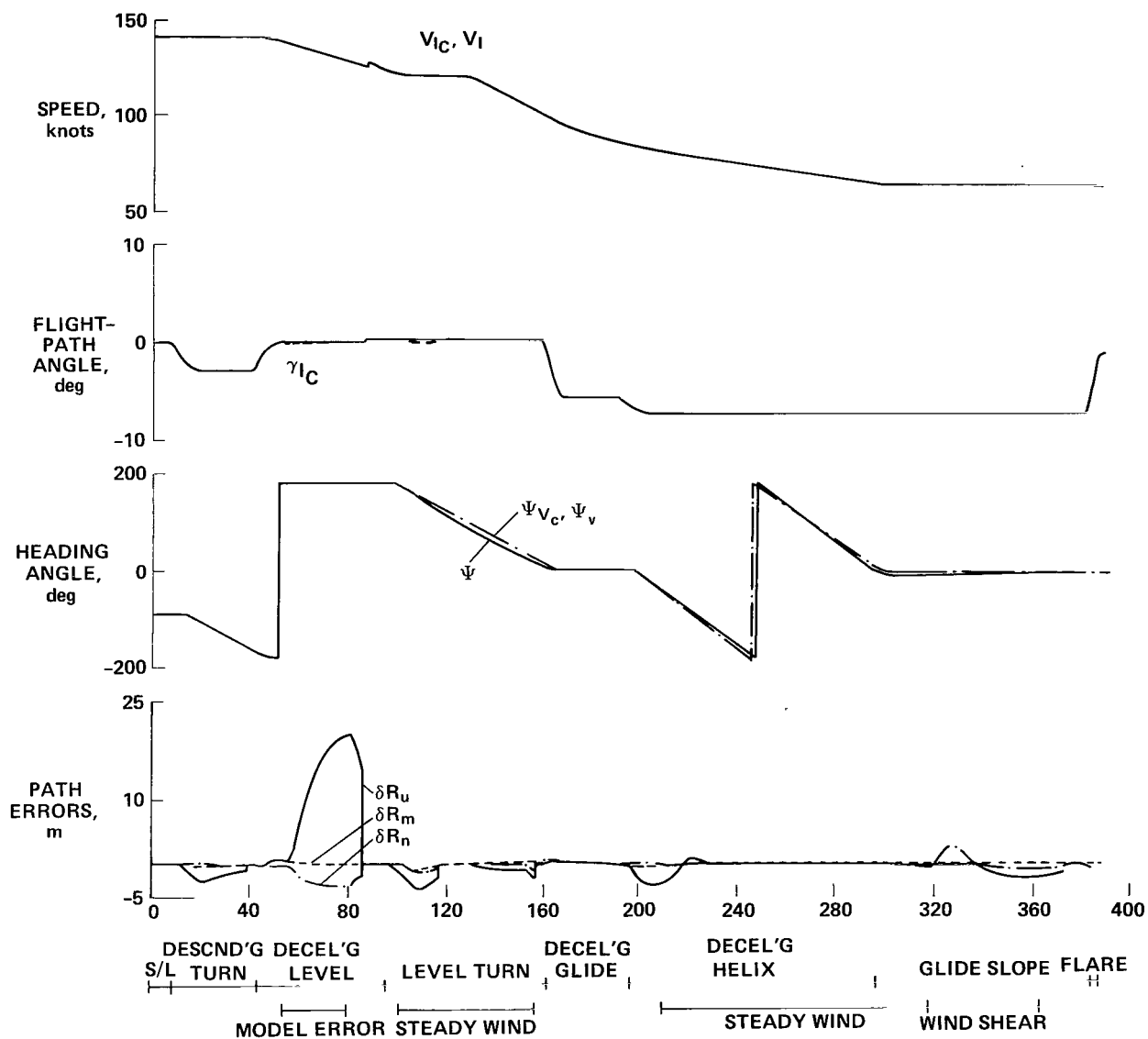
(c) Trajectory errors.

Figure 27.- Concluded.
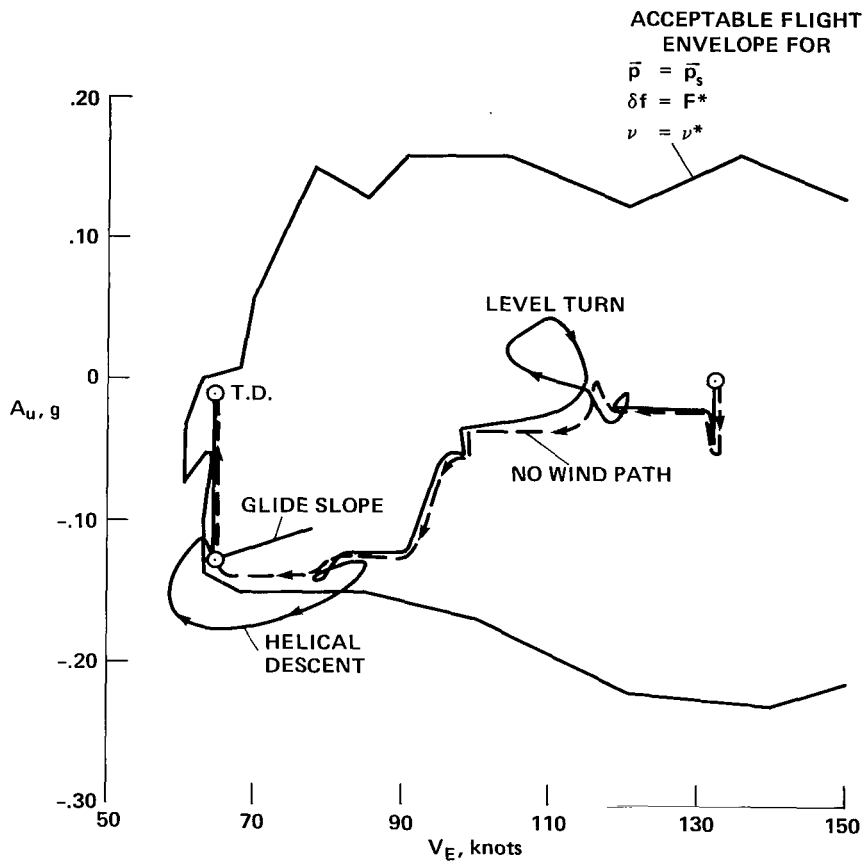
(a) Trajectory acceleration and speed locus.

Figure 28.- Simulation test path.
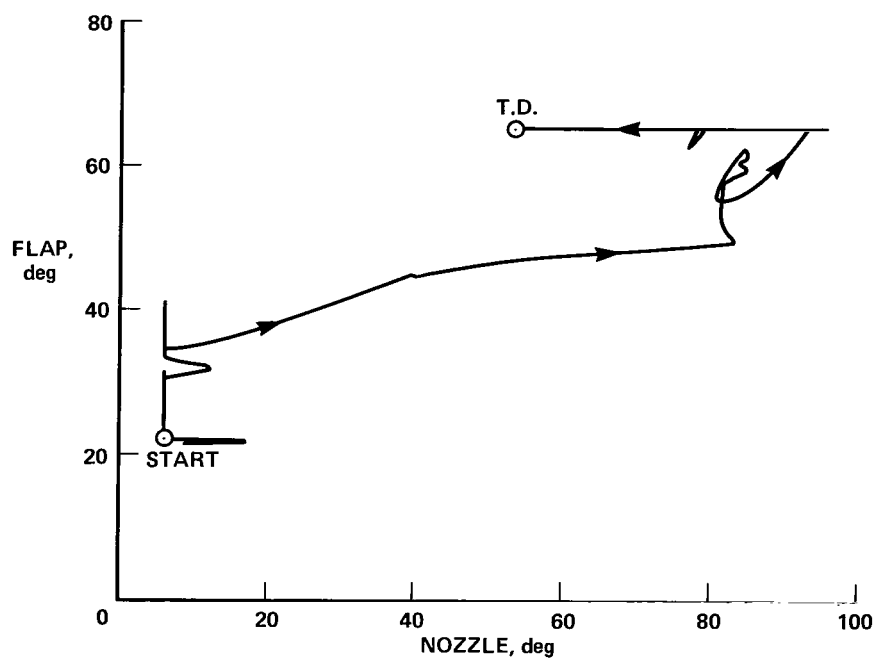
(b) Locus of configuration commands.

Figure 28.- Concluded.
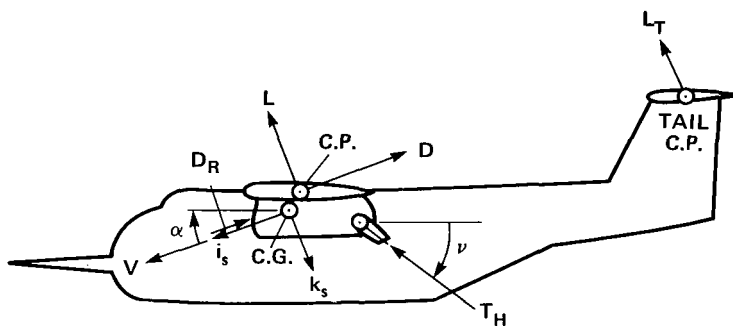
V = AIRCRAFT VELOCITY VECTOR

i_s, k_s = STABILITY AXES

α, ν = ANGLES OF V, T VECTORS FROM BODY LONGITUDINAL AXIS

L, D = WING-BODY AERODYNAMIC FORCE COMPONENTS

L_T = TAIL LIFT

D_R, T_H = ENGINE RAM DRAG AND THRUST FORCES

Figure 29.- Engine and aerodynamic forces - AWJSRA.
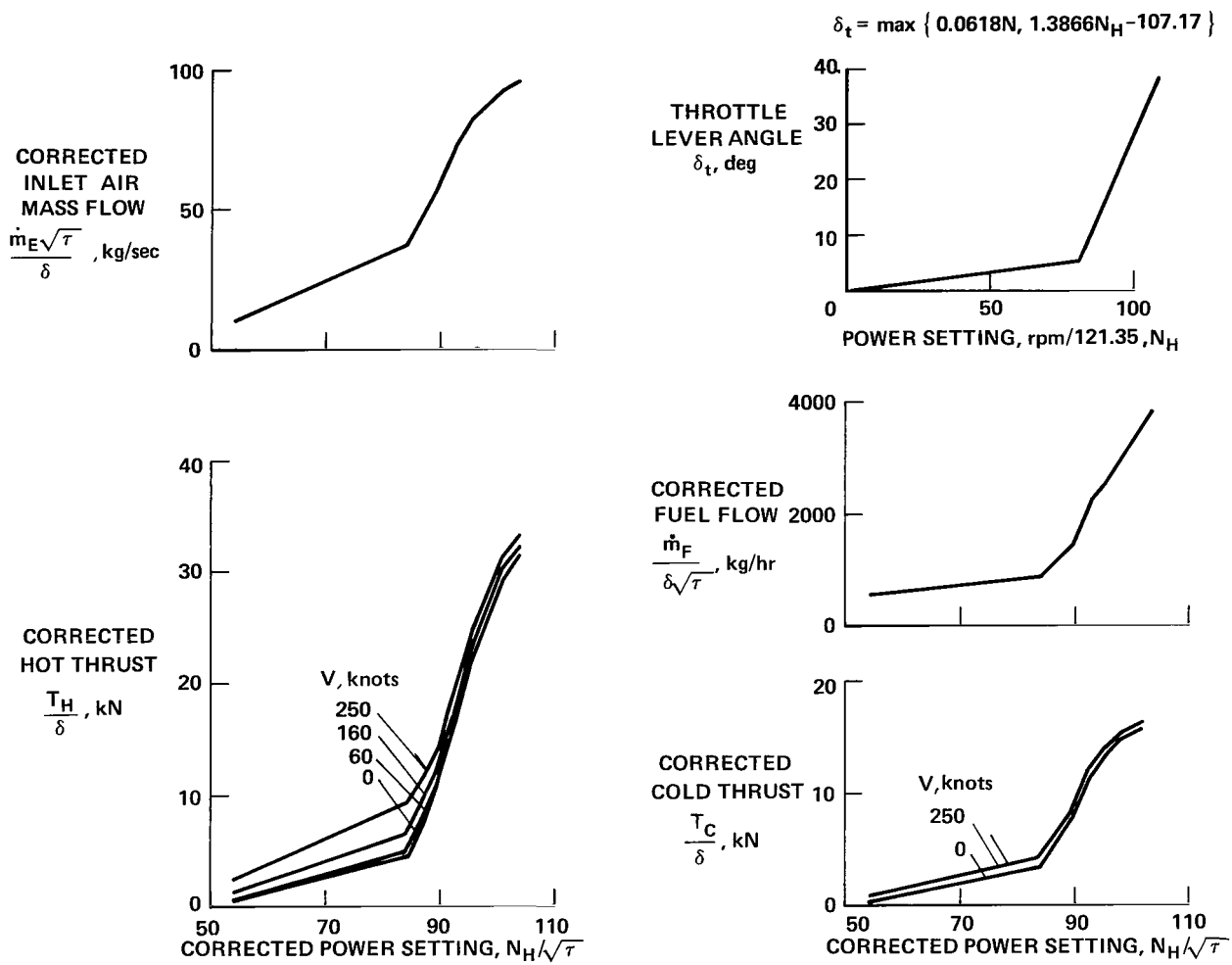
Figure 30.- AWJSRA engine model - one engine, hot thrust, cold thrust, mass flow, fuel flow and throttle-power relation.
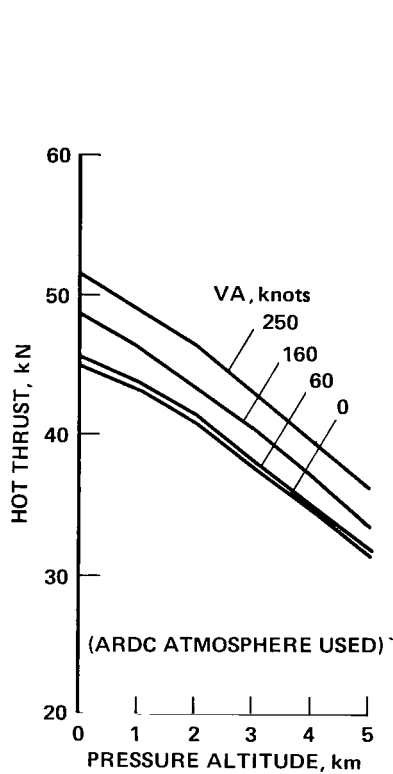
(a) Effect of altitude
    and airspeed on
    maximum continuous
    hot thrust.
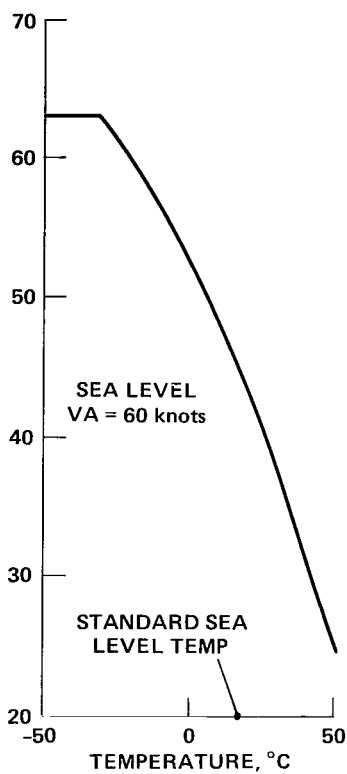
(b) Effect of tempera-
    ture on maximum
    continuous hot
    thrust.
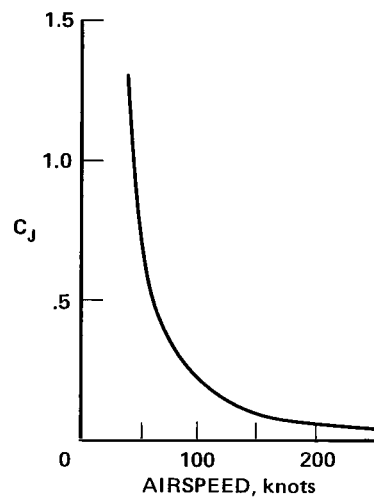
(c) Effect of air-
    speed on C_J at
    maximum continuous
    power.

Figure 31.- Engine output at maximum continuous power (N_H = 95.8):   two
engines.
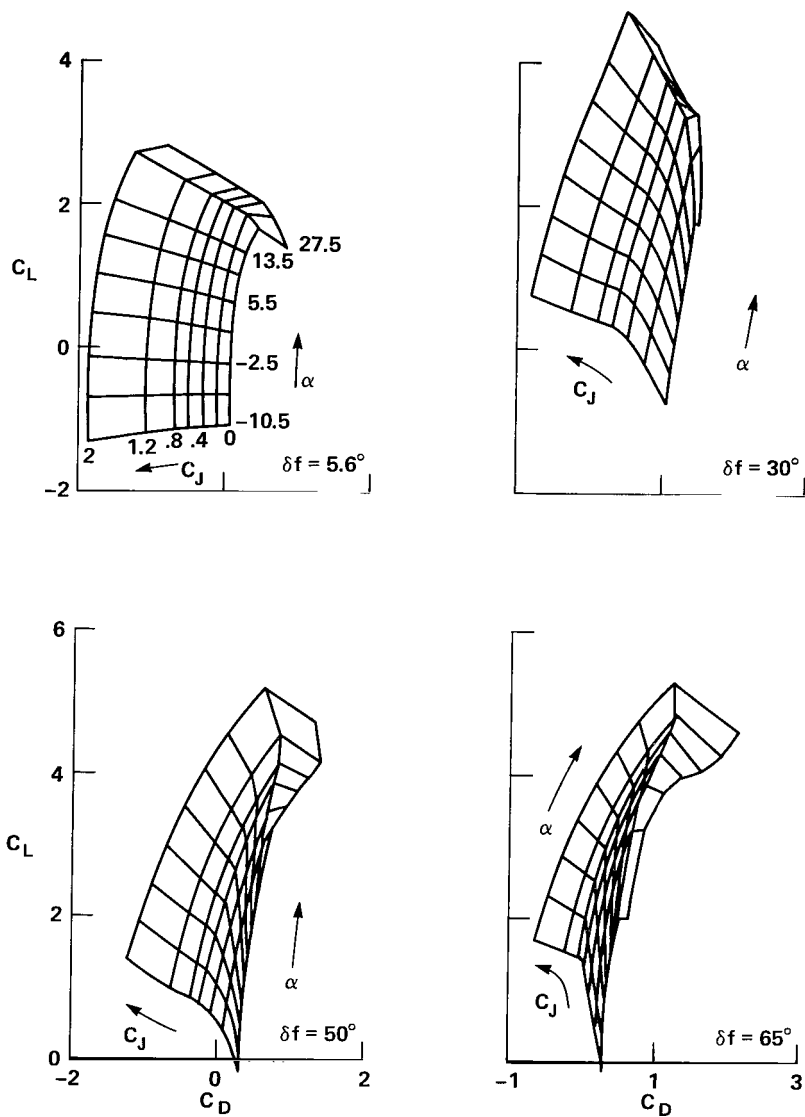
α   CONTOUR VALUES: −10.5°, −6.5°, −2.5°, 1.5°, 5.5°, 9.5°, 13.5°,
                    17.5°, 19.5°, 27.5°
C_J CONTOUR VALUES: 0, .2, .4, .6, .8, 1.2, 2

Figure 32.- Lift-drag polars — AWJSRA.
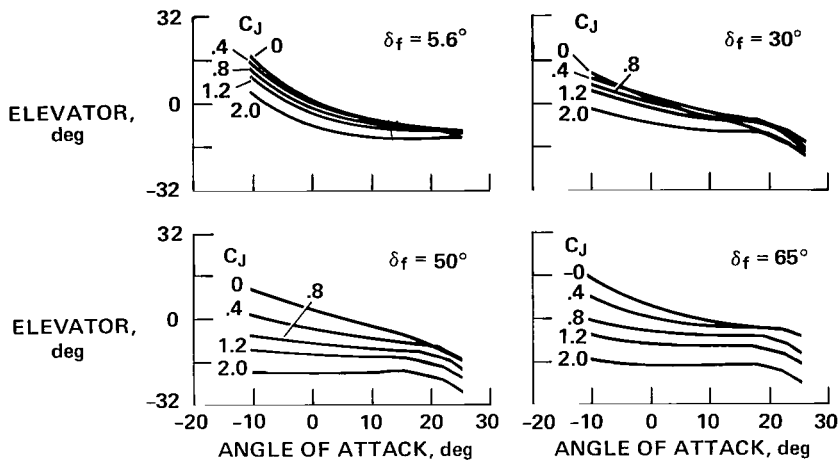
Figure 33.- AWJSRA elevator trim setting — $\delta e_A(\delta_f, \alpha, C_J)$.
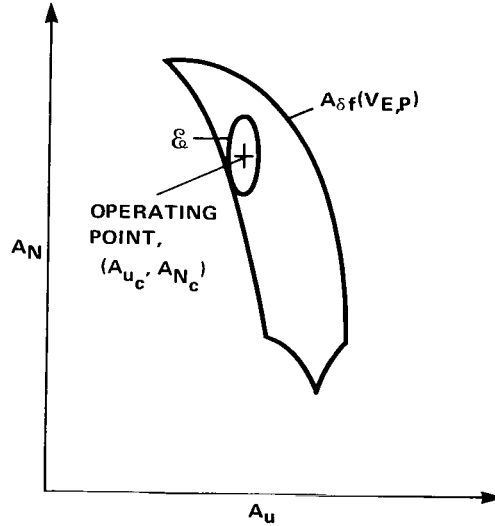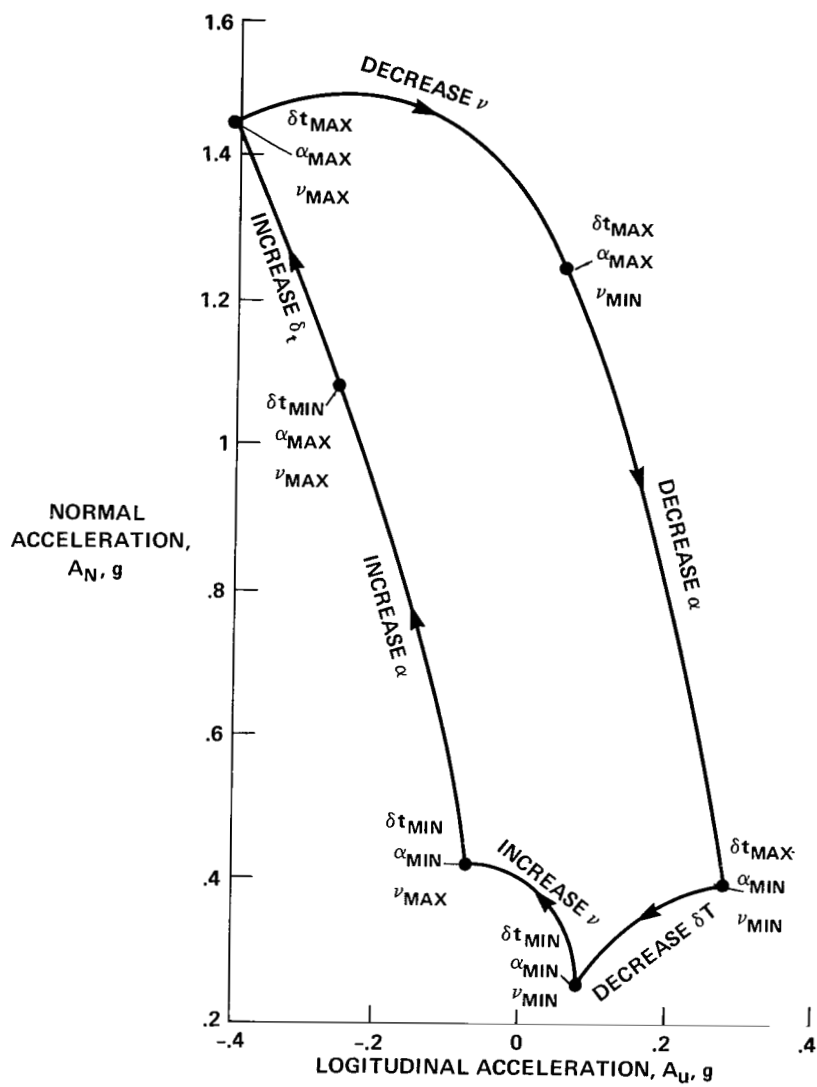

Figure 34.- Control margin definition.

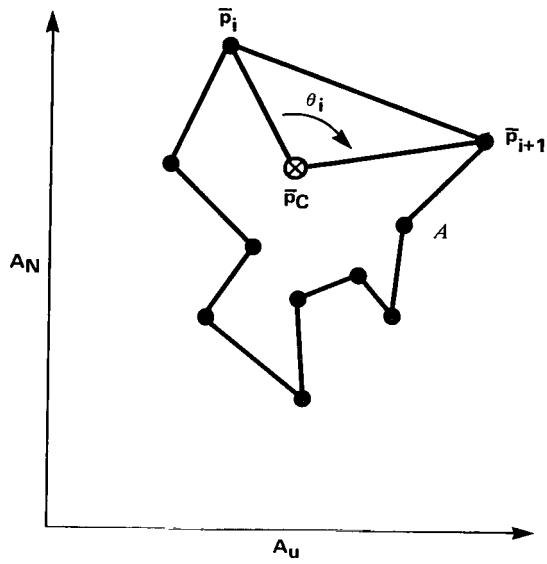Figure 35.– Acceleration envelope, $\mathscr{A}_{\delta_f}(V_E, p)$; $\delta_f = 65°$, $V_E = 65$ knots, $p = p_s$.
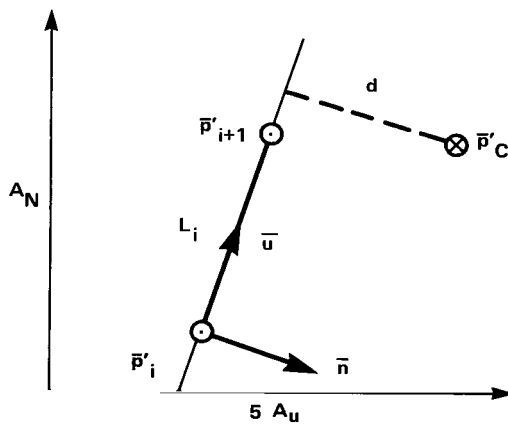
Figure 36.- Test for existence of control margin.

Figure 37.- Minimum distance from $\bar{p}'_C$ to a line segment, L.

131

1. Report No. NASA TP-1222	2. Government Accession No.	3. Recipient's Catalog No.
4. Title and Subtitle CONFIGURATION MANAGEMENT AND AUTOMATIC CONTROL OF AN AUGMENTOR WING AIRCRAFT WITH VECTORED THRUST		5. Report Date March 1979
		6. Performing Organization Code
7. Author(s) Luigi S. Cicolani, B. Sridhar,* and George Meyer		8. Performing Organization Report No. A-7099
		10. Work Unit No. 505-07-11
9. Performing Organization Name and Address NASA Ames Research Center Moffett Field, California 94035		11. Contract or Grant No.
		13. Type of Report and Period Covered Technical Paper
12. Sponsoring Agency Name and Address National Aeronautics and Space Administration Washington, D.C. 20546		14. Sponsoring Agency Code

15. Supplementary Notes

*NRC Postdoctoral Research Associate

16. Abstract

An advanced structure for automatic flight control logic for powered-lift aircraft operating i terminal areas is under investigation at Ames Research Center. This structure is based on accelera tion control; acceleration commands are constructed as the sum of acceleration on the reference trajectory and a corrective feedback acceleration to regulate path tracking errors. The central element of the structure, termed a Trimmap, uses a model of the aircraft aerodynamic and engine forces to calculate the control settings required to generate the acceleration commands.

This report describes the design criteria for the Trimmap and derives a Trimmap for Ames exper imental augmentor wing jet STOL research aircraft. The principal problems are associated with con- trol redundancy (there are two more controls than necessary to generate any given acceleration command) and model nonlinearity. Control redundancy is resolved using a stored configuration sched ule which selects two of the controls (flap and engine exhaust nozzle) as a function of the referen flight condition while the remaining two controls (elevator and throttle) are computed on the basis of the total acceleration command and the aircraft force model. The configuration schedule is derived for maximum control margins. The algebraic nonlinearity of the force model is treated usin piecewise linear descriptions of the model over its bounded domain.

The automatic control system, including the Trimmap described in this paper, was subjected to simulation tests using a rigorous STOL approach trajectory. These tests demonstrate the system response to maneuver commands, Trimmap model errors, and steady winds. The proposed Trimmap maintains an optimal configuration and coordinates all controls during any admissible maneuvers and in response to steady winds; it compensates automatically for model errors.

17. Key Words (Suggested by Author(s)) Automatic V/STOL flight control Automatic configuration schedule Trimmap Powered-lift aircraft	18. Distribution Statement Unlimited STAR Category - 08		
19. Security Classif. (of this report) Unclassified	20. Security Classif. (of this page) Unclassified	21. No. of Pages 141	22. Price* $6.00

NASA

POSTMASTER: If Undeliverable (Section .
Postal Manual) Do Not Re